ISSN 1949-8470 (online)

World Journal of *Radiology*

World J Radiol 2014 November 28; 6(11): 850-889

Published by Baishideng Publishing Group Inc

World Journal of
Radiology

A peer-reviewed, online, open-access journal of Radiology

Editorial Board

2014-2017

World Journal of Radiology

Monthly Volume 6 Number 11 November 28, 2014

Contents

World Journal of Radiology
Volume 6 Number 11 November 28, 2014

Contents

ABOUT COVER

Editorial Board Member of *World Journal of Radiology*, Jun Shen, MD, Professor, Department of Radiology, Sun Yat-Sen Memorial Hospital, Sun Yat-Sen University, Guangzhou 510120, Guangdong Province , China

AIM AND SCOPE

World Journal of Radiology (*World J Radiol*, *WJR*, online ISSN 1949-8470, DOI: 10.4329) is a peer-reviewed open access academic journal that aims to guide clinical practice and improve diagnostic and therapeutic skills of clinicians.

WJR covers topics concerning diagnostic radiology, radiation oncology, radiologic physics, neuroradiology, nuclear radiology, pediatric radiology, vascular/interventional radiology, medical imaging achieved by various modalities and related methods analysis. The current columns of *WJR* include editorial, frontier, diagnostic advances, therapeutics advances, field of vision, mini-reviews, review, topic highlight, medical ethics, original articles, case report, clinical case conference (clinicopathological conference), and autobiography.

We encourage authors to submit their manuscripts to *WJR*. We will give priority to manuscripts that are supported by major national and international foundations and those that are of great basic and clinical significance.

INDEXING/ABSTRACTING

World Journal of Radiology is now indexed in PubMed Central, PubMed, Digital Object Identifier, and Directory of Open Access Journals.

EDITORS FOR THIS ISSUE

Responsible Assistant Editor: *Xiang Li*
Responsible Electronic Editor: *Ya-Jing Lu*
Proofing Editor-in-Chief: *Lian-Sheng Ma*
Responsible Science Editor: *Fang-Fang Ji*
Proofing Editorial Office Director: *Jin-Lei Wang*

NAME OF JOURNAL
World Journal of Radiology

ISSN
ISSN 1949-8470 (online)

LAUNCH DATE
December 31, 2009

FREQUENCY
Monthly

EDITORS-IN-CHIEF
Kai U Juergens, MD, Associate Professor, MRT und PET/CT, Nuklearmedizin Bremen Mitte, ZEMODI - Zentrum für morphologische und molekulare Diagnostik, Bremen 28177, Germany

Edwin JR van Beek, MD, PhD, Professor, Clinical Research Imaging Centre and Department of Medical Radiology, University of Edinburgh, Edinburgh EH16 4TJ, United Kingdom

Thomas J Vogl, MD, Professor, Reader in Health Technology Assessment, Department of Diagnostic and Interventional Radiology, Johann Wolfgang Goethe University of Frankfurt, Frankfurt 60590, Germany

EDITORIAL OFFICE
Jin-Lei Wang, Director
Xiu-Xia Song, Vice Director
World Journal of Radiology
Room 903, Building D, Ocean International Center, No. 62 Dongsihuan Zhonglu, Chaoyang District, Beijing 100025, China
Telephone: +86-10-59080039
Fax: +86-10-85381893
E-mail: editorialoffice@wjgnet.com
Help Desk: http://www.wjgnet.com/esps/helpdesk.aspx
http://www.wjgnet.com

PUBLISHER
Baishideng Publishing Group Inc
8226 Regency Drive,
Pleasanton, CA 94588, USA
Telephone: +1-925-223-8242
Fax: +1-925-223-8243
E-mail: bpgoffice@wjgnet.com
Help Desk: http://www.wjgnet.com/esps/helpdesk.aspx
http://www.wjgnet.com

PUBLICATION DATE
November 28, 2014

INSTRUCTIONS TO AUTHORS
Full instructions are available online at http://www.wjgnet.com/1949-8470/g_info_20100316162358.htm.

ONLINE SUBMISSION
http://www.wjgnet.com/esps/

World Journal of
Radiology

Submit a Manuscript: http://www.wjgnet.com/esps/
Help Desk: http://www.wjgnet.com/esps/helpdesk.aspx
DOI: 10.4329/wjr.v6.i11.850

World J Radiol 2014 November 28; 6(11): 850-854
ISSN 1949-8470 (online)

TOPIC HIGHLIGHT

WJR 6th Anniversary Special Issues (6): CT

Spontaneous pneumomediastinum and Macklin effect: Overview and appearance on computed tomography

Sadayuki Murayama, Shinji Gibo

Sadayuki Murayama, Department of Radiology, Graduate School of Medical Science, University of the Ryukyus, Okinawa 903-0215, Japan
Shinji Gibo, Department of Radiology, Urasoe General Hospital, Okinawa 901-2132, Japan
Author contributions: Murayama S designed and wrote the paper; Gibo S provided case examples for this article.
Correspondence to: Sadayuki Murayama, MD, PhD, Department of Radiology, Graduate School of Medical Science, University of the Ryukyus, 207 Uehara, Nishihara-cho, Okinawa 903-0215, Japan. sadayuki@med.u-ryukyu.ac.jp
Telephone: +81-98-8951160 Fax: +81-98-8951420
Received: April 23, 2014 Revised: June 16, 2014
Accepted: September 23, 2014
Published online: November 28, 2014

Abstract

Spontaneous pneumomediastinum (SPM) is described as free air or gas located within the mediastinum that is not associated with any noticeable cause such as chest trauma. SPM has been associated with many conditions and triggers, including bronchial asthma, diabetic ketoacidosis, forceful straining during exercise, inhalation of drugs, as well as other activities associated with the Valsalva maneuver. The Macklin effect appears on thoracic computed tomography (CT) as linear collections of air contiguous to the bronchovascular sheaths. With the recent availability of multidetector-row CT, the Macklin effect has been seen in the clinical setting more frequently than expected. The aim of this review article is to describe the CT imaging spectrum of the Macklin effect in patients with SPM, focusing on the common appearance of the Macklin effect, pneumorrhachis, and persistent SPM with pneumatocele.

Key words: Pneumomediastinum; Spontaneous pneumomediastinum; Computed tomography; Macklin effect; Interstitial emphysema

Core tip: The Macklin effect can be frequently seen on imaging by multidetector-row computed tomography (CT) of patients who are found to have spontaneous pneumomediastinum from respiratory causes other than chest trauma. The collections of air dissect along the bronchovascular sheaths to the hilum and into the mediastinum. The Macklin effect as seen on CT may help differentiate respiratory from other etiologies of pneumomediastinum.

Murayama S, Gibo S. Spontaneous pneumomediastinum and Macklin effect: Overview and appearance on computed tomography. *World J Radiol* 2014; 6(11): 850-854 Available from: URL: http://www.wjgnet.com/1949-8470/full/v6/i11/850.htm DOI: http://dx.doi.org/10.4329/wjr.v6.i11.850

INTRODUCTION

Pneumomediastinum is described as free air or gas located within the mediastinum. It can be precipitated by various triggers that are either intrathoracic, such as stenosis or blockage of an airway, Valsalva maneuver, blunt trauma to the chest, or ruptured alveoli; or extrathoracic, such as fractured sinus, iatrogenic manipulation during tooth extraction, or ruptured intestine[1].

Spontaneous pneumomediastinum (SPM) is described as free air or gas located within the mediastinum that is not associated with any noticeable cause such as chest trauma. The first case series of SPM was reported by Hamman[2] in 1939; therefore, the condition is called Hamman syndrome[3]. Respiratory pneumomediastinum is a result of rupture along the alveolar tree, which leads to an abrupt increase in the intra-alveolar pressure. Released alveolar air centripetally dissects through the pulmonary interstitium along the bronchovascular sheaths

Figure 1 Chest computed tomography scan of an 82-year-old woman shows an injury to the posterior wall of the trachea, massive pneumomediastinum, and subcutaneous emphysema due to ruptured pars membranosa (arrow).

toward the pulmonary hila, into the mediastinum[3]. This pathophysiological mechanism was described by Macklin *et al*[4] in 1944, and is known as the Macklin effect.

SPM is usually a benign, self-limiting illness affecting young males. However, it is a condition that is not widely recognized by clinicians. There have been several reports describing the appearance of the Macklin effect on computed tomography (CT) images of patients with SPM[5-12]. This review article will describe the CT imaging spectrum of the Macklin effect as observed in patients with SPM.

THE MAIN CAUSES OF SPM

SPM occurs predominantly in young males[13,14], and is an uncommon entity. The prevalence of SPM reportedly ranges from 1 of 8005 to 1 of 42000 hospital accidents and emergency admissions[13,15]. Three different mechanisms can produce pneumomediastinum: (1) disruption of a cutaneous or mucosal barrier (usually the tracheobronchial tree or the esophagus), which allows the entry of gas into the mediastinum; (2) gas produced by organisms in the mediastinum or adjacent chest; or (3) rupture of an alveolus. Alveolar rupture is known as SPM[14,16]. SPM has been associated with many conditions and triggers, such as bronchial asthma[17], diabetic ketoacidosis[18], forceful straining during exercise[19], inhalation of drugs[20], childbirth[21], severe cough or vomiting[22], and other activities associated with the Valsalva maneuver[23]. Recent case reports have shown that SPM has also occurred in patients with gastroesophageal reflux disease[24], anorexia nervosa[25], in individuals swallowing a foreign body such as a peach seed or pork rib[26], and in a patient who practiced yoga[27].

Although pneumomediastinum can be spontaneous, without known precipitating events and without injury to mediastinal organs, pneumomediastinum can be an ominous sign of injury to mediastinal structures, including ruptured esophagus (Boerhaave syndrome) or ruptured trachea (Figure 1). Whenever pneumomediastinum is identified on imaging studies, the problem is differentiating those patients with mediastinal organ injuries from patients without organ injuries. The former require admission, diagnostic studies, and surgical treatment, while the latter can simply be observed, thereby avoiding unnecessary admissions and diagnostic tests[28].

SPM is uncommon in children. However, because of the increasing concern regarding the risks to children exposed to radiation, Chapdelaine *et al*[29] studied whether the extensive radiologic workup of SPM affects its management and outcome. Of 53 cases of SPM, 26 (49%) were related to bronchospasm, 11 (21%) were associated with respiratory infections, and 8 (15%) were of unknown etiology. Inhaled foreign bodies were associated with 4 cases. No esophageal perforations were identified. Posteroanterior chest x-ray (CXR) diagnosed every case except 1, and the mean number of CXRs performed during hospitalization was 3. Only 3 patients developed subsequent pneumothorax, and no patient needed pleural drainage. Of the 8 patients with SPM of unknown etiology, 5 underwent barium swallow and 2 underwent chest CT, and all findings were within normal limits. Therefore, the authors concluded that SPM is usually self limited, and the prognosis depends on the underlying disorder. Therefore, for patients with clinical improvement, an aggressive work up and follow-up chest imaging are rarely justified.

CT DEMONSTRATION OF THE MACKLIN EFFECTS IN SPM

Macklin and Macklin first observed that released alveolar air from alveolar rupture centripetally dissects through the pulmonary interstitium along the bronchovascular sheaths toward the pulmonary hila and into the mediastinum[4]. Wintermark and Schnyder recently reported that the rate of Macklin effect seen on chest CTs of patients with blunt trauma to the chest was 39%. They concluded that CT-associated Macklin effect was a sign of severe blunt trauma to the chest[30]. However, there have been several reports of the Macklin affect on the CT scans of patients with SPM[5-12].

As demonstrated in Figures 2-5, the Macklin effect appears on thoracic computed tomography (CT) as linear collections of air contiguous to the bronchovascular sheaths[5-12]. The air dissects into the pulmonary hila and from there enters the mediastinum. We previously reported that using multidetector-row (MD)CT, we detected the Macklin effect in 8 of 9 patients with nontraumatic pneumomediastinum , which was a higher rate of detection than had been previously reported[5]. Sakai *et al*[6] also reported a high detection rate of the Macklin effect using 64-detector-row CT. They found interstitial gas in the perihilar region of all 20 of their patients. We speculated that the increased detection rate of the Macklin effect was a result of using MDCT with application of thin collimation, a one-breath-hold technique, and visualization of magnified images on a monitor with cathode ray tubes. These factors might facilitate the identification of subtle Macklin effects. Therefore, we may conclude that

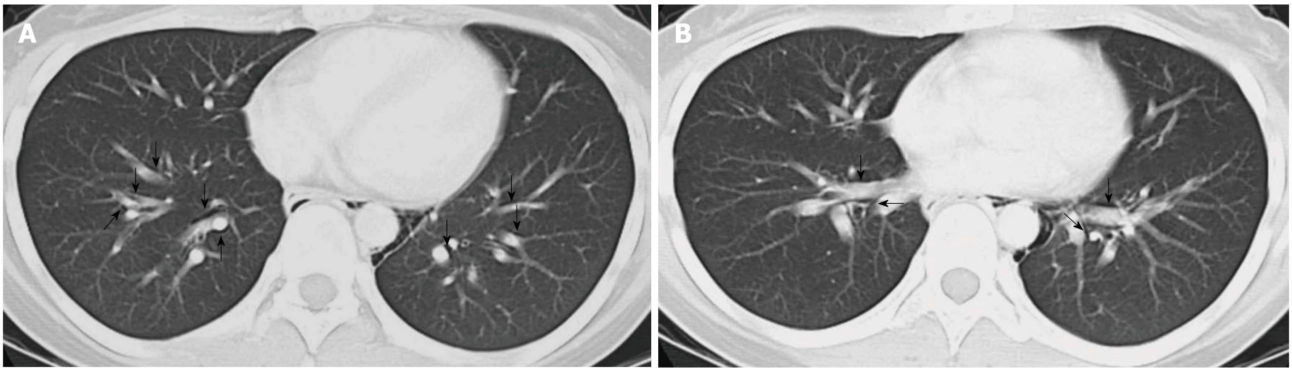

Figure 2 A 21-year-old woman with hypothyroidism and symptoms of cervical discomfort and tenderness. Multidetector-row computed tomography scan demonstrates air collection along the perivascular connective tissue, the Macklin effect (arrows), in the peripheral area (A) and in the perihilar area (B), and pneumomediastinum. Reprinted from ref. [5].

Figure 3 A 15-year-old girl with acute myeloid leukemia. Multidetector-row computed tomography scan demonstrates air collection along the perivascular connective tissue and the Macklin effect (arrow) in the perihilar area. A small pneumomediastinum is also noted.

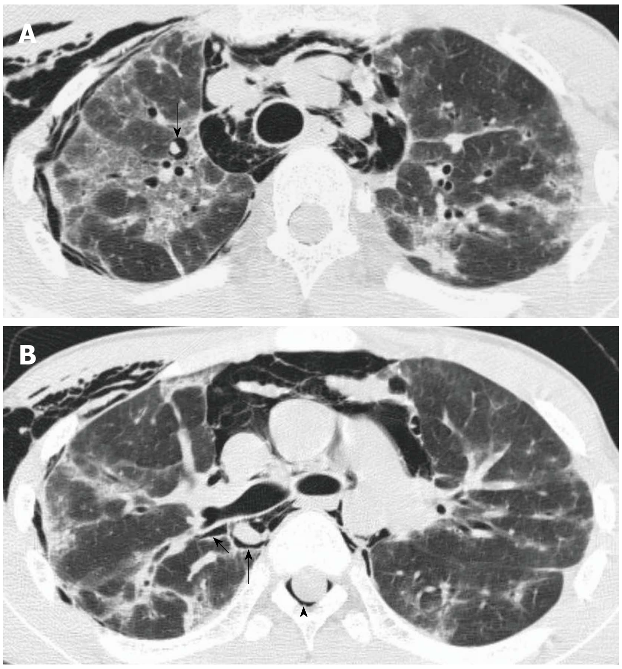

Figure 4 A 15-year-old girl with cryptogenic organizing pneumonia associated with graft-*vs*-host disease. Multidetector-row computed tomography scan demonstrates air collection along the perivascular connective tissue, the Macklin effect (arrows) in the peripheral area (A) and in the perihilar area (B), and massive pneumomediastinum. This patient also has spinal pneumorrhachis (arrowhead). Reprinted from ref. [5].

alveolar rupture described as the Macklin effect is even frequently seen in patients with SPM.

CXRs are generally useful for diagnosing pneumomediastinum, although there have been false-negative results. For false-negative cases, Okada *et al*[7] concluded that because of thin slices obtained on CT, CT is more effective than CXR alone for diagnosing pneumomediastinum. Sixty-four-detector-row CT reveals minute changes in organs and peripheral tissues. However, the Macklin effect was not detected in the peripheral lung of 4 of our reported 12 cases[5] and in 11 of 20 cases in Sakai's report[6]. We believe that since the Macklin effect develops as linear collections of air in the pulmonary interstitium that extend along the bronchi and contiguous blood vessels to gradually reach the perihilar bronchovascular sheath, the longer that time passes after its onset, the less often it is seen in the periphery of CT scans (Figure 3).

Complications of SPM

SPM is occasionally associated with pneumorrhachis, the presence of air within the spinal epidural space (Figure 4). A literature review of 48 patients with pneumorrhachis revealed that only 1 case had neurologic symptoms and signs; the other cases were successfully managed conservatively[31]. This literature review described a 72-year-old man with progressive motor weakness and sensory deficits in the lower extremities, who had a large accumulation of intraspinal air. He recovered completely after a C7 laminectomy. Kono *et al*[32] reported pneumorrhachis in 4 of 42 children with SPM, and the patients with pneumorrhachis did not have neurological symptoms. Therefore, in SPM, a collection of air within the spinal canal is mostly self limiting and benign. Pneumomediastinum concomitant with pneumoperitoneum is very rare in SPM, with only a few cases reported. It also appears to resolve with conservative treatment, without intervention[33,34].

Figure 5 A 16-year-old girl with persistent spontaneous pneumomediastinum and pneumatocele. Computed tomography shows massive pneumomediastinum and perihilar and peripheral Macklin effects (arrows). In the left lower lobe, a pneumatocele (arrowhead) is observed.

Although the Macklin effect appears on thoracic CT as linear collections of air contiguous to the bronchovascular sheaths, the onset, which is alveolar rupture, is rarely observed on CT. The released alveolar air rapidly dissects into the pulmonary hila and from there enters the mediastinum. We did have an SPM patient with a pneumatocele (Figure 5). This young female patient had interstitial pneumonia with prolonged SPM and cervical subcutaneous air. Patients found to have a Macklin effect involving peribronchovascular air and pneumatocele[35] will have a prolonged SPM, and clinical intervention is required.

CONCLUSION

The Macklin effect can be frequently observed on the MDCT images of patients with SPM not associated with trauma. A Macklin effect seen on CT may help differentiate respiratory from other etiologies of pneumomediastinum. However, especially in pediatric patients with SPM who improve clinically, aggressive investigation and follow-up CXRs are rarely warranted, and the efficacy of CT is limited.

REFERENCES

1 **Zylak CM**, Standen JR, Barnes GR, Zylak CJ. Pneumomediastinum revisited. *Radiographics* 2000; **20**: 1043-1057 [PMID: 10903694 DOI: 10.1148/radiographics.20.4.g00jl131043]

2 **Hamman L**. Spontaneous mediastinal emphysema. *Bull Johns Hopkins Hosp* 1939; **64**: 1-21

3 **Wintermark M**, Wicky S, Schnyder P, Capasso P. Blunt traumatic pneumomediastinum: using CT to reveal the Macklin effect. *AJR Am J Roentgenol* 1999; **172**: 129-130 [PMID: 9888752 DOI: 10.2214/ajr.172.1.9888752]

4 **Macklin MT**, Macklin CC. Malignant interstitial emphysema of the lungs and mediastinum as an important occult complication in many respiratory diseases and other conditions: interpretation of the clinical literature in the light of laboratory experiment. *Medicine* 1944; **23**: 281-358 [DOI: 10.1097/00005792-194412000-00001]

5 **Rosenberg JC**, Bowles AL. Nonneoplastic disorders of the mediastinum. In: Fishman AP (ed) Pulmonary diseases and disorders, 2nd ed. New York: McGraw-Hill, 1988: 2079-2083

6 **Sakai M**, Murayama S, Gibo M, Akamine T, Nagata O. Frequent cause of the Macklin effect in spontaneous pneumomediastinum: demonstration by multidetector-row computed tomography. *J Comput Assist Tomogr* 2006; **30**: 92-94 [PMID: 16365580 DOI: 10.1097/01.rct.0000187416.07698.8d]

7 **Okada M**, Adachi H, Shibuya Y, Ishikawa S, Hamabe Y. Diagnosis and treatment of patients with spontaneous pneumomediastinum. *Respir Investig* 2014; **52**: 36-40 [PMID: 24388369 DOI: 10.1016/j.resinv.2013.06.001]

8 **Kaneki T**, Kubo K, Kawashima A, Koizumi T, Sekiguchi M, Sone S. Spontaneous pneumomediastinum in 33 patients: yield of chest computed tomography for the diagnosis of the mild type. *Respiration* 2000; **67**: 408-411 [PMID: 10940795 DOI: 10.1159/000029539]

9 **Gunluoglu MZ**, Cansever L, Demir A, Kocaturk C, Melek H, Dincer SI, Bedirhan MA. Diagnosis and treatment of spontaneous pneumomediastinum. *Thorac Cardiovasc Surg* 2009; **57**: 229-231 [PMID: 19670118 DOI: 10.1055/s-2008-1039059]

10 **Franquet T**, Rodríguez S, Hernández JM, Martino R, Giménez A, Hidalgo A, Domingo P. Air-leak syndromes in hematopoietic stem cell transplant recipients with chronic GVHD: high-resolution CT findings. *J Thorac Imaging* 2007; **22**: 335-340 [PMID: 18043388 DOI: 10.1097/RTI.0b013e3180cab6cf]

11 **Satoh K**, Kobayashi T, Kawase Y, Mitani M, Nakano S, Takahashi K, Takashima H, Ohkawa M, Tanabe M, Kojima K. CT appearance of interstitial pulmonary emphysema. *J Thorac Imaging* 1996; **11**: 153-154 [PMID: 8820025 DOI: 10.1097/00005382-199621000-00006]

12 **Franquet T**, Giménez A, Torrubia S, Sabaté JM, Rodriguez-Arias JM. Spontaneous pneumothorax and pneumomediastinum in IPF. *Eur Radiol* 2000; **10**: 108-113 [PMID: 10663725 DOI: 10.1007/s003300050014]

13 **Mondello B**, Pavia R, Ruggeri P, Barone M, Barresi P, Monaco M. Spontaneous pneumomediastinum: experience in 18 adult patients. *Lung* 2007; **185**: 9-14 [PMID: 17310299 DOI: 10.1007/s00408-006-0002-7]

14 **Kelly S**, Hughes S, Nixon S, Paterson-Brown S. Spontaneous pneumomediastinum (Hamman's syndrome). *Surgeon* 2010; **8**: 63-66 [PMID: 20303884 DOI: 10.1016/j.surge.2009.10.007]

15 **McMahon DJ**. Spontaneous pneumomediastinum. *Am J Surg* 1976; **131**: 550-551 [PMID: 1275141 DOI: 10.1016/0002-9610(76)90008-8]

16 **Koullias GJ**, Korkolis DP, Wang XJ, Hammond GL. Current assessment and management of spontaneous pneumomediastinum: experience in 24 adult patients. *Eur J Cardiothorac Surg* 2004; **25**: 852-855 [PMID: 15082293 DOI: 10.1016/j.ejcts.2004.01.042]

17 **Newcomb AE**, Clarke CP. Spontaneous pneumomediastinum: a benign curiosity or a significant problem? *Chest* 2005; **128**: 3298-3302 [PMID: 16304275 DOI: 10.1378/chest.128.5.3298]

18 **Weathers LS**, Brooks WG, DeClue TJ. Spontaneous pneumomediastinum in a patient with diabetic ketoacidosis: a potentially hidden complication. *South Med J* 1995; **88**: 483-484 [PMID: 7716607 DOI: 10.1097/00007611-199504000-00022]

19 **Partridge RA**, Coley A, Bowie R, Woolard RH. Sports-related pneumothorax. *Ann Emerg Med* 1997; **30**: 539-541 [PMID: 9326870 DOI: 10.1016/S0196-0644(97)70018-0]

20 **Beauchamps G.** Spontaneous pneumothorax and pneumomediastinum. In: Pearson FG, Deslauriers J, Ginsberg RJ, Hiebert CA, McKneally MF, Urschel HC, editors. Thoracic surgery. New York: Churchill Livingstone, 1995: 1037-1054

21 **Sutherland FW**, Ho SY, Campanella C. Pneumomediastinum during spontaneous vaginal delivery. *Ann Thorac Surg* 2002; **73**: 314-315 [PMID: 11837245 DOI: 10.1016/S0003-4975(01)02729-1]

22 **Jougon JB**, Ballester M, Delcambre F, Mac Bride T, Dromer CE, Velly JF. Assessment of spontaneous pneumomediastinum: experience with 12 patients. *Ann Thorac Surg* 2003; **75**: 1711-1714 [PMID: 12822604 DOI: 10.1016/S0003-4975(03)00027-4]

23 **Panacek EA**, Singer AJ, Sherman BW, Prescott A, Rutherford WF. Spontaneous pneumomediastinum: clinical and natural history. *Ann Emerg Med* 1992; **21**: 1222-1227 [PMID: 1416301 DOI: 10.1016/S0196-0644(05)81750-0]

24 **Huang HR**, Wong KS, Lien R, Chiu CY. Spontaneous pneumomediastinum due to gastroesophageal reflux disease in an adolescent boy. *Respirology* 2008; **13**: 744-745 [PMID: 18513250 DOI: 10.1111/j.1440-1843.2008.01298.x]

25 **Hochlehnert A**, Löwe B, Bludau HB, Borst M, Zipfel S, Herzog W. Spontaneous pneumomediastinum in anorexia nervosa: a case report and review of the literature on pneumomediastinum and pneumothorax. *Eur Eat Disord Rev* 2010; **18**: 107-115 [PMID: 20148397 DOI: 10.1002/erv.1002]

26 **Cho TJ**, Kim H. Unusual presentation of spontaneous pneumomediastinum. *Lung India* 2010; **27**: 239-241 [PMID: 21139723 DOI: 10.4103/0970-2113.71961]

27 **Hafberg E**, Gudmundsson G, Gudbjartsson T. [Spontanous pneumomediastinum after yoga practice - a case report]. *Laeknabladid* 2009; **95**: 279-281 [PMID: 19420409]

28 **Banki F**, Estrera AL, Harrison RG, Miller CC, Leake SS, Mitchell KG, Khalil K, Safi HJ, Kaiser LR. Pneumomediastinum: etiology and a guide to diagnosis and treatment. *Am J Surg* 2013; **206**: 1001-1006; discussion 1006 [PMID: 24296102 DOI: 10.1016/j.amjsurg.2013.08.009]

29 **Chapdelaine J**, Beaunoyer M, Daigneault P, Bérubé D, Bütter A, Ouimet A, St-Vil D. Spontaneous pneumomediastinum: are we overinvestigating? *J Pediatr Surg* 2004; **39**: 681-684 [PMID: 15136999 DOI: 10.1016/j.jpedsurg.2004.01.045]

30 **Wintermark M**, Schnyder P. The Macklin effect: a frequent etiology for pneumomediastinum in severe blunt chest trauma. *Chest* 2001; **120**: 543-547 [PMID: 11502656 DOI: 10.1378/chest.120.2.543]

31 **Belotti EA**, Rizzi M, Rodoni-Cassis P, Ragazzi M, Zanolari-Caledrerari M, Bianchetti MG. Air within the spinal canal in spontaneous pneumomediastinum. *Chest* 2010; **137**: 1197-1200 [PMID: 20442120 DOI: 10.1378/chest.09-0514]

32 **Kono T**, Kuwashima S, Fujioka M, Kobayashi C, Koike K, Tsuchida M, Seki I. Epidural air associated with spontaneous pneumomediastinum in children: uncommon complication? *Pediatr Int* 2007; **49**: 923-927 [PMID: 18045298 DOI: 10.1111/j.1442-200X.2007.02480.x]

33 **Lantsberg L**, Rosenzweig V. Pneumomediastinum causing pneumoperitoneum. *Chest* 1992; **101**: 1176 [PMID: 1555448 DOI: 10.1378/chest.101.4.1176]

34 **Uva JL**. Spontaneous pneumothoraces, pneumomediastinum, and pneumoperitoneum: consequences of smoking crack cocaine. *Pediatr Emerg Care* 1997; **13**: 24-26 [PMID: 9061731 DOI: 10.1097/00006565-199702000-00008]

35 **Hussain N**, Noce T, Sharma P, Jagjivan B, Hegde P, Pappagallo M, Bhandari A. Pneumatoceles in preterm infants-incidence and outcome in the post-surfactant era. *J Perinatol* 2010; **30**: 330-336 [PMID: 19812584 DOI: 10.1038/jp.2009.162]

P- Reviewer: Lassandro F, Li YZ, Shen J **S- Editor**: Ji FF
L- Editor: A **E- Editor**: Lu YJ

World Journal of Radiology

Submit a Manuscript: http://www.wjgnet.com/esps/
Help Desk: http://www.wjgnet.com/esps/helpdesk.aspx
DOI: 10.4329/wjr.v6.i11.855

World J Radiol 2014 November 28; 6(11): 855-864
ISSN 1949-8470 (online)

TOPIC HIGHLIGHT

WJR 6th Anniversary Special Issues (8): fMRI

Partial volume effect modeling for segmentation and tissue classification of brain magnetic resonance images: A review

Jussi Tohka

Jussi Tohka, Department of Signal Processing, Tampere University of Technology, FIN-33101 Tampere, Finland
Author contributions: Tohka J designed and wrote the article.
Correspondence to: Jussi Tohka, PhD, Department of Signal Processing, Tampere University of Technology, PO Box 553, FIN-33101 Tampere, Finland. jussi.tohka@tut.fi
Telephone: +358-40-1981497 Fax: +358-3-3641352
Received: June 23, 2014 Revised: September 3, 2014
Accepted: September 23, 2014
Published online: November 28, 2014

Abstract

Quantitative analysis of magnetic resonance (MR) brain images are facilitated by the development of automated segmentation algorithms. A single image voxel may contain of several types of tissues due to the finite spatial resolution of the imaging device. This phenomenon, termed partial volume effect (PVE), complicates the segmentation process, and, due to the complexity of human brain anatomy, the PVE is an important factor for accurate brain structure quantification. Partial volume estimation refers to a generalized segmentation task where the amount of each tissue type within each voxel is solved. This review aims to provide a systematic, tutorial-like overview and categorization of methods for partial volume estimation in brain MRI. The review concentrates on the statistically based approaches for partial volume estimation and also explains differences to other, similar image segmentation approaches.

Key words: Magnetic resonance imaging; Segmentation; Tissue classification; White matter; Gray matter; Image processing; Brain imaging; Image analysis

Core tip: Each voxel in a brain magnetic resonance imaging (MRI) may contain multiple types of tissue. Partial volume estimation refers to a generalized image segmentation task where the amount of each tissue type within each image voxel of brain MRI is solved. This is important for volume quantification and cortical thickness analysis due to the geometrical complexity of human brain structure. This review aims to provide a systematic, tutorial-like overview of methods for partial volume estimation in brain MRI.

Tohka J. Partial volume effect modeling for segmentation and tissue classification of brain magnetic resonance images: A review. *World J Radiol* 2014; 6(11): 855-864 Available from: URL: http://www.wjgnet.com/1949-8470/full/v6/i11/855.htm DOI: http://dx.doi.org/10.4329/wjr.v6.i11.855

INTRODUCTION

Quantitative analysis of magnetic resonance (MR) brain images to gain knowledge about human brain structure is increasingly important. For example, various neuropsychiatric and neurodegenerative diseases, such as schizophrenia[1] and Alzheimer's disease[2], alter the brain structure. By analyzing these alterations, a better understanding of the underlying disease mechanisms could be gained and diseases could potentially be diagnosed more rapidly and accurately[3]. This is important since brain diseases represent a major source of the overall disease burden[4] and are often associated with heavy impact to informal caregivers.

The typical quantitative analyses to detect and quantify differences in brain structure between two or more subject groups include voxel based morphometry[5] and cortical thickness analysis[6]. These analyses are facilitated by the development of automated MR image (MRI) segmentation algorithms, which are standard tools in modern neuroscience. The image processing chain leading to MRI segmentation and, finally, to statistical analyses,

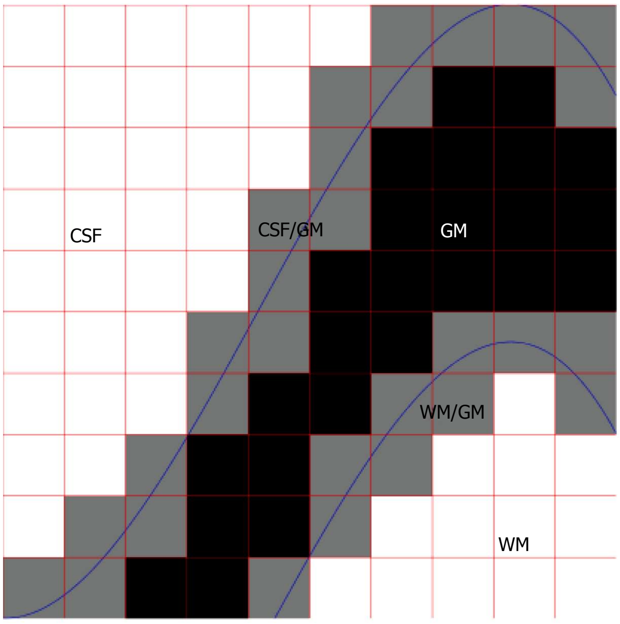

Figure 1 A schematic explanation of the partial volume effect in the context of brain magnetic resonance imaging. Voxels composed of purely gray matter (GM) are colored in black color while voxels composed of cerebro-spinal fluid (CSF) or white matter (WM) are in white color. These are termed pure tissue voxels or pure voxels. Voxels composed of multiple tissue types, termed mixed voxels, are colored in gray. In the figure, these can be either voxels containing both CSF and GM tissue types or voxels containing both WM and GM tissue types. The actual anatomical boundaries between tissue types are shown in blue and red color is used to indicate voxel boundaries.

comprises of a long pipeline of different operations including skull stripping, intensity non-uniformity correction, tissue classification, registration to the stereotactic space and cortical surfaces extraction. The point of interest in this review is the tissue classification. This refers to assigning a tissue type label to each voxel of a brain image. Typically, the three main tissue types, white matter (WM), gray matter (GM), and cerebro-spinal fluid (CSF), are considered.

A single voxel may contain of several types of tissues due to the finite spatial resolution of the imaging device. This phenomenon, termed partial volume effect (PVE), complicates the segmentation process, and, due to the complexity of human brain anatomy, the PVE is an important factor when accurate brain structure quantification is needed; Figure 1 for a schematic explanation of the PVE in the context of brain MRI. González Ballester *et al*[7,8] reported that ignoring the PVE can lead to volume measurement errors in the range of 20%-60%. Most widely used MRI segmentation algorithms account for PVE, for example by incorporating extra tissue classes[9-11]. Ruan *et al*[12] demonstrated that the intensity distributions of the partial volume voxels can be approximated using Gaussian distributions and an early work attributed the non-normality of the intensity distributions of the tissue classes to partial volume artefact[13]. However, some algorithms take a step further and try to solve an extended version of the tissue classification problem, where the amount of each tissue type within each voxel is solved. For example, hard or crisp tissue classification provides information whether a particular voxel is WM, GM, or CSF. In the extended problem, one wants to know that a voxel contains 20% GM, 80% WM and 0% of CSF and we say that the partial volume coefficients (PVCs) are 20% for GM, 80% for WM and 0% for CSF. The extended problem has various names. It has been referred to as fuzzy segmentation, partial volume segmentation, partial volume estimation, and tissue fraction estimation. It will be referred to as partial volume estimation in the remainder of this paper. In order for the partial volume estimation problem to be solvable, the intensity of a partial volume voxel has to be expressed with a model that depends on the parameters of image intensity distributions of pure tissue classes. Figure 2 exemplifies partial volume estimation as compared to hard tissue classification and also points out a specific problem of hard tissue classification particularly important to cortical thickness computations. Namely, insufficient image resolution may lead to hard tissue classification miss sulcal CSF and this may subsequently lead to incorrect cortical thickness computation if hard tissue classification is used as a preprocessing operation to the cortical thickness computation.

This review aims to provide a systematic, tutorial-like overview and categorization for different approaches for partial volume estimation in brain MRI. In addition of the author's knowledge about existing literature, the articles to be included in this review were searched on Pubmed: Search term: [(magnetic resonance [Title/Abstract] OR MRI [Title/Abstract]) AND brain [Title/Abstract] AND partial volume [Title/Abstract] AND (segmentation [Title/Abstract] OR tissue classification [Title/Abstract] OR partial volume coefficient estimation [Title/Abstract])] NOT (PET [Title/Abstract] OR emission tomography [Title/Abstract]). The search yielded 80 articles, majority of which were found relevant to this review.

IMAGE PRE-PROCESSING

The algorithms introduced in next sections require various image pre-processing steps to be performed before the partial volume estimation can take place. The preprocessing pipeline can include intensity non-uniformity correction, brain extraction (or skull stripping) and registration to a sterotactic space.

Intensity non-uniformity correction is required because MR images are known to contain low frequency spatial intensity variations often referred to as radio frequency inhomogeneity or shading artifact[14]. All segmentation algorithms in brain MRI must account for this artifact to produce accurate segmentations. There are several ways to correct for the shading artifact[14]. This can be assumed to be an image pre-processing step or to be performed jointly with the PV estimation, interleaving PV estimation (segmentation) and non-uniformity correction steps. In what follows, we will assume that the images have been corrected for this artifact.

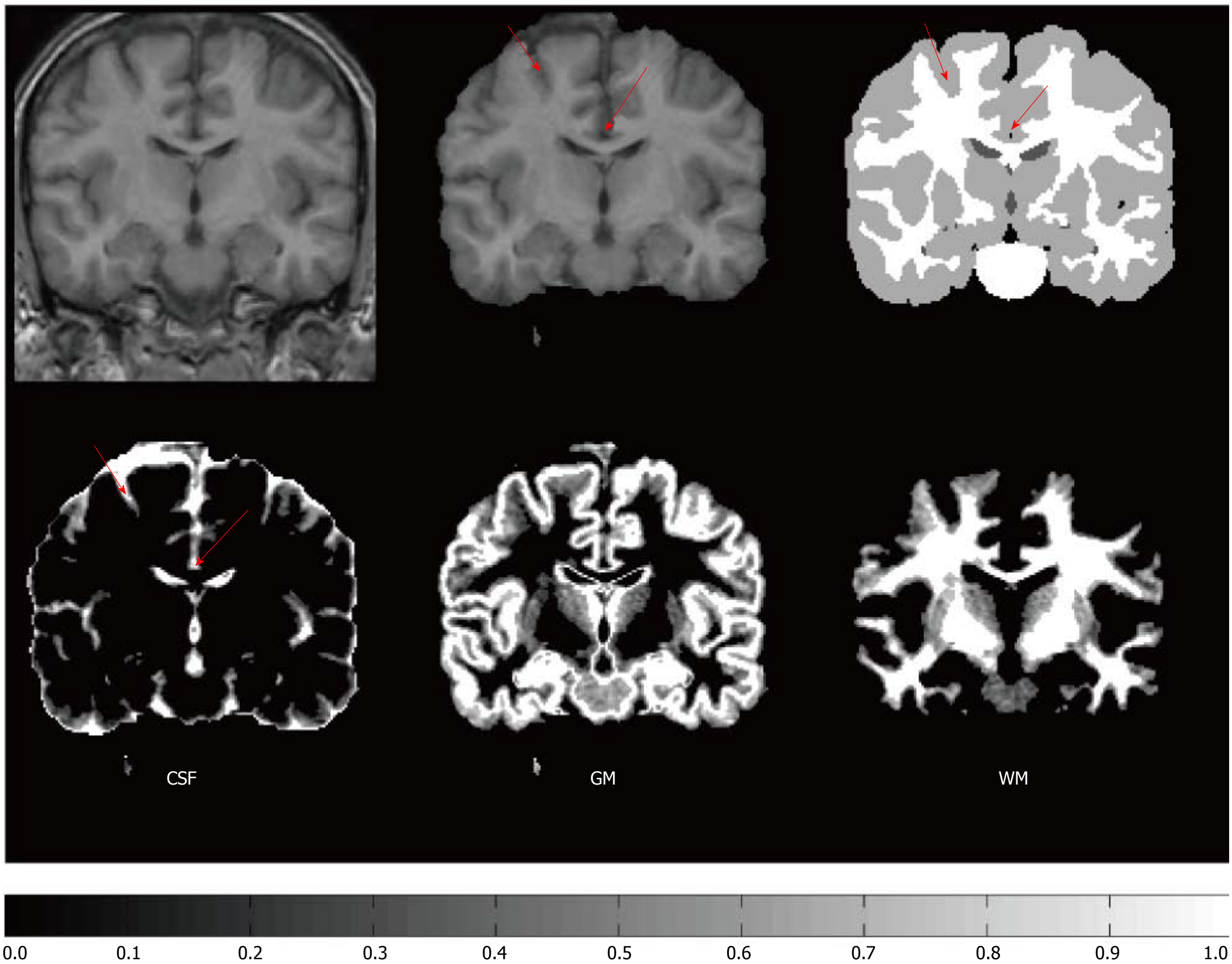

Figure 2 Example of partial volume estimation. Top row, from left: A coronal section of T1 weighted MR image; A skull stripped version of the coronal section; A manual labeling into gray matter (GM) (gray color), white matter (WM) (white color), and cerebro-spinal fluid (CSF) (dark gray color). Bottom row: Estimates of partial volume coefficients (PVCs) for CSF, GM, and WM. The color bar refers to the PVC estimates in the bottom row. The image is obtained from the IBSR2 dataset provided by the Center for Morphometric Analysis at Massachusetts General Hospital and PVCs were computed as described in the ref. [28]. Note how the manual hard labeling completely misses the CSF in the interhemispheric fissure as well as in the superior frontal sulcus pointed by red arrows. Instead PVC estimates of CSF in the bottom row capture well the sulcal CSF.

Although we are interested in segmentation of the brain tissues, brain MR images contain signal from other, extracerebral tissue types, such as skull or scalp. Because these extracerebral tissue types are often irrelevant for brain image quantification, it is useful to mask out the voxels outside the brain out before the PV estimation. This is termed skull stripping or brain extraction and the reference[15] provides a comparison of skull stripping algorithms.

The registration to stereotactic space is usually carried out to be able to utilize information of the tissue type probability maps, which, for each voxel, give a prior probability that the voxel is of certain issue type[16]. It should be noted that this is not as useful for partial volume estimation as it can be for hard segmentation, because tissue probability maps provide no information on tissue fractions[17]. Moreover, if the registered images are resampled to the stereotactic space, this amplifies the partial volume effect and may not be a recommended action.

MIXEL MODEL

Definition and approximations

The most commonly used model of PVE in brain MRI is the mixel model[18]. The mixel model assumes that each intensity value in the image is a realization of a weighted sum of random variables (RVs), each of which characterizes a pure tissue type. The original formulation[18] requires images to be multispectral, *i.e.*, that image data from multiple pulse sequences are available (for example, T1, T2,and proton density weighted images). However, there are approaches to overcome this problem by utilizing clever approximations as we shall see in Section 3.2.

We now proceed to a more formal description of the mixel model. For this, we need to establish some notation. The observed image is $X = \{x_i: i = 1,\ldots,N\}$, with the voxel intensity $x_i \in \mathbb{R}^K$, and K the number of data channels in the multispectral case. For example, if we have T1-, T2-, and proton density-weighted images, then $K = 3$.

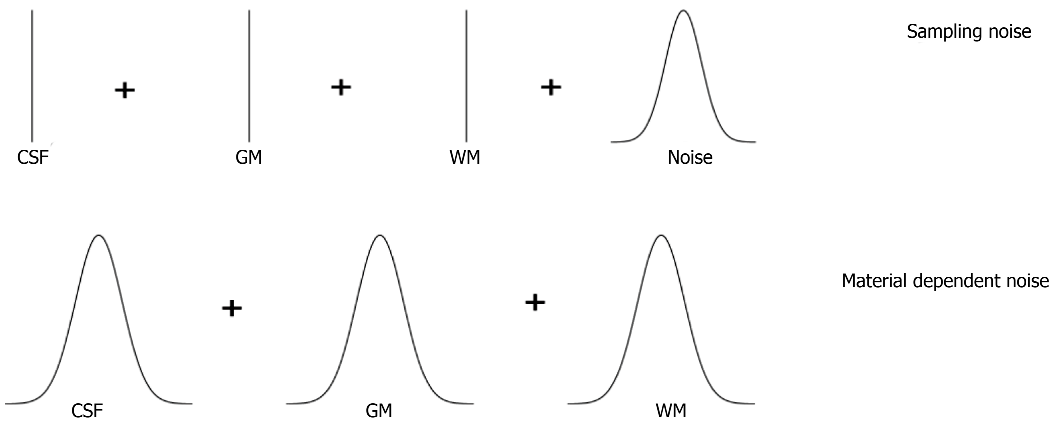

Figure 3 Sampling and material dependent noise models. Sampling noise model assumes that each tissue type is represented by a single average value and Gaussian-distributed noise is then added. Material dependent noise model assumes that the tissue types are represented by random variables. CSF: Cerebro-spinal fluid; GM: Gray matter; WM: White matter.

N denotes the number of brain voxels in the image and i is the voxel index. The voxel index has three components that correspond to the position of the voxel in the left-right, anterior-posterior, and inferior-superior axes. There are M tissue types in the image. Typically, M is equal to 3, and the tissue types are WM, GM, and CSF. The mixel model is statistically based. Thus, a voxel intensity x_i is considered to be a realization of random variable $\mathbf{x}_i$. (We use bold-face symbols to refer to random variables and the corresponding normal-face symbols denote their realizations.) Similarly, each tissue type j is described by a random variable $\mathbf{l}_j$, which is assumed to be distributed according to the multivariate normal distribution with the mean μ_j and covariance Σ_j. Random variable $\mathbf{x}_i$ is written as a weighted sum

$$\mathbf{x}_i = \sum_{j=1}^{M} w_{ij} \mathbf{l}_j + \mathbf{n}, \tag{1}$$

where $\mathbf{n}$ represents measurement noise, typically assumed to be Gaussian (with a covariance matrix Σ^*) and partial volume coefficients (PVCs) $w_{ij} \in [0, 1]$ for all i,j and $\sum_{j=1}^{M} w_{ij} = 1$ for all i. The PVCs model the fraction of each tissue type in the voxel, for example, if w_{iGM} has a value of 0.8 then the voxel contains 80% of the GM tissue type. This is similar to the fuzzy classification/segmentation problem, but in the mixel model the coefficients w_{ij} specifically model the fraction of tissue type j present in the voxel i. We will return to connections of the mixel model and the Fuzzy C-means algorithm in Section 5.

In practice, the mixel model has to be simplified because it is impossible to distinguish between measurement noise and variability within tissue types. Various simplifications have been studied by Santago *et al*[19,20]. They identified two possible types of simplification, namely, the sampling noise model and material dependent noise model as depicted in Figure 3. The sampling noise model assumes that all the randomness in the model is due to measurement noise. This leads to a model, where the tissue types are described by mean intensities of tissue types:

$$\mathbf{x}_i = \sum_{j=1}^{M} w_{ij} \mu_j + \mathbf{n}, \tag{2}$$

The material dependent noise model is obtained by embedding the measurement noise into material noise components, *i.e.*, $\mathbf{n}$ is dropped from Eq. (1)

$$\mathbf{x}_i = \sum_{j=1}^{M} w_{ij} \mathbf{l}_j. \tag{3}$$

This model is more complex than the sampling noise model, but it is probably more realistic.

Solving the mixel model

Direct solution *via* penalized least squares: Assuming the sampling noise model, the PVCs can be solved directly from Eq. (2) if enough data channels are available[18]. Denoting a matrix of all PVCs by w, the least squares criterion to minimize for solving Eq. (2) is written as

$$LS(w) = \sum_{i=1}^{N} || x_i - \sum_{j=1}^{M} w_{ij} \mu_j ||^2 \tag{4}$$

with constraints that $\sum_{j=1}^{M} w_{ij} = 1$ and $0 \leqslant w_{ij} \leqslant 1$. Note that this equation can be solved individually for each voxel. In the case of single image channel and two tissue types, the solution is particularly simple:

$$w_{i1} = r\left(\frac{x_i - \mu_2}{\mu_1 - \mu_2}\right);\ w_{i2} = 1 - w_{i1}, \tag{5}$$

and the function r limits the solution to the interval from 0 to 1, *i.e.*, $r(y) = 0$ when $y < 0$, $r(y) = y$ when $0 \leqslant y \leqslant 1$, and $r(y) = 1$ when $y > 1$. This solution is also the maximum likelihood solution and it accounts to a simple scaling of the image intensities to the interval from 0 to 1. For this reason, the solution is also very noisy and Choi *et al*[18] suggested to regularize it with a Markov Random Field (MRF) prior (see also Li *et al*[21]). The idea is that PVCs of neighboring voxels should have similar values. This leads to a modified criterion to minimize, with the same constraints as above,

$$PLS(w) = \sum_{i=1}^{N} || x_i - \sum_{j=1}^{M} w_{ij} \mu_j ||^2 + P(w) \tag{6}$$

where the term $P(w)$ penalizes differences between $w_i = [w_{i1},\ldots,w_{iM}]$ and $w_k = [w_{k1},\ldots,w_{kM}]$ if the voxels i and k

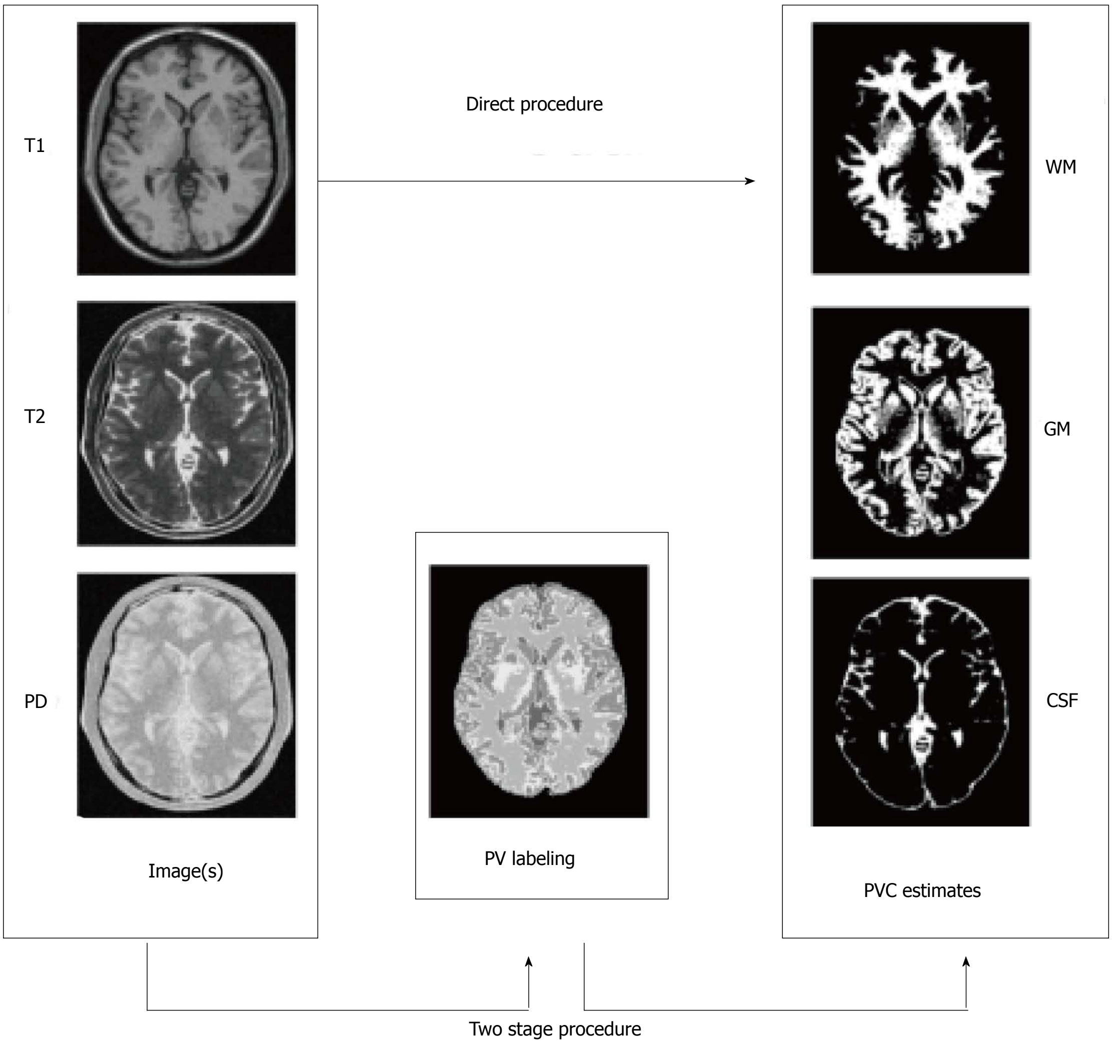

Figure 4 Direct *vs* two step procedure for partial volume coefficient estimation. CSF: Cerebro-spinal fluid; GM: Gray matter; WM: White matter; PVC: Partial volume coefficient.

are neighbours. Unfortunately, this objective cannot be anymore minimized separately for each voxel, but all the voxels must be taken into account. Besag *et al*[22] used Iterative Conditional Modes algorithm to minimize the penalized least squares criterion in Eq.(6).

Two step algorithms: The simple two-class, one-channel solution above motivates a set of techniques allowing the standard PVC estimation for three tissue types even if just data from just a single image (usually T1-weighted) is available. The idea is that since the combination of more than two tissue types in a voxel is very rare, we can estimate which two tissue types are present in a voxel before the PVC estimation; Alike idea was already mentioned for multichannel data in[18,23]. The steps of the two step algorithm can be given as follows, and they are schematically represented in Figure 4: (1) Partial volume classification: Estimate which is most likely tissue type configuration containing at most two tissue types in each voxel; and (2) PVC estimation: Solve the partial volume estimation problem limited to tissue types found in Step 1 for all the voxels.

There are at least three different approaches to solve the task in the step 1. In the simplest approach, used for example in the reference[24], the tissue classes are ordered based on their mean values so that $\mu_1 < \mu_2 < ..... < \mu_M$. Then, if the intensity value x_i lies in the interval $[\mu_k, \mu_{k+1}]$, it is assumed that the voxel i is a mixture of tissue types k and $k + 1$. This simple model does not account for the noise in the images and is not applicable for multichannel data because it assumes that the mean intensity values of tissue types can be ordered. The second approach is to detect most likely pure tissue types within the voxel based on the Bayes classifier[18,23]. This is done computing the two most probable tissue types within a voxel. However, this approach, as the first one, ignores the possibility that voxels may be composed of a single tissue type. The third and preferred approach, which is we term as probabilistic partial volume classification, fixes the just mentioned problem. The probabilistic partial volume classification approach is to compute the probability of each possible tissue type mixture appearing in the voxel[19,20,25-27]. For example, if the tissue types of interest are WM, GM, and CSF, the following 6 probabilities are computed: (1)

Voxel is solely CSF; (2) Voxel is solely GM; (3) Voxel is solely WM; (4) voxel is a mixture of background and CSF; (5) voxel is a mixture of CSF and GM; and (6) voxel is a mixture of GM and WM. (Some tissue type combinations are not considered due to their rarity in the brain.) The technical problem in the probabilistic partial volume classification approach is the construction of the probability models for mixed tissue classes; the class conditional densities for pure tissue classes are modelled by the normal density. The probability densities for the mixed tissue types can be constructed based on a marginalization technique developed originally in references[19,20] and further applied in references[25-28]. The idea is to integrate out the variable w_{i1} describing the percentage of tissue type 1 in a voxel by numerical integration. Note that with current computers the numerical integration does not present computational problem and can be solved very fast[28]. Advantages of this more complicated probabilistic approach over the two simple approaches include possibility to include spatial regularization in the form of MRFs to the step 1[25,26] and the applicability to multispectral images[26]. Additionally, it is often expected that the number of the pure tissue voxels should be greater than the number of mixed tissue voxels. The probabilistic partial volume classification includes automatic and elegant control for this issue that has been solved elsewhere by using Bayesian methods at the expense of introducing extra user-defined parameters[24,29].

Once the tissue types that are probable to appear in a voxel are determined, then the PVCs can be estimated using Eq. (5) if the sampling noise model is assumed. Note that if voxel i is determined to be a voxel of pure tissue type k, then $w_{ik} = 1$ and $w_{ij} = 0$ for other tissue types $j \neq k$. One can also adopt the material dependent noise model leading to a maximum likelihood criterion. If i is a mixed voxel of tissue types j and k, the maximum-likelihood solution is

$$w_{ij}^{*} = \arg\max_{w \in [0,1]} \log\left(g(x_i \mid \mu(w), \Sigma(w))\right) \qquad (7)$$

where $\mu(w) = w\mu_j + (1-w)\mu_k$; $\Sigma(w) = w^2\Sigma_j + (1-w)^2\Sigma_k$ or $\Sigma(w) = w\Sigma_j + (1-w)\Sigma_k$. Furthermore, $w_{ik}^{*} = 1 - w_{ij}^{*}$ and all the other PVCs are zero. The correct model for $\Sigma(w)$ has caused some controversy (see the references[30,31] for details). The difference in the two models is that the first one ($\Sigma(w) = w^2\Sigma_j + (1-w)^2\Sigma_k$) results in a more regularized solution of Eq. (7) while the second one ($\Sigma(w) = w\Sigma_j + (1-w)\Sigma_k$) is conceptually more pleasing. The maximum-likelihood PVC-estimate in Eq. (7) is solved by a simple grid search. Extensions to the maximum likelihood principle of Eq. (7) include Bayesian methods[24].

As mentioned above, the two-step algorithms can use the MRF prior to regularize the partial volume classification and this has been demonstrated to lead to more accurate partial volume estimates when the images are noisy[25]. The use of the MRF requires the user to set a proper weighting parameter for the prior which may be considered as a disadvantage[8]. However, often quoted disadvantage of the added computational cost (*e.g.*, the reference[8]) of the MRF, can be overcome by new rapid algorithms capable of performing MRF based segmentation of the typical 3-D MR images within few seconds[28]. While the two-step algorithms often use spatial MRF prior during the partial volume classification step, they typically do not utilize spatial information during the second, PVC estimation, step. Manjón *et al*[27] introduced an MRF for modelling of the spatial information during the PVC estimation step and compared it to the usage of prefiltering the images with a non-local means filter. The results suggested that using spatial information improved the PVC estimates and non-local means filtering performed better than the MRF-based approach.

Discretization approaches: An alternative to try to find real-valued PVC estimates is to discretize the PVC estimation problem[32-34]. This means that instead of letting each PVC w_{ij} lie freely in the interval from zero to one, the discretization-based methods restrict the PVCs to have only a discrete set of values. For example, w_{ij} can be 0, 0.1, 0.2,…,1.0. The discretization-based methods then try to solve maximally probable PVCs from this discretized set resorting MRF approaches to model spatial interaction between adjacent voxels[32-34]. While the restriction to a discrete set of PVC values is perfectly reasonable given the noisiness of the images, the discretization approaches are usually very time consuming, especially when compared to fast two step approaches[25,28].

Parameter estimation

The necessary model parameters $\mu_j, j = 1,\ldots,M$ and Σ^* or $\Sigma_j, j = 1,\ldots,M$ must be estimated before or during the solution of the mixel model. Correct estimation of these parameters is essential for partial volume estimation[35]. Tohka *et al*[26] identified three potential approaches to the parameter estimation problem: (1) histogram analysis; (2) simultaneous parameter, and partial volume estimation by expectation maximization (EM)-like algorithms; and (3) the estimation based on a hard segmentation of the image.

The conceptually simplest alternative is to fit a parametric model (a mixture model of pure and mixed tissue intensity densities) to an image histogram. The objective function can be based on the maximum likelihood or least squares criterion. The disadvantage of parametric model fitting is that the formulated minimization problem is complex and non-convex rendering the standard optimization algorithms useless. Various global optimization algorithms, including genetic algorithms and tree annealing, have been used for the task[19,36]. The EM-like algorithms start from an initial rough parameter estimates and refine the estimates jointly with the partial volume estimation[32,34] or classification[37] through alternating expectation and maximization steps. This can guarantee accurate parameter estimates, but the estimates depend strongly on the initial guess and the convergence of the process can be slow. The third alternative is to generate an initial rough segmentation of the image, and thereafter use outlier detection techniques based on the mathematical morphology, robust point estimates, or image gradient values to prune the set of voxels belonging to a certain tissue class[25,26,35,38,39]. Comparisons of these three techniques have been reported in the references[26,35]. The main result of these comparisons has been that the parameter estimation based on the hard segmentation of the image is fast and usually, but not always, works as well or better than the other two approaches.

RELATED METHODS

Fuzzy C-means

The standard Fuzzy C-means (FCM) algorithm optimizes a cost function

$$J_{FCM} = \sum_{i=1}^{N}\sum_{j=1}^{M} \mu_{ij}^{q} ||x_i - \mu_k||^2,$$

where u_{ij} are the fuzzy membership values μ_k are the class centroids, and q is the fuzzification parameter. This objective function and its modifications have been widely and successfully used for brain MRI tissue classification[40-43]. As shown in the reference[29], if $q = 3$, $M = 2$, and $K = 1$, optimizing the objective J_{FCM} for fixed centroids leads to the identical PVCs as PVCs derived based on Eq. (5). However, with more than two tissue types or multispectral data, fuzzy segmentations by FCM and mixel model are different.

Bayesian tissue classifiers

Often the tissue classification is casted as the Bayesian decision problem[9,16,17,44,45]. In that, one tries to estimate the posterior probability map that the tissue type is c given the image intensities. Often approaches use prior information from tissue probability maps[9,16] or MRFs[44,45] or both[17]. It should be noted that the tissue type probabilities are different from the partial volume coefficients. The exact difference of the segmentation results depends on the probability model selected, but usually these Bayesian tissue classifiers produce more crisp tissue type maps than the partial volume estimation algorithms. This issue and its ramifications are considered in a more detail by Manjón *et al*[27].

APPLICATIONS OF PARTIAL VOLUME ESTIMATION

Voxel based morphometry

Voxel-based morphometry (VBM) involves a voxel-wise comparison of the local concentration of gray matter between two groups of subjects. The procedure consists of segmenting the gray matter from the MR images and spatially normalizing these gray matter images from all the subjects in the study into the same stereotactic space[5]. These gray matter images can either represent GM tissue probabilities, for example, as in the reference[46] or GM tissue fractions resulting partial volume estimation, for example, as in the reference[47]. While it seems clear that the PVCs are better representations of gray matter density than gray matter probabilities, it is not clear whether this particular modelling choice has a major effect on the accuracy of the results. To author's knowledge, gray matter probability and gray matter PV-coefficient based VBM methods have not been directly compared. Tardif *et al*[48] examined two pipelines resulting in GM probability based VBM and PVC based VBM but the main focus of the work was on a comparison of 1.5T and 3T imaging protocols. The VBM8 software package (http://dbm.neuro.uni-_jena.de/vbm/) offers possibility to VBM using PVCs[49].

Cortical thickness

Cortical thickness is a quantitative measure describing the combined thickness of the layers of the cerebral cortex that can be measured using MRI either using mesh based[6,50,51] or voxel based techniques[52]. The thickness of the cortex, and its local variations, are of great interest in both normal development as well as a wide variety of neurodegenerative and psychiatric disorders[6]. Cortex is a highly folded structure with an approximate average thickness of 2.5 mm[53] and hence it is not difficult to appreciate that the partial volume effect has been an important consideration when measuring cortical thickness. Both surface mesh based[54] and voxel based[55-57] cortical thickness measures can be shown to be improved if the partial volume effect is taken into account. Especially, as demonstrated in Figure 2 and discussed further in the references[26,54], hard tissue classifications may miss some of the sulcal CSF because of an insufficient image resolution. This causes incorrect reconstruction of the GM/CSF boundary, which, in turn, leads to errors in the cortical thickness computation.

Other applications

Other applications of segmentation with the PVE modeling identified during the literature review were segmentation of the brain images of the neonates[58-61], hemisphere segmentation and related shape analysis[62,63], EEG source localization[64], and lesion load computations based on MRI[65-68]. Especially, in the case of the Multiple Sclerosis (MS) lesion volumetry, the correction for the partial volume effects has a large positive effect on the reproducibility and accuracy of the analysis[69]. In particular, it was found to be important in avoiding of misclassification of some non-lesion voxels (between CSF and brain tissue) into lesion voxels[69].

CONCLUSION

An interesting recent development in MRI segmentation and partial volume estimation is the use of quantitative tissue type maps for the purpose[70-72]. For example, Ahlgren *et al*[70] utilized the signal of a spoiled gradient-recalled echo (SPGR) sequence acquired with multiple flip angles to map T1, and subsequently to fit of a multi-compartment model yielding parametric maps of partial volume estimates of the different compartments. West *et al*[71] used quantitative MRI values of the longitudinal relaxation rate, the transverse relaxation rate and the proton density to define tissues (WM,GM,CSF) and constructed a lookup table for partial volume estimation. These quantitative approaches show good potential to improve the partial volume estimation accuracy. Another recent development is the use of high-field MRI to map smaller and smaller brain structures[73], such cortical layers or hippocampal subfields[74]. These efforts will benefit from automated segmentation. Despite of improved image resolution provided by higher field strengths the problems related to partial volume effect will remain as the structures of interest will become smaller at the same time. For example, while the improved image resolution will diminish (but not completely erase) the challenges related to partial volume effect in the cortical thickness computation, it will also possibly allow studies concerning individual cortical layers requiring a higher image resolution, where partial volume effect is again an important consideration.

REFERENCES

1 **Shenton ME**, Dickey CC, Frumin M, McCarley RW. A review of MRI findings in schizophrenia. *Schizophr Res* 2001; **49**: 1-52 [PMID: 11343862 DOI: 10.1016/S0920-9964(01)00163-3]

2 **Weiner MW**, Veitch DP, Aisen PS, Beckett LA, Cairns NJ, Green RC, Harvey D, Jack CR, Jagust W, Liu E, Morris JC, Petersen RC, Saykin AJ, Schmidt ME, Shaw L, Shen L, Siuciak JA, Soares H, Toga AW, Trojanowski JQ. The Alzheimer's Disease Neuroimaging Initiative: a review of papers published since its inception. *Alzheimers Dement* 2013; **9**: e111-e194 [PMID: 23932184 DOI: 10.1016/j.jalz.2013.05.1769]

3 **Frisoni GB**, Fox NC, Jack CR, Scheltens P, Thompson PM. The clinical use of structural MRI in Alzheimer disease. *Nat Rev Neurol* 2010; **6**: 67-77 [PMID: 20139996 DOI: 10.1038/nrneurol.2009.215]

4 **Olesen J**, Leonardi M. The burden of brain diseases in Europe. *Eur J Neurol* 2003; **10**: 471-477 [PMID: 12940825 DOI: 10.1046/j.1468-1331.2003.00682.x]

5 **Ashburner J**, Friston KJ. Voxel-based morphometry--the methods. *Neuroimage* 2000; **11**: 805-821 [PMID: 10860804 DOI: 10.1006/nimg.2000.0582]

6 **Fischl B**, Dale AM. Measuring the thickness of the human cerebral cortex from magnetic resonance images. *Proc Natl Acad Sci USA* 2000; **97**: 11050-11055 [PMID: 10984517 DOI: 10.1073/pnas.200033797]

7 **González Ballester MA**, Zisserman A, Brady M. Segmentation and measurement of brain structures in MRI including confidence bounds. *Med Image Anal* 2000; **4**: 189-200 [PMID: 11145308 DOI: 10.1016/S1361-8415(00)00013-X]

8 **González Ballester MA**, Zisserman AP, Brady M. Estimation of the partial volume effect in MRI. *Med Image Anal* 2002; **6**: 389-405 [PMID: 12494949 DOI: 10.1016/S1361-8415(02)00061-0]

9 **Ashburner J**, Friston KJ. Unified segmentation. *Neuroimage* 2005; **26**: 839-851 [PMID: 15955494 DOI: 10.1016/j.neuroimage.2005.02.018]

10 **Beck CW**, Slack JM. Analysis of the developing Xenopus tail bud reveals separate phases of gene expression during determination and outgrowth. *Mech Dev* 1998; **72**: 41-52 [PMID: 9533951 DOI: 10.1109/42.650887]

11 **Cuadra MB**, Cammoun L, Butz T, Cuisenaire O, Thiran JP. Comparison and validation of tissue modelization and statistical classification methods in T1-weighted MR brain images. *IEEE Trans Med Imaging* 2005; **24**: 1548-1565 [PMID: 16350916 DOI: 10.1109/TMI.2005.857652]

12 **Ruan S**, Jaggi C, Xue J, Fadili J, Bloyet D. Brain tissue classification of magnetic resonance images using partial volume modeling. *IEEE Trans Med Imaging* 2000; **19**: 1179-1187 [PMID: 11212366 DOI: 10.1109/42.897810]

13 **Bullmore E**, Brammer M, Rouleau G, Everitt B, Simmons A, Sharma T, Frangou S, Murray R, Dunn G. Computerized brain tissue classification of magnetic resonance images: a new approach to the problem of partial volume artifact. *Neuroimage* 1995; **2**: 133-147 [PMID: 9343596 DOI: 10.1006/nimg.1995.1016]

14 **Vovk U**, Pernus F, Likar B. A review of methods for correction of intensity inhomogeneity in MRI. *IEEE Trans Med Imaging* 2007; **26**: 405-421 [PMID: 17354645 DOI: 10.1109/TMI.2006.891486]

15 **Shattuck DW**, Prasad G, Mirza M, Narr KL, Toga AW. Online resource for validation of brain segmentation methods. *Neuroimage* 2009; **45**: 431-439 [PMID: 19073267 DOI: 10.1016/j.neuroimage.2008.10.066]

16 **Ashburner J**, Friston K. Multimodal image coregistration and partitioning--a unified framework. *Neuroimage* 1997; **6**: 209-217 [PMID: 9344825 DOI: 10.1006/nimg.1997.0290]

17 **Tohka J**, Dinov ID, Shattuck DW, Toga AW. Brain MRI tissue classification based on local Markov random fields. *Magn Reson Imaging* 2010; **28**: 557-573 [PMID: 20110151 DOI: 10.1016/j.mri.2009.12.012]

18 **Choi HS**, Haynor DR, Kim Y. Partial volume tissue classification of multichannel magnetic resonance images-a mixel model. *IEEE Trans Med Imaging* 1991; **10**: 395-407 [PMID: 18222842 DOI: 10.1109/42.97590]

19 **Santago P**, Gage HD. Quantification of MR brain images by mixture density and partial volume modeling. *IEEE Trans Med Imaging* 1993; **12**: 566-574 [PMID: 18218450 DOI: 10.1109/42.241885]

20 **Santago P**, Gage HD. Statistical models of partial volume effect. *IEEE Trans Image Process* 1995; **4**: 1531-1540 [PMID: 18291985 DOI: 10.1109/83.469934]

21 **Li X**, Li L, Lu H, Liang Z. Partial volume segmentation of brain magnetic resonance images based on maximum a posteriori probability. *Med Phys* 2005; **32**: 2337-2345 [PMID: 16121590 DOI: 10.1118/1.1944912]

22 **Besag J.** On the statistical analysis of dirty pictures. *Journal of the Royal Statistical Society, Series B* 1986; **48:** 259-302. Available from: URL: http: //www.jstor.org/stable/2345426

23 **Choi H**, Haynor D, Kim Y. Multivariate tissue classification of mri images for 3-d volume reconstruction-a statistical approach. In: Proc. SPIE vol. 1092, Medical Imaging III: Image Processing, 1989: 183-193

24 **Brouwer RM**, Hulshoff Pol HE, Schnack HG. Segmentation of MRI brain scans using non-uniform partial volume densities. *Neuroimage* 2010; **49**: 467-477 [PMID: 19635574 DOI: 10.1016/j.neuroimage.2009.07.041]

25 **Shattuck DW**, Sandor-Leahy SR, Schaper KA, Rottenberg DA, Leahy RM. Magnetic resonance image tissue classification using a partial volume model. *Neuroimage* 2001; **13**: 856-876 [PMID: 11304082 DOI: 10.1006/nimg.2000.0730]

26 **Tohka J**, Zijdenbos A, Evans A. Fast and robust parameter estimation for statistical partial volume models in brain MRI. *Neuroimage* 2004; **23**: 84-97 [PMID: 15325355 DOI: 10.1016/j.neuroimage.2004.05.007]

27 **Manjón JV**, Tohka J, Robles M. Improved estimates of partial volume coefficients from noisy brain MRI using spatial context. *Neuroimage* 2010; **53**: 480-490 [PMID: 20600978 DOI: 10.1016/j.neuroimage.2010.06.046]

28 **Tohka J**. FAST-PVE: Extremely fast markov random field based brain MRI tissue classification. In: Image Analysis,

18th Scandinavian Conference, SCIA 2013, Lecture notes in computer science vol. 7944. SCIA: Springer, 2013: 266-276 [DOI: 10.1007/978-3-642-38886-6_26]
29 **Pham DL**, Prince J. Partial volume estimation and the fuzzy c-means algorithm. In: Image Processing, 1998. ICIP 98. Proceedings. ICIP: 1998 International Conference on, vol. III, 1998: 819-822 [DOI: 10.1109/ICIP.1998.999071]
30 **Bromiley P**, Thacker N. Multi-dimensional medical image segmentation with partial volume and gradient modelling. *Annals of the BMVA* 2008; **(2)**: 1-22. Available from: URL: http: //www.bmva.org/annals/2008/2008-0002.pdf
31 **Bromiley P,** Thacker N . Multi-dimensional medical image segmentation with partial volume and gradient modelling. Mathematical derivations and proofs. *Annals of the BMVA* 2008; **(2s1)**: 1-11. Available from: URL: http: //www.bmva.org/annals/2008/2008-0002-supplement.pdf
32 **Bricq S**, Collet Ch, Armspach JP. Unifying framework for multimodal brain MRI segmentation based on Hidden Markov Chains. *Med Image Anal* 2008; **12**: 639-652 [PMID: 18440268 DOI: 10.1016/j.media.2008.03.001]
33 **Ruan S**, Moretti B, Fadili J, Bloyet D. Fuzzy markovian segmentation in application of magnetic resonance images. *Comput Vis Image Und* 2002; **85**: 54-69 [DOI: 10.1006/cviu.2002.0957]
34 **Van Leemput K**, Maes F, Vandermeulen D, Suetens P. A unifying framework for partial volume segmentation of brain MR images. *IEEE Trans Med Imaging* 2003; **22**: 105-119 [PMID: 12703764 DOI: 10.1109/TMI.2002.806587]
35 **Manjón JV**, Tohka J, García-Martí G, Carbonell-Caballero J, Lull JJ, Martí-Bonmatí L, Robles M. Robust MRI brain tissue parameter estimation by multistage outlier rejection. *Magn Reson Med* 2008; **59**: 866-873 [PMID: 18383286 DOI: 10.1002/mrm.21521]
36 **Tohka J**, Krestyannikov E, Dinov ID, Graham AM, Shattuck DW, Ruotsalainen U, Toga AW. Genetic algorithms for finite mixture model based voxel classification in neuroimaging. *IEEE Trans Med Imaging* 2007; **26**: 696-711 [PMID: 17518064 DOI: 10.1109/TMI.2007.895453]
37 **Noe A,** Gee J. Partial volume segmentation of cerebral MRI scans with mixture model clustering. In: Proc. of Information Processing in Medical Imaging. IPMI: 17th International Conference, 2001: 423-430 [DOI: 10.1007/3-540-45729-1_44]
38 **Wang D**, Doddrell DM. A segmentation-based and partial-volume-compensated method for an accurate measurement of lateral ventricular volumes on T(1)-weighted magnetic resonance images. *Magn Reson Imaging* 2001; **19**: 267-273 [PMID: 11358664 DOI: 10.1016/S0730-725X(01)00235-1]
39 **Wang D**, Doddrell DM. MR image-based measurement of rates of change in volumes of brain structures. Part I: method and validation. *Magn Reson Imaging* 2002; **20**: 27-40 [PMID: 11973027 DOI: 10.1016/S0730-725X(02)00466-6]
40 **Suckling J**, Sigmundsson T, Greenwood K, Bullmore ET. A modified fuzzy clustering algorithm for operator independent brain tissue classification of dual echo MR images. *Magn Reson Imaging* 1999; **17**: 1065-1076 [PMID: 10463658 DOI: 10.1016/S0730-725X(99)00055-7]
41 **Ortiz A**, Palacio AA, Górriz JM, Ramírez J, Salas-González D. Segmentation of brain MRI using SOM-FCM-based method and 3D statistical descriptors. *Comput Math Methods Med* 2013; **2013**: 638563 [PMID: 23762192 DOI: 10.1155/2013/638563]
42 **Pham DL**, Prince JL. Adaptive fuzzy segmentation of magnetic resonance images. *IEEE Trans Med Imaging* 1999; **18**: 737-752 [PMID: 10571379 DOI: 10.1109/42.802752]
43 **Yoon UC**, Kim JS, Kim JS, Kim IY, Kim SI. Adaptable fuzzy C-Means for improved classification as a preprocessing procedure of brain parcellation. *J Digit Imaging* 2001; **14**: 238-240 [PMID: 11442112 DOI: 10.1007/BF03190353]
44 **Van Leemput K**, Maes F, Vandermeulen D, Suetens P. Automated model-based tissue classification of MR images of the brain. *IEEE Trans Med Imaging* 1999; **18**: 897-908 [PMID: 10628949 DOI: 10.1109/42.811270]
45 **Zhang Y**, Brady M, Smith S. Segmentation of brain MR images through a hidden Markov random field model and the expectation-maximization algorithm. *IEEE Trans Med Imaging* 2001; **20**: 45-57 [PMID: 11293691 DOI: 10.1109/42.906424]
46 **Good CD**, Johnsrude I, Ashburner J, Henson RN, Friston KJ, Frackowiak RS. Cerebral asymmetry and the effects of sex and handedness on brain structure: a voxel-based morphometric analysis of 465 normal adult human brains. *Neuroimage* 2001; **14**: 685-700 [PMID: 11506541 DOI: 10.1006/nimg.2001.0857]
47 **Nagano-Saito A**, Washimi Y, Arahata Y, Kachi T, Lerch JP, Evans AC, Dagher A, Ito K. Cerebral atrophy and its relation to cognitive impairment in Parkinson disease. *Neurology* 2005; **64**: 224-229 [PMID: 15668417 DOI: 10.1212/01.WNL.0000149510.41793.50]
48 **Tardif CL**, Collins DL, Pike GB. Regional impact of field strength on voxel-based morphometry results. *Hum Brain Mapp* 2010; **31**: 943-957 [PMID: 19862698 DOI: 10.1002/hbm.20908]
49 **Gaser C**. Partial volume segmentation with adaptive maximum a posteriori (MAP) approach. *NeuroImage* 2009: **47:** S121 [DOI: 10.1016/S1053-8119(09)71151-6]
50 **MacDonald D**, Kabani N, Avis D, Evans AC. Automated 3-D extraction of inner and outer surfaces of cerebral cortex from MRI. *Neuroimage* 2000; **12**: 340-356 [PMID: 10944416 DOI: 10.1006/nimg.1999.0534]
51 **Lerch JP**, Evans AC. Cortical thickness analysis examined through power analysis and a population simulation. *Neuroimage* 2005; **24**: 163-173 [PMID: 15588607 DOI: 10.1016/j.neuroimage.2004.07.045]
52 **Hutton C**, De Vita E, Ashburner J, Deichmann R, Turner R. Voxel-based cortical thickness measurements in MRI. *Neuroimage* 2008; **40**: 1701-1710 [PMID: 18325790 DOI: 10.1016/j.neuroimage.2008.01.027]
53 **Zilles K**. Architecture of the Human Cerebral Cortex. In Paxinos G, Mai JK, The human nervous system. 2nd ed. San Diego: Elsevier, 2004: 997-1060
54 **Kim JS**, Singh V, Lee JK, Lerch J, Ad-Dab'bagh Y, MacDonald D, Lee JM, Kim SI, Evans AC. Automated 3-D extraction and evaluation of the inner and outer cortical surfaces using a Laplacian map and partial volume effect classification. *Neuroimage* 2005; **27**: 210-221 [PMID: 15896981 DOI: 10.1016/j.neuroimage.2005.03.036]
55 **Rueda A**, Acosta O, Couprie M, Bourgeat P, Fripp J, Dowson N, Romero E, Salvado O. Topology-corrected segmentation and local intensity estimates for improved partial volume classification of brain cortex in MRI. *J Neurosci Methods* 2010; **188**: 305-315 [PMID: 20193712 DOI: 10.1016/j.jneumeth.2010.02.020]
56 **Acosta O**, Bourgeat P, Zuluaga MA, Fripp J, Salvado O, Ourselin S. Automated voxel-based 3D cortical thickness measurement in a combined Lagrangian-Eulerian PDE approach using partial volume maps. *Med Image Anal* 2009; **13**: 730-743 [PMID: 19648050 DOI: 10.1016/j.media.2009.07.003]
57 **Aganj I**, Sapiro G, Parikshak N, Madsen SK, Thompson PM. Measurement of cortical thickness from MRI by minimum line integrals on soft-classified tissue. *Hum Brain Mapp* 2009; **30**: 3188-3199 [PMID: 19219850 DOI: 10.1002/hbm.20740]
58 **Cardoso MJ**, Melbourne A, Kendall GS, Modat M, Hagmann CF, Robertson NJ, Marlow N, Ourselin S. Adaptive neonate brain segmentation. *Med Image Comput Comput Assist Interv* 2011; **14**: 378-386 [PMID: 22003722]
59 **Leroy F**, Mangin JF, Rousseau F, Glasel H, Hertz-Pannier L, Dubois J, Dehaene-Lambertz G. Atlas-free surface reconstruction of the cortical grey-white interface in infants. *PLoS One* 2011; **6**: e27128 [PMID: 22110604 DOI: 10.1371/journal.pone.0027128]
60 **Song T**, Jamshidi MM, Lee RR, Huang M. A modified probabilistic neural network for partial volume segmentation in brain MR image. *IEEE Trans Neural Netw* 2007; **18**: 1424-1432

[PMID: 18220190 DOI: 10.1109/TNN.2007.891635]
61 **Xue H**, Srinivasan L, Jiang S, Rutherford M, Edwards AD, Rueckert D, Hajnal JV. Automatic segmentation and reconstruction of the cortex from neonatal MRI. *Neuroimage* 2007; **38**: 461-477 [PMID: 17888685 DOI: 10.1016/j.neuroimage.2007.07.030]
62 **Zhao L**, Ruotsalainen U, Hirvonen J, Hietala J, Tohka J. Automatic cerebral and cerebellar hemisphere segmentation in 3D MRI: adaptive disconnection algorithm. *Med Image Anal* 2010; **14**: 360-372 [PMID: 20303318 DOI: 10.1016/j.media.2010.02.001]
63 **Pepe A**, Zhao L, Koikkalainen J, Hietala J, Ruotsalainen U, Tohka J. Automatic statistical shape analysis of cerebral asymmetry in 3D T1-weighted magnetic resonance images at vertex-level: application to neuroleptic-naïve schizophrenia. *Magn Reson Imaging* 2013; **31**: 676-687 [PMID: 23337078 DOI: 10.1016/j.mri.2012.10.021]
64 **Hyde DE**, Duffy FH, Warfield SK. Anisotropic partial volume CSF modeling for EEG source localization. *Neuroimage* 2012; **62**: 2161-2170 [PMID: 22652021 DOI: 10.1016/j.neuroimage.2012.05.055]
65 **Wu Y**, Warfield SK, Tan IL, Wells WM, Meier DS, van Schijndel RA, Barkhof F, Guttmann CR. Automated segmentation of multiple sclerosis lesion subtypes with multichannel MRI. *Neuroimage* 2006; **32**: 1205-1215 [PMID: 16797188 DOI: 10.1016/j.neuroimage.2006.04.211]
66 **Li W**, Tian J, Li E, Dai J. Robust unsupervised segmentation of infarct lesion from diffusion tensor MR images using multiscale statistical classification and partial volume voxel reclassification. *Neuroimage* 2004; **23**: 1507-1518 [PMID: 15589114 DOI: 10.1016/j.neuroimage.2004.08.009]
67 **Meier DS**, Guttmann CRG. Time-series analysis of mri intensity patterns in multiple sclerosis. *Neuroimage* 2003; **20**: 1193-1209 [DOI: 10.1016/S1053-8119(03)00354-9]
68 **Khademi A**, Venetsanopoulos A, Moody AR. Robust white matter lesion segmentation in FLAIR MRI. *IEEE Trans Biomed Eng* 2012; **59**: 860-871 [PMID: 22203699 DOI: 10.1109/TBME.2011.2181167]
69 **Wei X**, Warfield SK, Zou KH, Wu Y, Li X, Guimond A, Mugler JP, Benson RR, Wolfson L, Weiner HL, Guttmann CR. Quantitative analysis of MRI signal abnormalities of brain white matter with high reproducibility and accuracy. *J Magn Reson Imaging* 2002; **15**: 203-209 [PMID: 11836778 DOI: 10.1002/jmri.10053]
70 **Ahlgren A**, Wirestam R, Sthlberg F, Knutsson L. Automatic brain segmentation using fractional signal modeling of a multiple flip angle, spoiled gradient-recalled echo acquisition. *MAGMA* 2014: In press [PMID: 24639095 DOI: 10.1007/s10334-014-0439-2]
71 **West J**, Warntjes JB, Lundberg P. Novel whole brain segmentation and volume estimation using quantitative MRI. *Eur Radiol* 2012; **22**: 998-1007 [PMID: 22113264 DOI: 10.1007/s00330-011-2336-7]
72 **West J**, Blystad I, Engström M, Warntjes JB, Lundberg P. Application of quantitative MRI for brain tissue segmentation at 1.5 T and 3.0 T field strengths. *PLoS One* 2013; **8**: e74795 [PMID: 24066153 DOI: 10.1371/journal.pone.0074795]
73 **Duyn JH**. The future of ultra-high field MRI and fMRI for study of the human brain. *Neuroimage* 2012; **62**: 1241-1248 [PMID: 22063093 DOI: 10.1016/j.neuroimage.2011.10.065]
74 **Van Leemput K**, Bakkour A, Benner T, Wiggins G, Wald LL, Augustinack J, Dickerson BC, Golland P, Fischl B. Automated segmentation of hippocampal subfields from ultra-high resolution in vivo MRI. *Hippocampus* 2009; **19**: 549-557 [PMID: 19405131 DOI: 10.1002/hipo.20615]

P- Reviewer: Logeswaran R, Sheehan JR, Walter M
S- Editor: Ji FF **L- Editor**: A **E- Editor**: Lu YJ

World Journal of Radiology

Submit a Manuscript: http://www.wjgnet.com/esps/
Help Desk: http://www.wjgnet.com/esps/helpdesk.aspx
DOI: 10.4329/wjr.v6.i11.865

World J Radiol 2014 November 28; 6(11): 865-873
ISSN 1949-8470 (online)

REVIEW

Multimodality imaging of renal inflammatory lesions

Chandan J Das, Zohra Ahmad, Sanjay Sharma, Arun K Cupta

Chandan J Das, Zohra Ahmad, Sanjay Sharma, Arun K Cupta, Department of Radiodiagnosis, All India Institute of Medical Sciences, New Delhi, Delhi 110029, India
Author contributions: All the authors solely contributed to this paper.
Correspondence to: Sanjay Sharma, MD, Department of Radiodiagnosis, All India Institute of Medical Sciences, Ansari Nagar East, Gautam Nagar, New Delhi, Delhi 110029, India. drssharma@hotmail.com
Telephone: +91-98-11687277 **Fax:** +91-98-11687277
Received: April 3, 2014 **Revised:** August 19, 2014
Accepted: September 6, 2014
Published online: November 28, 2014

Abstract

Spectrum of acute infections includes acute pyelonephritis, renal and perirenal abscesses, pyonephrosis, emphysematous pyelonephritis and emphysematous cystitis. The chronic renal infections that we routinely encounter encompass chronic pyelonephritis, xanthogranulomatous pyelonephritis, and eosinophilic cystitis. Patients with diabetes, malignancy and leukaemia are frequently immunocompromised and more prone to fungal infections *viz*. angioinvasive aspergillus, candida and mucor. Tuberculosis and parasitic infestation of the kidney is common in tropical countries. Imaging is not routinely indicated in uncomplicated renal infections as clinical findings and laboratory data are generally sufficient for making a diagnosis. However, imaging plays a crucial role under specific situations like immunocompromised patients, treatment non-responders, equivocal clinical diagnosis, congenital anomaly evaluation, transplant imaging and for evaluating extent of disease. We aim to review in this article the varied imaging spectrum of renal inflammatory lesions.

Key words: Imaging modalities; Renal infection; Cystitis; Pyelonephritis; Pyonephrosis; Xanthogranulomatous; Magnetic resonance imaging

Core tip: Imaging in renal infections is challenging, given the relatively non-specific nature of findings in majority of the cases. A careful assessment of clinical situation in question is essential to accurately choose the imaging modality which would provide most information. In this review we discuss the appropriateness of specific imaging modalities, to allow the radiologist to choose the best modality for a given clinical situation. In addition, some entities such as acute pyelonephritis, Xanthogranulomatous pyelonephritis and emphysematous pyelonephritis have some specific imaging features. In this review we describe and illustrate such specific features, to facilitate their recognition when present.

Das CJ, Ahmad Z, Sharma S, Cupta AK. Multimodality imaging of renal inflammatory lesions. *World J Radiol* 2014; 6(11): 865-873 Available from: URL: http://www.wjgnet.com/1949-8470/full/v6/i11/865.htm DOI: http://dx.doi.org/10.4329/wjr.v6.i11.865

INTRODUCTION

Renal infections range from mild to severe, acute to chronic (Table 1) and may be associated with predisposing risk factors like diabetes mellitus, human immunodeficiency virus (HIV), leukemia, vesico-ureteric reflux and staghorn calculi.

Acute infections include acute pyelonephritis which may be focal or diffuse, may resolve with time or worsen to abscess formation depending on the treatment rendered and immune status of the patient. Immunocompromised state might predispose an individual to more severe and life threatening conditions like emphysematous pyelonephritis which may warrant a nephrectomy. An obstructing pathology with a superimposed infection may lead to pyonephrosis for which drainage is the treatment of choice. Renal infections may take a turn for the worse in a chronic irreversibly damaging form like

Figure 1 Acute pyelonephritis in a 40 years old male. A: US shows soft tissue in bilateral PCS (arrowhead) with increased echogenecity of perinephric fat (arrow); B: CECT nephrographic phase shows bilateral enlarged kidneys with heterogeneous enhancement. There is soft tissue thickening and abnormal enhancement of bilateral PCS and ureter (arrow); C: CECT delayed phase shows striated nephrogram (arrow) seen as linear bands of contrast extending from cortex to medulla. US: Ultrasonography; PCS: Pelvicalyceal system; CECT: Contrast-enhanced computed tomography.

Table 1 Spectrum of renal infections

Acute	Chronic	Others
Acute pyelonephritis	Chronic pyelonephritis	Tuberculosis
Focal nephritis	Xanthogranulomatous pyelonephritis	Fungal
Abscess	Malakoplakia	
Emphsematous pyelonephritis	Eosinophilic cystitis	
Papillary necrosis		
Pyonephrosis		

chronic pyelonephritis and xanthogranulomatous pyelonephritis. Tuberculosis involves the kidney with calyceal irregularity being the earliest manifestation, later leading to scarring, fibrosis and infundibular and ureteric stricture formation. Immunocompromised individuals are particularly predisposed to fungal infections, the most common organisms being Candida, Aspergillus and Mucor. Some rare inflammatory conditions encountered are malakoplakia and eosinophilic cystitis.

Acute infection is usually diagnosed based on clinical symptoms and laboratory data without imaging examinations. Hence, imaging is not routinely indicated in uncomplicated renal infections. However, imaging plays a pivotal role in evaluating infections in situations like immunocompromised state, treatment non-responders, congenital anomaly evaluation, and post transplant for evaluating extent of the disease. We wish to review in this article the varied imaging spectrum of renal inflammatory lesions.

IMAGING MODALITIES

Imaging is not routinely indicated in urinary tract infections, however with severe symptoms, high risk immunocompromised state, diabetic patients and antibiotic non-responders, it becomes necessary[1]. Plain radiography may provide evidence of gas in the renal area in emphysematous pyelonephritis or abscess and the typical mass like calcification in end stage renal tuberculosis (Putty kidney). Ultrasound (US) is the initial screening modality and is used for guiding interventions as well. The role of intravenous urography (IVU) has diminished lately, however it still remains the best modality to diagnose calyceal irregularity of early tuberculosis, papillary necrosis and to evaluate congenital anomalies. Computed tomography (CT) is the gold standard for diagnosis and assessment of severity of acute pyelonephritis and its complications. Magnetic resonance imaging (MRI) is indicated in pregnancy and patients with contraindication to iodinated contrast such as transplant recipients. Diffusion weighted MRI (DW-MRI) has been applied to differentiate hydronephrosis from pyonephrosis as well as to detect infected cysts and tumors.

ACUTE PYELONEPHRITIS

Acute pyelonephritis is usually diagnosed based on clinical symptoms and laboratory data without imaging examinations. In many cases of mild acute pyelonephritis, enhanced CT or ultrasonography may show no abnormal findings. The recommended phases of CT scan for evaluating renal infections are a non-contrast scan, nephrographic phase at 50-90 s and excretory phase at 2 min if there is obstruction[2]. Striated nephrogram which is an appearance described for acute pyelonephritis shows discrete rays of alternating hypoattenuation and hyperattenuation radiating from the papilla to the cortex along the direction of the excretory tubules (Figures 1 and 2). This appearance is ascribed to the decreased flow of contrast due to stasis and eventual hyperconcentration in the infected tubules[3]. Striated nephrogram is not specific and is also seen in some other conditions like renal vein thrombosis, ureteric obstruction and contusion[4]. Pyelonephritis may manifest as wedge shaped zones of decreased attenuation or a hypodense mass in its focal form (Figure 3). The diffuse form of acute pyelonephritis may cause global enlargement, poor enhancement of renal parenchyma, absent excretion of contrast and streakiness of fat. Hemorrhagic bacterial nephritis which is relatively uncommon shows hyperattenuating areas representing parenchymal bleeding on non-contrast scan[5].

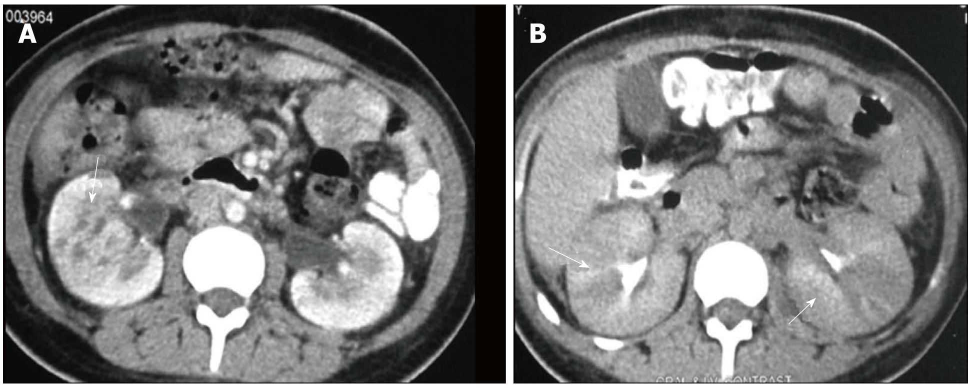

Figure 2 Acute pyelonephritis. A: CECT venous phase shows heterogeneous parenchymal enhancement with pelvic wall thickening (arrow); B: CECT delayed phase shows alternating discrete rays of hyper and hypoattenuation (arrows) giving the appearance of a striated nephrogram. CECT: Contrast-enhanced computed tomography.

Figure 3 Contrast-enhanced computed tomography shows acute pyelonephritis manifesting as a focal wedge shaped hypodensity with surrounding fat stranding as seen in right kidney (arrow).

RENAL ABSCESS

Renal and perinephric abscesses develop as a complication of focal pyelonephritis or hematogenous infection. Early abscess appears as a poorly marginated non-enhancing area of decreased attenuation. A mature abscess shows a sharply marginated, complex cystic mass with necrosis and a peripheral enhancing rim[6]. US may show internal echoes, septations and loculations (Figure 4). DW-MRI can readily pick up abscesses showing restriction of diffusion (Figure 5). In a transplant patient DW-MRI has an important role to play as contrast may be contraindicated due to deranged renal parameters (Figure 6).

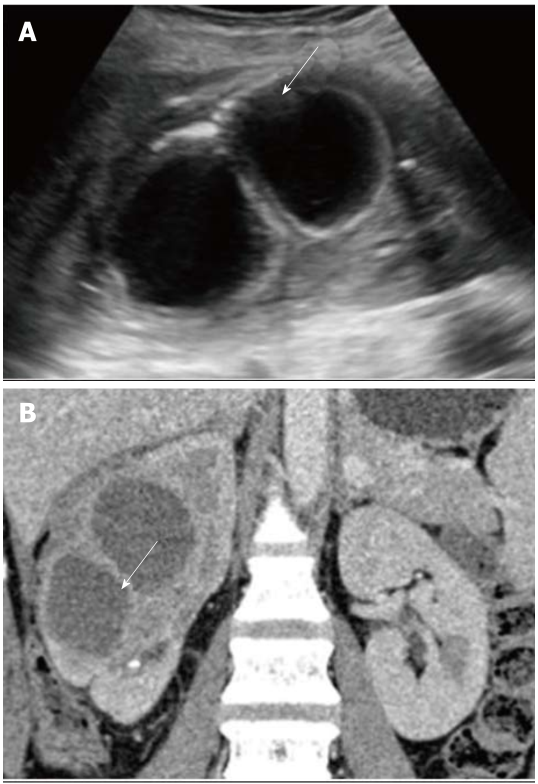

Figure 4 Mature abscess. A: US shows a complex cystic lesion with thick walls in right kidney; B: CECT shows a sharply marginated area of low attenuation due to parenchymal necrosis with peripheral enhancing rim that suggest a mature abscess. US: Ultrasonography; CECT: Contrast-enhanced computed tomography.

PYONEPHROSIS

Pyonephrosis is pus collection in an obstructed collecting system, the cause of obstruction being calculus, stricture, tumour or congenital anomaly. US shows dilated pelvicalyceal system (PCS) with debris and fluid-fluid levels within (Figure 7)[1]. On CT, high density of urine in dilated PCS with contrast layering, parenchymal or perinephric inflammatory changes and thickening of pelvic wall suggests infection (Figure 8). DW-MRI may have an additional role in distinguishing hydronephrosis from pyonephrosis as pyonephrosis tends to show restricted diffusion (Figure 9)[7]. Contrast enhanced MRI may show enhancement and wall thickening of the renal pelvis (Figure 10).

XANTHOGRANULOMATOUS PYELONEPHRITIS

Xanthogranulomatous pyelonephritis is a chronic granulomatous process commonly associated with recurrent

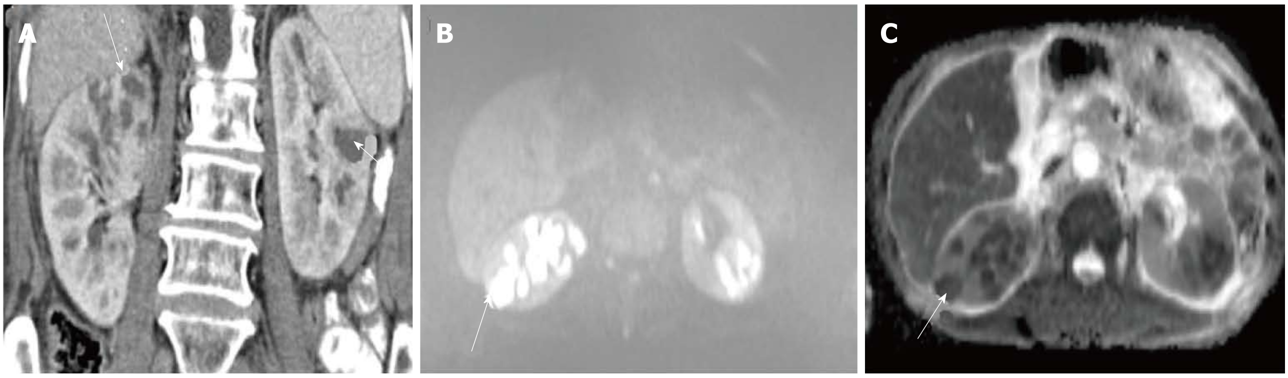

Figure 5 Diffusion weighted magnetic resonance imaging. A: CECT of a diabetic middle aged male shows multiple peripherally enhancing lesions in bilateral kidneys (arrows). B, C: DW-MRI (b = 1000) (B) and corresponding ADC maps (C) show that the lesions have restricted diffusion. Aspiration revealed the pyogenic nature of the abscess. There was excellent response to antibiotics. CECT: Contrast-enhanced computed tomography; DW-MRI: Diffusion weighted magnetic resonance imaging.

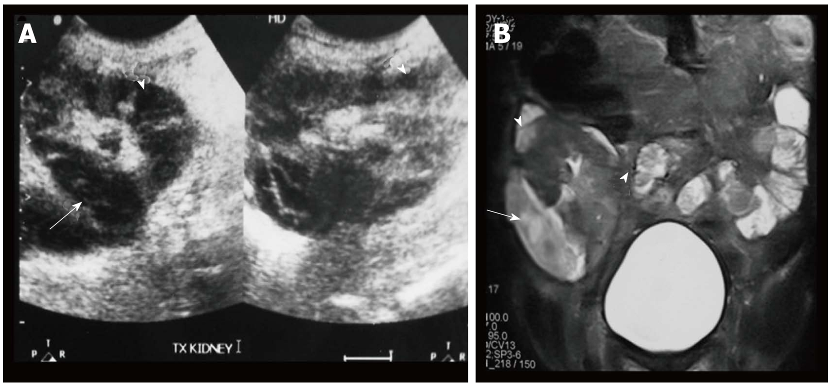

Figure 6 Acute pyelonephritis in transplant kidney. A: USG of transplanted kidney in a 25 years old patient shows multiple hypoechoic lesions (arrowheads) within the cortex and one large hypoechoic lesion laterally (arrow); B: Coronal T2W MR shows multiple hyperintensities (arrowheads) in the renal cortex and a large well defined abscess (arrow) laterally suggestive of acute pyelonephritis with abscess formation.

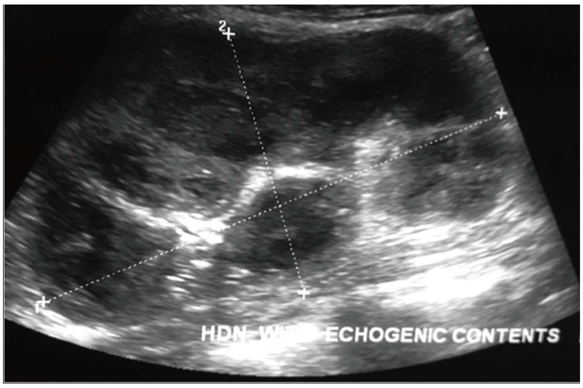

Figure 7 Ultrasonography shows hydronephrosis with echogenic debris within suggestive of pyonephrosis.

E. coli and Proteus mirabilis infection affecting middle aged females and children. Most (90%) of the affected individuals have a staghorn calculus. Pathologically there is replacement of renal parenchyma with foamy macrophages which appear as multiple hypoechoic masses on sonography and as low attenuation rounded masses on CT which represent dilated calyces and abscess cavities (Figure 11) filled with pus and debris[8]. It can manifest as either diffuse (80%) or focal (15%) forms which are treated by nephrectomy and partial nephrectomy respectively[9]. Typical features of xanthogranulomatous pyelonephritis are presence of a central calculus, expansion of the calices with hypodense material in a non-functioning enlarged kidney and inflammatory changes in the perinephric fat. Atypical features include absence of calculi (10%), focal instead of diffuse involvement (10%) and renal atrophy instead of enlargement.

EMPHYSEMATOUS PYELONEPHRITIS

Emphysematous pyelonephritis is a life threatening, necrotising infection with gas formation and is associated with diabetes mellitus or immunocompromised state. The presence of gas is attributed to fermentation by bacteria in the presence of high glucose levels[10]. USG shows non-dependent echoes within the parenchyma and collecting system with dirty shadowing. However, USG is not sensitive to small amounts of gas (Figure 12). CT is performed for evaluating severity, extent of disease, parenchymal destruction, fluid collections and abscess formation. It is divided into two forms depending on severity and prognosis. Type 1 is the more severe type with a mortality rate of 80%. It is characterised by severe parenchymal destruction, intraparenchymal gas and paucity of pus collection (Figure 13). Type 2 is less common and has a lower mortality rate of 20%. It has less parenchymal destruction and renal or perirenal fluid collections (Figure 14). A comparison of the types of emphysema-

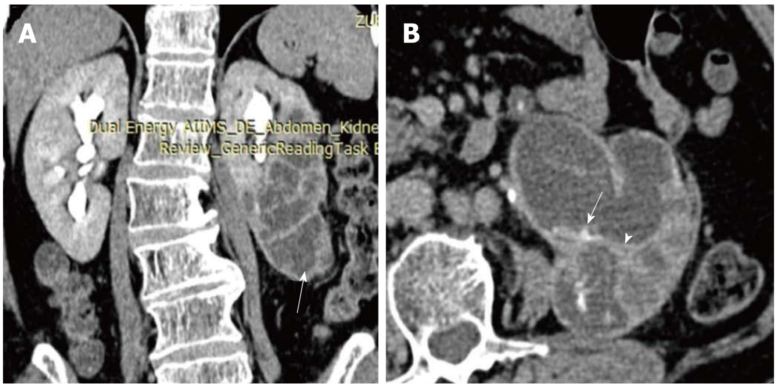

Figure 8 Pyonephrosis in duplex left kidney. Coronal (A) and axial (B) sections of delayed phase CECT shows left duplex kidney with obstruction and hydronephrosis of lower moiety (arrow, A). Walls of the PCS shows thickening and crescentic enhancement (arrowhead, B) suggesting pyonephrosis. PCS: Pelvicalyceal system; CECT: Contrast-enhanced computed tomography.

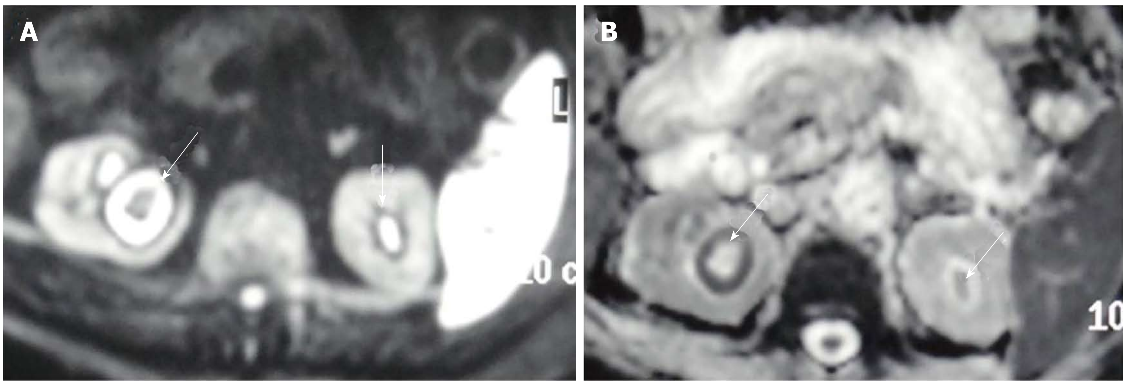

Figure 9 Diffusion weighted magnetic resonance imaging at b = 1000 (A) and corresponding ADC map (B) show hydronephrosis with diffusion restriction suggestive of pyonephrosis (arrows).

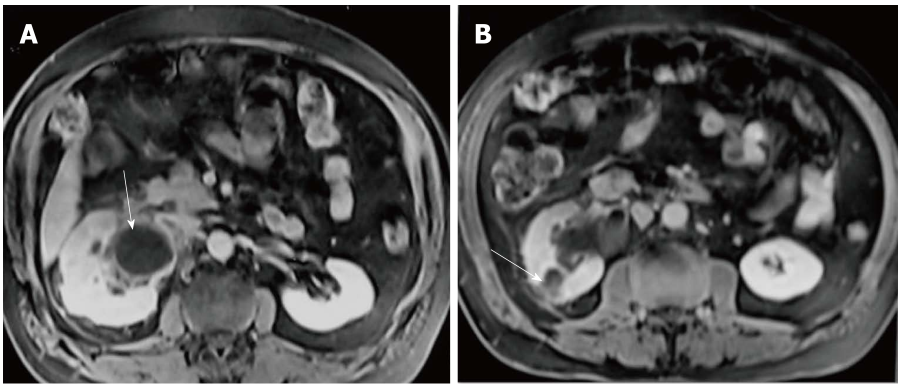

Figure 10 Axial sections of post gadolinium magnetic resonance imaging. A 42 years old male with right hydronephrosis, peripheral enhancement of dilated pelvis (arrow, A) representing pyonephrosis along with a heterogeneously enhancing focal lesion in right kidney (arrow, B) suggestive of focal pyelonephritis.

Table 2 Emphysematous pyelonephritis

	TYPE 1 -33%	TYPE 2 -66%
Parenchymal destruction	Severe – streaky gas radiating from medulla to cortex with crescent of subcapsular gas	Less
Fluid collection	None as the reduced immune response limits pus collection	Renal or perirenal fluid collection is characteristic
Mortality	80%	20%
Treatment	Nephrectomy	Aggressive medical treatment with percutaneous drainage

tous pyelonephritis is presented in Table 2.

Emphysematous pyelitis is usually accompanied by obstruction due to calculus, neoplasm or stricture and 50% of the affected patients are diabetics[10-12]. CT shows gas within the dilated PCS and urinary bladder (Figure 15 A). Emphysematous cystitis shows an air fluid level in

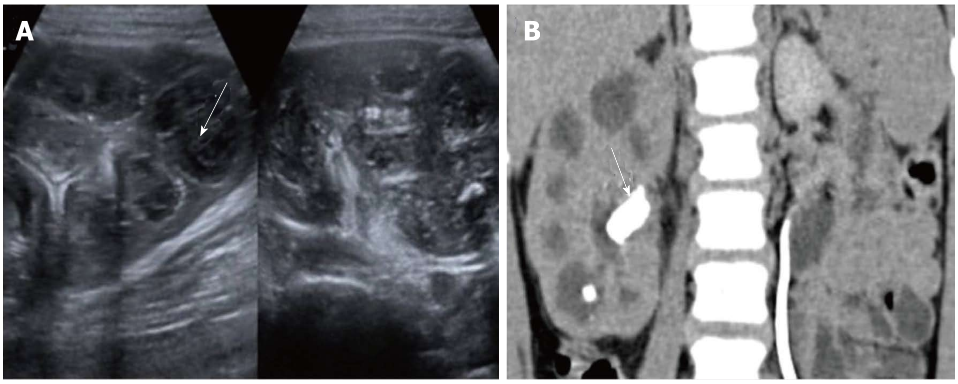

Figure 11 Xanthogranulomatous pyelonephritis. A: USG shows enlarged kidney with parenchyma replaced with multiple hypoechoic masses (arrow, A) comprising inflammatory exudate; B: Computed tomography shows multiple low-attenuation rounded masses, corresponding to either dilated calyces or focal areas of parenchymal destruction with a central staghorn calculus (arrow, B).

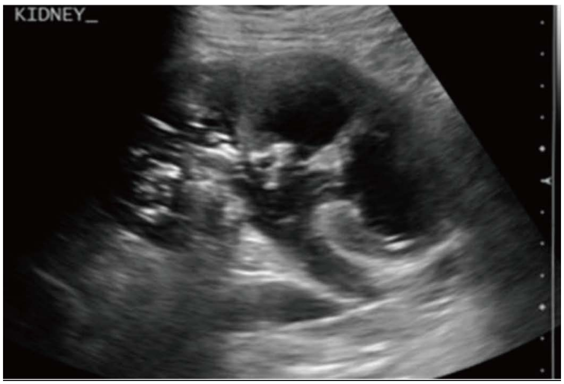

Figure 12 Emphysematous pyelonephritis. Ultrasonography shows dilated calyces with echoes within pelvis and renal parenchyma with dirty shadowing.

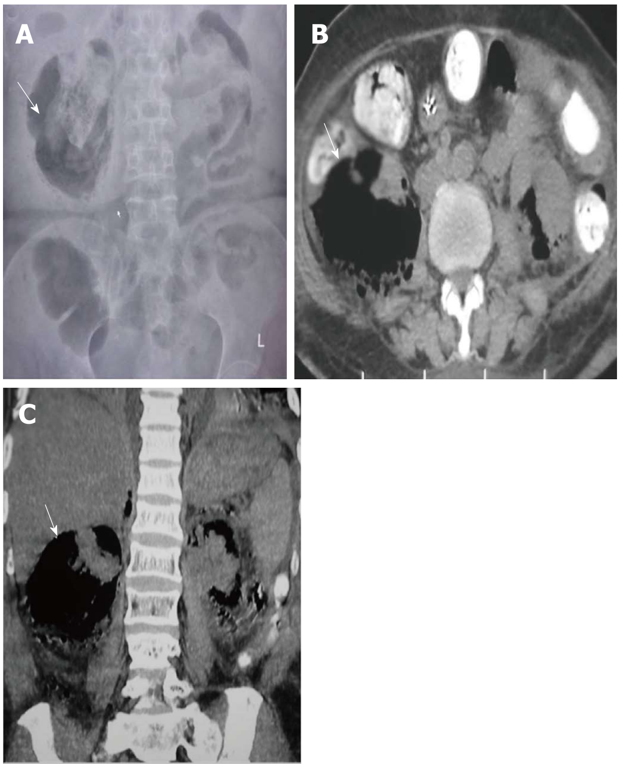

Figure 13 Type 1 emphysematous pyelonephritis. A: Plain abdominal radiograph shows large amount of gas outlining the right kidney (arrow); B, C: Contrast-enhanced computed tomography axial (B) and coronal (C) images show gas pockets and parenchymal destruction destroying and replacing almost the entire right kidney. No perirenal collections are noted.

the bladder lumen or linear streaks of air in the bladder wall (Figure 15B). Before making a diagnosis of emphysematous cystitis, history of instrumentation must be ruled out.

It is important to make the distinction between emphysematous pyelitis and pyelonephritis as the former is a less aggressive infection and does not require nephrectomy. In pyelitis, air is limited to PCS while in pyelonephritis it enters the parenchyma.

CHRONIC PYELONEPHRITIS

Chronic pyelonephritis may be caused by reflux of infected urine in childhood, recurrent infections or as a result of a remote single infection[13]. Imaging shows focal polar scars with underlying calyceal distortion with global atrophy and hypertrophy of residual tissue (Figure 16)[14]. Lobar infarcts can be differentiated by their lack of calyceal involvement. Fetal lobulations are differentiated by depressions lying between calyces rather than overlying calyces

TUBERCULOSIS

Renal tuberculosis (TB) may occur due to hematogenous dissemination. In half of the affected patients of genitourinary TB, there may be no lung involvement[15]. The earliest finding in TB which can be picked up on Intravenous Urography (IVU) is caliectasis with a feathery contour, later appearing as a phantom calyx or a cavity communicating with a deformed calyx (Figure 17A). These findings can also be picked up on CT. Over the course of the disease, the granulomas coalesce forming mass like lesions (tuberculoma) which may rupture into the PCS[16]. Eventually as the disease evolves, fibrosis ensues leading to infundibular stenosis. In the late stage, the kid-

Figure 14 Type 2 Emphysematous pyelonephritis. Contrast-enhanced computed tomography shows extensive inflammatory changes in right kidney and perinephric space with presence of gas within along with perirenal collection. The patient responded to antibiotics and percutaneous drainage.

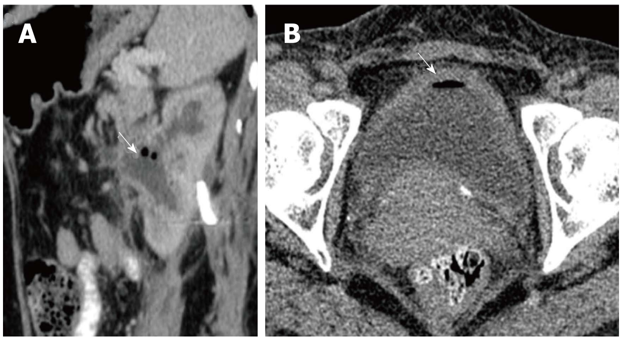

Figure 15 Emphysematous pyelitis and cystitis. A: Para-sagittal reformatted CECT of a 42 years old diabetic lady showing air within dilated PCS with surrounding inflammatory changes; B: Axial CECT shows bladder wall thickening and air within the bladder lumen. PCS: Pelvicalyceal system; CECT: Contrast-enhanced computed tomography.

Figure 16 Coronal contrast-enhanced computed tomography shows atrophic right kidney with multiple cortical scars overlying the dilated calyces. This appearance is typical of chronic pyelonephritis.

ney either becomes calcified or shrunken (putty kidney) (Figure 17B) or an enlarged sac with caseous material (case cavernous type autonephrectomy). Ureteric involvement may manifest as wall thickening causing strictures and shortening leading to a beaded appearance. Bladder involvement results in a contracted thimble shape with

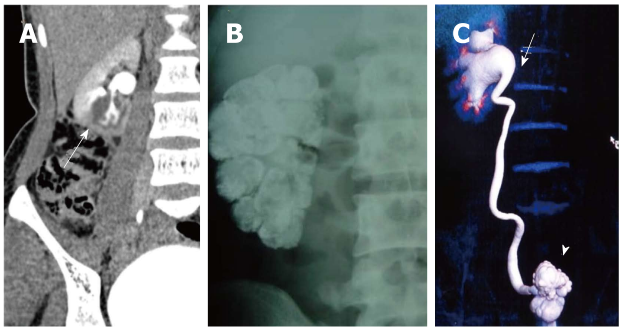

Figure 17 Renal tuberculosis. A: Delayed CECT shows a cavitation at the lower pole of right kidney communicating with the PCS. This finding is fairly typical of GU TB. This adolescent male was a known case of pulmonary tuberculosis; B: Plain abdominal radiograph in a different patient shows diffuse parenchymal calcification of right kidney suggestive endstage autonephrectomy or putty kidney; C: Volume rendered technique image of delayed phase CECT shows a contracted thimble bladder (arrowhead), hiked up right pelvis (arrow) and hydroureteronephrosis. This patient had acid fast bacilli cultured from urine. PCS: Pelvicalyceal system; CECT: Contrast-enhanced computed tomography; TB: Tuberculosis.

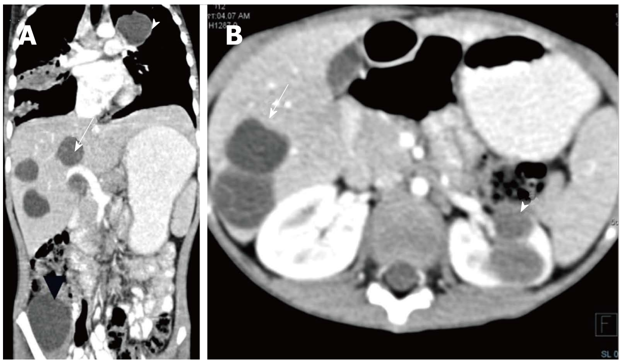

Figure 18 Disseminated hydatidosis. A: Coronal reformatted CECT of a 7 years old boy shows multiple hydatid cysts in lung (white arrowhead), liver (arrow) and right iliacus (black arrowhead); B: Axial CECT shows multiple liver (arrow) and renal hydatid cysts (arrowhead). CECT: Contrast-enhanced computed tomography.

multiple diverticulae (Figure 17C).

PARASITIC INFECTION

Schistomiasis can appear in the acute phase as nodular bladder wall thickening, later causing it to become contracted, fibrotic and thick walled with curvilinear calcifications. This chronic phase of schistosomiasis is considered to be premalignant. Liver is the most common organ involved by hydatid disease while renal involvement comprises only 5% of patients. Hydatid disease affecting the kidney may appear as a unilocular or multilocular cystic lesion(s) with or without peripheral calcification[17] (Figure 18). Occasionally on communication with the pelvicalyceal system (PCS) it may lead to hydatiduria.

FUNGAL INFECTION

Fungal infection of the urinary tract is a severe life threatening infection particularly affecting patients with dia-

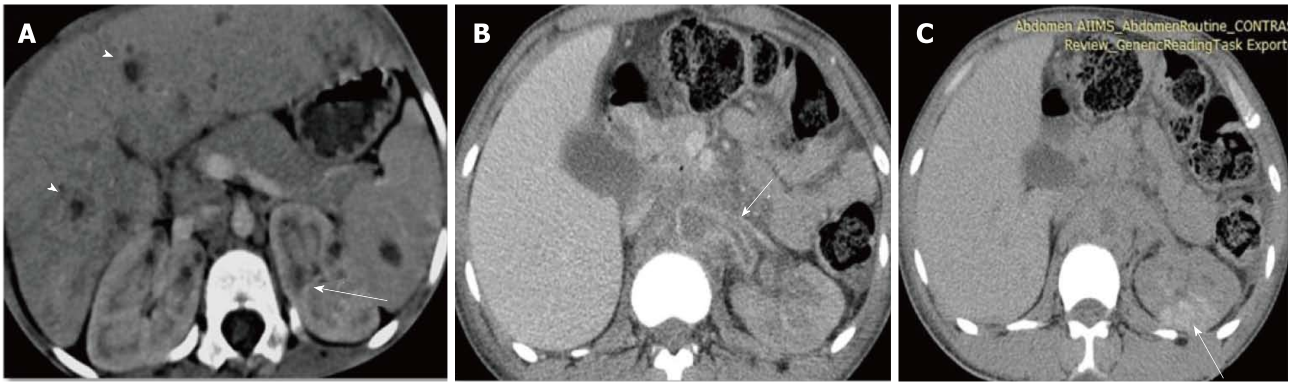

Figure 19 Fungal infection. A: CECT shows liver, spleen and bilateral kidneys studded with small hypodense lesions in a 10 years old leukemia patient who was proven to have Aspergillus infection on aspiration cytology. The patient also had lung involvement with contiguous cardiac thrombus (not shown); B, C: Nephrographic (B) and delayed (C) phase CECT in a 26 years old aplastic anemia patient reveal a poorly enhancing, non-excreting left kidney with perinephric inflammation. Aorta and left renal artery are almost completely occluded by a non-enhancing thrombus (arrow B). On delayed image (Figure C), patchy areas of enhancement (arrow) noted in left kidney are characteristic of acute pyelonephritis. FNAC from the perirenal soft tissue revealed fungal hyphae and diagnosis of angioinvasive fungal infection (mucor) was made and Amphotericin B was started. However patient expired two days later. CECT: Contrast-enhanced computed tomography.

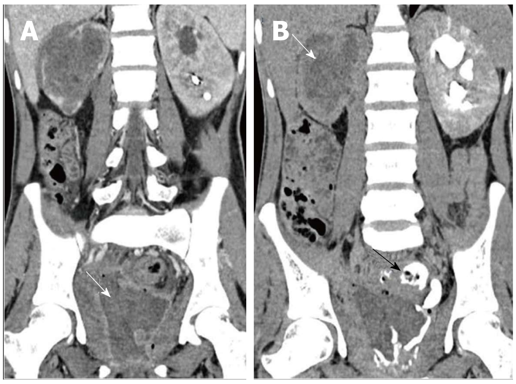

Figure 20 Eosinophilic cystitis. A 25 years old man who presented with hematuria and worsening irritative symptoms over past one year. Clinical suspicion was that of a bladder malignancy. A: Coronal reformatted CECT in nephrographic phase shows diffuse mass like bladder wall thickening and irregularity with air specks in the wall. Mass like soft tissue is replacing entire right kidney with perinephric spread; B: Delayed coronal CECT shows opacification of rectum through a fistulous communication (arrow). Note made of striated nephrogram in left kidney suggesting ongoing acute inflammatory process. Biopsy revealed eosinophilic infiltration and fibrosis within the bladder wall with no evidence of malignancy. CECT: Contrast-enhanced computed tomography.

betes mellitus, haematological malignancy, HIV or other immunocompromised status. The common fungal organisms are Candida and Aspergillus which may be acquired by hematogenous or ascending urinary tract infection. There is formation of multiple renal abscesses appearing as hypoattenuating lesions with a striated nephrogram signifying acute pyelonephritis (Figure 19A). There can also be conglomeration of fungal hyphae and inflammatory cells into a fungal ball which appears as an irregular filling defect in the collecting system[1]. Diagnosis requires demonstration of fungi in tissues. Mucor is a rare organism which has a tendency to invade vessels and cause infarction with high mortality requiring combined surgical and aggressive medical management to improve outcome (Figure 19B, C)[18]. Pneumocystic carini infection in HIV patients presents as diffuse punctate calcifications in kidneys and organs of the reticuloendothelial system[19].

EOSINOPHILIC CYSTITIS

Eosinophilic cystitis is a rare chronic inflammatory disease of urinary bladder due to eosinophil infiltration into the bladder wall leading to fibrosis and muscle necrosis[20]. It clinically presents with hematuria, frequency and irritative symptoms. The mean age at diagnosis is 41.6 years with an equal sex distribution[21].

On imaging, there is diffuse bladder wall thickening which is often more than 10 mm with characteristic preservation of the mucosal line and enhancement on delayed images (Figure 20)[22,23]. This entity is often confused with a neoplastic etiology, therefore biopsy is essential. There may be associated diffuse or segmental bowel wall thickening and hepatic nodules[22].

CONCLUSION

Over the years imaging modalities used for renal infections have evolved from USG and IVU to CT and MRI. CT remains the mainstay in evaluation of inflammatory disease of kidney and urinary bladder. Ultrasonography forms an excellent screening tool for evaluation in the emergency setting. An IVU continues to be invaluable in some indications like tuberculosis. Upcoming role of DW-MRI deserves mention in identifying abscesses and differentiating pyonephrosis from hydronephrosis.

REFERENCES

1 **Kawashima A**, Sandler CM, Goldman SM, Raval BK, Fishman EK. CT of renal inflammatory disease. *Radiographics* 1997; **17**: 851-866; discussion 867-868 [PMID: 9225387 DOI: 10.1148/radiographics.17.4.9225387]

2 **Stunell H**, Buckley O, Feeney J, Geoghegan T, Browne RF, Torreggiani WC. Imaging of acute pyelonephritis in the adult. *Eur Radiol* 2007; **17**: 1820-1828 [PMID: 16937102]

3 **Gold RP,** Mcclennan BL, Kenney PJ, Breatnach ES, Stanley

RJ, Lebowitz RI. Acute infections of the renal parenchyma. In: Pollack HM, editor. Clinical urography. Philadelphia, Pa: Saunders, 1990: 799-821
4 **Saunders HS**, Dyer RB, Shifrin RY, Scharling ES, Bechtold RE, Zagoria RJ. The CT nephrogram: implications for evaluation of urinary tract disease. *Radiographics* 1995; **15**: 1069-185; discussion 1069-1085 [PMID: 7501851]
5 **Rigsby CM**, Rosenfield AT, Glickman MG, Hodson J. Hemorrhagic focal bacterial nephritis: findings on gray-scale sonography and CT. *AJR Am J Roentgenol* 1986; **146**: 1173-1177 [PMID: 3518368 DOI: 10.2214/ajr.146.6.1173]
6 **Browne RF**, Zwirewich C, Torreggiani WC. Imaging of urinary tract infection in the adult. *Eur Radiol* 2004; **14** Suppl 3: E168-E183 [PMID: 14749952 DOI: 10.1007/s00330-003-2050-1]
7 **Cova M**, Squillaci E, Stacul F, Manenti G, Gava S, Simonetti G, Pozzi-Mucelli R. Diffusion-weighted MRI in the evaluation of renal lesions: preliminary results. *Br J Radiol* 2004; **77**: 851-857 [PMID: 15482997]
8 **Loffroy R**, Guiu B, Watfa J, Michel F, Cercueil JP, Krausé D. Xanthogranulomatous pyelonephritis in adults: clinical and radiological findings in diffuse and focal forms. *Clin Radiol* 2007; **62**: 884-890 [PMID: 17662737 DOI: 10.1016/j.crad.2007.04.008]
9 **Kim JC**. US and CT findings of xanthogranulomatous pyelonephritis. *Clin Imaging* 2001; **25**: 118-121 [PMID: 11483422]
10 **Grayson DE**, Abbott RM, Levy AD, Sherman PM. Emphysematous infections of the abdomen and pelvis: a pictorial review. *Radiographics* 2002; **22**: 543-561 [PMID: 12006686]
11 **Kiris A,** Ozdemir H, Bozgeyik Z, Kocakoc E. Ultrasonographic target appearance due to renal calculi containing gas in emphysematous pyelitis. *Eur J Radiol Extra* 2004; **52:** 119-21 [DOI: 10.1016/j.ejrex.2004.09.011]
12 **Joseph RC**, Amendola MA, Artze ME, Casillas J, Jafri SZ, Dickson PR, Morillo G. Genitourinary tract gas: imaging evaluation. *Radiographics* 1996; **16**: 295-308 [PMID: 8966288]
13 **Craig WD,** Wagner BJ, Travis MD. Pyelonephritis: Radiologic-Pathologic review in adults. *Radiographics* 2008; **28:** 255–276 [PMID: 18203942 DOI: 10.1148/rg.281075171]
14 **Goldman SM**. Acute and chronic urinary infection: present concepts and controversies. *Urol Radiol* 1988; **10**: 17-24 [PMID: 3043871 DOI: 10.1007/bf02926529]
15 **Becker JA**. Renal tuberculosis. *Urol Radiol* 1988; **10**: 25-30 [PMID: 3043873 DOI: 10.1007/bf02926530]
16 **Hammond NA**, Nikolaidis P, Miller FH. Infectious and inflammatory diseases of the kidney. *Radiol Clin North Am* 2012; **50**: 259-270, vi [PMID: 22498442 DOI: 10.1016/j.rcl.2012.02.002]
17 **Pedrosa I**, Saíz A, Arrazola J, Ferreirós J, Pedrosa CS. Hydatid disease: radiologic and pathologic features and complications. *Radiographics* 2000; **20**: 795-817 [PMID: 10835129]
18 **Sharma R**, Shivanand G, Kumar R, Prem S, Kandpal H, Das CJ, Sharma MC. Isolated renal mucormycosis: an unusual cause of acute renal infarction in a boy with aplastic anaemia. *Br J Radiol* 2006; **79**: e19-e21 [PMID: 16823048 DOI: 10.1259/bjr/17821080]
19 **Radin DR**, Baker EL, Klatt EC, Balthazar EJ, Jeffrey RB, Megibow AJ, Ralls PW. Visceral and nodal calcification in patients with AIDS-related Pneumocystis carinii infection. *AJR Am J Roentgenol* 1990; **154**: 27-31 [PMID: 2104720 DOI: 10.2214/ajr.154.1.2104720]
20 **Teegavarapu PS**, Sahai A, Chandra A, Dasgupta P, Khan MS. Eosinophilic cystitis and its management. *Int J Clin Pract* 2005; **59**: 356-360 [PMID: 15857336]
21 **Pomeranz A**, Eliakim A, Uziel Y, Gottesman G, Rathaus V, Zehavi T, Wolach B. Eosinophilic cystitis in a 4-year-old boy: successful long-term treatment with cyclosporin A. *Pediatrics* 2001; **108**: E113 [PMID: 11731640 DOI: 10.1542/peds.108.6.e113]
22 **Kim MS**, Park H, Park CS, Lee EJ, Rho MH, Park NH, Joh J. Eosinophilic cystitis associated with eosinophilic enterocolitis: case reports and review of the literature. *Br J Radiol* 2010; **83**: e122-e125 [PMID: 20505026 DOI: 10.1259/bjr/36109223]
23 **Leibovitch I**, Heyman Z, Ben Chaim J, Goldwasser B. Ultrasonographic detection and control of eosinophilic cystitis. *Abdom Imaging* 1994; **19**: 270-271 [PMID: 8019361 DOI: 10.1007/bf00203525]

P- Reviewer: Gao BL, Tsushima Y **S- Editor**: Song XX
L- Editor: A **E- Editor**: Lu YJ

World Journal of Radiology

Submit a Manuscript: http://www.wjgnet.com/esps/
Help Desk: http://www.wjgnet.com/esps/helpdesk.aspx
DOI: 10.4329/wjr.v6.i11.874

World J Radiol 2014 November 28; 6(11): 874-880
ISSN 1949-8470 (online)

MINIREVIEWS

Impact of dose calculation algorithm on radiation therapy

Wen-Zhou Chen, Ying Xiao, Jun Li

Wen-Zhou Chen, Ying Xiao, Jun Li, Department of Radiation Oncology, Jefferson Medical College, Philadelphia, PA 19107, United States
Author contributions: All three authors contributed to manuscript preparation
Supported by In part, under a grant with the Pennsylvania Department of Health
Correspondence to: Jun Li, PhD, Department of Radiation Oncology, Jefferson Medical College, 111 South 11th St., Philadelphia, PA 19107, United States. jun.li@jefferson.edu
Telephone: +1-215-9557945 Fax: +1-215-5032386
Received: May 8, 2014 Revised: August 4, 2014
Accepted: September 23, 2014
Published online: November 28, 2014

Abstract

The quality of radiation therapy depends on the ability to maximize the tumor control probability while minimizing the normal tissue complication probability. Both of these two quantities are directly related to the accuracy of dose distributions calculated by treatment planning systems. The commonly used dose calculation algorithms in the treatment planning systems are reviewed in this work. The accuracy comparisons among these algorithms are illustrated by summarizing the highly cited research papers on this topic. Further, the correlation between the algorithms and tumor control probability/normal tissue complication probability values are manifested by several recent studies from different groups. All the cases demonstrate that dose calculation algorithms play a vital role in radiation therapy.

Key words: Dose calculation; Algorithm; Radiation therapy; Tumor control probability; Normal tissue complication probability

Core tip: This paper is a review of the impact of current commercial dose calculation algorithms on radiation therapy, with a focus on discussing the impact on tumor control probability and normal tissue complication probability.

Chen WZ, Xiao Y, Li J. Impact of dose calculation algorithm on radiation therapy. *World J Radiol* 2014; 6(11): 874-880 Available from: URL: http://www.wjgnet.com/1949-8470/full/v6/i11/874.htm DOI: http://dx.doi.org/10.4329/wjr.v6.i11.874

INTRODUCTION

The quality of radiation therapy depends on the ability to maximize the tumor control probability (TCP) while minimizing the normal tissue complication probability (NTCP) at the same time. Since these two quantities are directly dependent on the absorbed dose in the targets and in the organs at risk (OARs) respectively, accurate knowledge of dose distribution within the patient are crucial in radiation therapy. International Commission on Radiation Units and Measurements (ICRU)[1] has recommended an overall dose accuracy within 5%. Considering the uncertainties resulting from patient setup, machine calibration and dose calculation from treatment planning systems, it is necessary to have a dose calculation algorithm that can predict dose distribution within 3% accuracy.

Accurate calculation of dose distribution in an inhomogeneous medium such as human body is a complicated task, especially for tumors located in the lung. To date, only the Monte Carlo method is considered to be the most accurate algorithm for dose calculation but it requires the greatest processing time. Apart from Monte Carlo method, all other methods make different degrees of approximation and simplification which lead to much faster calculation speed but also result in less accurate dose distribution comparing with the Monte Carlo simulation.

The purpose of this work is to review the effect of dose calculation algorithms on the radiation therapy for different disease sites and special focus is given for the lung region. As mentioned in the American Association of Physicists in Medicine (AAPM) Report No. 85[2], the level of dose differences can be detected clinically. In order to quantify the clinical effects, we review the works on the correlation of dose calculation algorithms with computed values of tumor control probability and normal tissue complication probability. The impact of the accuracy of the algorithms is directly related to the quality of radiation therapy.

DOSE CALCULATION ALGORITHMS

The Monte Carlo dose calculation method is considered to be the most accurate algorithm and has always been used as the generation of benchmark dose distribution with which to compare the results of other less-computer-intensive dose calculation methods[3]. The Monte Carlo method uses photon and electron transport physics to consider the trajectories of individual particles and thus the pattern of dose deposition. Each particle's history is determined by the random number generator and millions of particles' histories are traced. The dose distribution is built by summing the energy deposition in each particle's history.

Apart from the Monte Carlo simulation, all other commonly used dose calculation algorithms can be categorized into two groups[2,4,5]: (1) Methods based on equivalent path length (EPL)[6] scaling or equivalent tissue-air ratio (ETAR)[7] for inhomogeneity corrections. In these methods the changes in lateral transport of electrons are not modeled; and (2) Methods based on convolution techniques, in which the inhomogeneities are handled either by an equivalent path length correction or scaled kernels and the lateral electron transport is considered in an approximate way. In this work, these two types of algorithms are referred to as type (1) and type (2) methods. In type (1) methods, the equivalent path length correction is a one-dimensional method that takes into account of electron density information along a ray path from the source to the point in question. There are two methods: ratio of tissue-air ratios (RTAR) method[2] and power law method which is also referred as modified Batho method[8]. These methods correctly account for the change in the attenuation of the primary dose but not in the scatter contribution, thus result in an overestimation of dose when the electron density is less than unity and an underestimation when the electron density is greater than unity. The equivalent tissue-air ratio method is a three-dimensional correction method which is based on full three-dimensional density information acquired from CT images. This method applies a ray trace to determine the change in the primary dose and calculate the scatter dose based on the three-dimensional density data. Although methods in type (1) do not perform an accurate dose distribution calculation in patients, they are still used by some treatment planning systems for a quick dose calculation to give the planner a rough idea about the absorbed dose and by some dose verification systems to perform a second independent check to catch the gross errors.

In type (2) methods, the model-based convolution/superposition algorithms[9-13] are widely used in commercial radiotherapy treatment planning systems (TPSs), which perform dose calculations with accuracies close to the results of Monte Carlo simulation while taking much less time. All convolution algorithms have two essential components: one representing the energy imparted to the medium by the interactions of primary photons, called Terma (total energy released per unit mass) and one representing the energy deposited about a primary photon interaction site, the kernel. The kernel can be further separated into two parts: the primary kernel which calculates the primary dose and the scatter kernel which calculates the first and multiple scatter doses. The dose at any point can be calculated from the convolution of the Terma with the kernel. In order to account for tissue heterogeneities in a patient, kernel is scaled by radiological distances which are calculated from the material densities defined by CT images. Rigorously speaking, when the scaled kernel is used, the process is not a convolution any more since the kernel is not invariant in space and it is in fact a superposition of varying kernels with the Terma. The treatment planning systems that use the superposition algorithm include, for example, XiO (Elekta, Inc.). Several variations of the convolution/superposition algorithms exist today and two typical and mostly used ones are collapsed cone convolution (CCC) and pencil beam convolution (PBC) techniques[4]. The collapsed cone convolution method uses a polyenergetic Terma and kernel, where the kernel is represented analytically and expressed in polar coordinates. There are a finite number of polar angles with respect to the primary beam. The interaction site can be considered to be at the apex of a set of radially directed lines spreading out in three dimensions. Each line is considered to be the axis of a cone. The kernel along each line is actually the energy deposited within the entire cone collapsed onto the line. The advantage of the CCC method over standard convolution is that the computation time increase with MN^3 as opposed to N^6, where M is the number of cones and N is the number of voxels along one side of the calculation volume. The treatment planning systems that use the CCC method include, for example, Pinnacle (Philips, Inc.) and Oncentra MasterPlan (Nucletron, Inc.). In the pencil beam convolution method, the dose deposited at a point is calculated as a convolution of Terma with a pencil-shape-like kernel which is derived from the measured beam data. The pencil-beam kernel describes the dose distribution of a very narrow beam entering a water phantom along the beam's central axis. Inhomogeneity correction is performed with an equivalent path length correction for the primary dose contribution and a one-dimensional convolution along fan lines for scattered radiation[14,15]. The anisotropic analytical algorithm (AAA)[16,17] used by Eclipse TPS (Varian Medical Systems) is based on the pencil beam convolution technique. The AAA uses spatially variant convolution scatter kernels which are derived from Monte Carlo simulation, and separate modeling for primary photons, scattered photons, and contaminant electrons. Inhomogeneity is handled with radiological scaling of the dose deposition functions in the beamlet direction and electron-density-based scaling of the photon scatter kernels in 16 lateral directions. The final doses are obtained by superposing the doses from the photon and electron convolutions[18,19]. The anisotropic analytical algorithm is an attractive option for routine clinical use because of its relatively short computation time and accuracy comparing with the Monte Carlo method.

COMPARISON OF DOSE CALCULATION ALGORITHMS AND THEIR CLINICAL IMPACT

Comparisons of dose calculation algorithms for clinical treatment disease sites have been studied in many references[4,19-21]. In this review, we first summarize the comparisons of dose calculation algorithms for four commonly treated disease sites, which demonstrate that dose calculation algorithms that can calculate dose accurately in inhomogeneous environment are essential for lung tumor treatment. Then we focus on the dose calculation algorithm for lung tumor treatment planning. Different treatment techniques are discussed. Finally we show the correlation of the algorithms with TCP/NTCP.

In Knöös *et al*[4]'s paper, the authors studied the performance of different dose calculation algorithms from five commercial radiotherapy treatment planning systems for four common treatment disease sites: prostate, head and neck, breast and lung. The Monte Carlo algorithm was used as a benchmark for comparison between different algorithms. Increasing the complexity from the relatively homogeneous pelvic region to the very inhomogeneous lung region resulted in less accurate dose distributions. Improvements in the accuracy of dose calculation were observed when the methods taking into account of volume scatter and changes in electron transport were used, that is, when type (2) algorithms were used. That was especially important when the extension of the irradiated volume was limited such as in the breast case and when low densities were presented such as in the lung case. In the prostate case, no significant differences were found in the results calculated with different algorithms. For instance, when 6 MV was used, the dose to 95% of the PTV was in a range of 96.2% to 100.3% for all studied systems, with an average value of 98.2%. Qualitatively, all the plans which were calculated with different methods, were very similar. The similar situation existed in the head and neck case. The average dose per monitor unit (MU) to the PTV was decreased by 1% for the low energy if more accurate methods, *i.e.*, type (2) methods, were used. This difference was not presented for the higher energy, due to less scatter in the high energy beam. The dose to 95% of the PTV showed no significant change when moving from type (1) methods to type (2) methods for both low and high energies. The ETAR method of type (1) resulted in doses closer to that calculated with type (2) methods, due to the improved scatter integration which took into account the 3D extension of the volume more accurately. In the breast case, two equally weighted opposed tangential beams were used. The average PTV doses were decreased by 0.7% and 1.6% for low and high energies, respectively, when comparing type (1) with type (2) methods. In general, larger differences in dose calculation were found in high energy treatment due to the longer range of electrons, especially in the low density lung tissues. In the pulmonary case, for 6 MV, the average dose per MU to the PTV was decreased by 2.5% when the type (2) methods were used, compared with that calculated with type (1) methods. Changing the energy to high energies increased the difference to 3.7%. The high dose volume within the PTV was decreased by 3.4% and 4.6%, moving from type (1) methods to type (2) methods for low and high energies, respectively. This implies that accurate tumor doses are different from the doses predicted with those methods, and accurate tumor doses needs to be predicted with advanced dose calculation algorithms, *i.e.*, Monte Carlo algorithm. Thus the algorithm directly affects the local control of tumors in lung cancer. That is, less coverage for tumor is presented when more realistic and accurate methods is used. This paper and many other references[19-22] showed that the dose calculation algorithms have a significant impact on radiation therapy for lung cancer treatment.

Remarkable impact of dose calculation algorithms on radiation therapy has been observed in the treatment of lung cancer, when tissue density correction was taken into account. Differences between dose calculations with and without density corrections in the thoracic region have been reported[23-28]. In Xiao *et al*[27]'s paper, a retrospective dosimetric study was carried out based on the treatment plans submitted to Radiation Therapy Oncology Group (RTOG) 0236 clinical trials of non-small-cell lung cancer (NSCLC) treatment with stereotactic body radiotherapy (SBRT). The protocol required each institution to submit two plans: one plan without heterogeneity correction and one plan with heterogeneity correction, with identical MUs. In Xiao *et al*[27]'s study, the authors found that the planning target volume receiving greater than 60 Gy was decreased, on average, by 10.1% when heterogeneity corrections were applied. The maximal dose to any point greater than 2 cm away from the planning target volume increased from 35.2 Gy to 38.5 Gy.

The impact of heterogeneity corrections of dose algorithms on target coverage in the SBRT lung treatment was studied in more details in Ding *et al*[22]'s paper. The dose calculations using four different algorithms were compared with experimental measurements. The pencil beam algorithm with no heterogeneity corrections (PB-

Table 1 Calculated percent mean tumor control probability values (ranges in parentheses) for all algorithms as a function of planning target volume volume

PTV bins (cm^3)	Mean PTV volume (range, cm^3)	*n*	EPL-1D	EPL-3D	AAA	CCC	Acuros	MC
$4 \leqslant v < 10$	7.8 (4.8-9.9)	15	100.0 (100-100)	99.9 (99.6-100)	93.1 (76.3-99.8)	91.3 (63.0-99.9)	91.8 (60.8-99.8)	90.5 (51.1-99.9)
$10 \leqslant v < 20$	15.0 (10.4-19.8)	27	100.0 (99.8-100)	99.9 (99.5-100)	91.3 (61.7-100)	91.3 (50.4-100)	91.4 (65.4-99.9)	91.1 (53.2-100)
$20 \leqslant v < 30$	24.3 (20.4-29.6)	29	98.5 (99.8-100)	98.9 (77.6-100)	92.7 (74.9-99.9)	90.5 (46.4-99.9)	90.9 (65.1-99.9)	91.1 (48.4-99.9)
$30 \leqslant v < 40$	34.9 (30.2-39.8)	18	99.8 (97.4-100)	99.6 (98.2-100)	92.0 (63.4-99.9)	92.1 (69.7-99.9)	90.9 (61.6-99.8)	92.4 (56.3-99.9)
$40 \leqslant v < 60$	47.3 (40.2-58.4)	17	99.5 (93.1-100)	99.1 (95.6-100)	92.6 (78.6-99.9)	91.4 (64.4-99.9)	93.6 (77.6-99.9)	92.3 (63.6-99.9)
$60 \leqslant v < 100$	78.0 (60.4-95.9)	16	99.5 (95.6-100)	99.0 (95.8-100)	92.7 (70.7-99.8)	92.8 (66.2-99.9)	93.4 (70.4-99.8)	94.7 (74.6-99.9)
$V \geqslant 100$	162.4 (100.5-360.2)	11	99.2 (96.1-99.9)	98.7 (95.0-100)	96.3 (89.9-100)	95.6 (91.6-99.8)	95.3 (83.0-99.9)	97.1 (88.8-99.9)

PTV: Planning target volume; EPL-1D: 1-D equivalent path-length (pencil beam-type); EPL-3D: 3-D equivalent-path-length (pencil beam-type); AAA: Anisotropic analytical algorithm; CCC: Collapsed cone convolution-superposition; Acuros: Acuros AXB; MC: Monte Carlo. (Cited from Chetty *et al*[30] 2013).

NC) and with modified Batho heterogeneity corrections (PB-MB), the anisotropic analytical algorithm (AAA) and Monte Carlo simulation were investigated in ten patients' treatment planning. The plans included 8-10 non-opposed photon beams and 2-4 of the beams were non-coplanar. The field sizes ranged from 3.5 cm × 3.5 cm to 6 cm × 6 cm with the mean value close to 4 cm × 4 cm. The mixed 6 and 10 MV energies were used. The authors found that the differences in calculated doses to 95% or 99% of the PTV, between calculations using the PB-NC and the AAA, were within 10% of prescribed dose. Compared to that calculated with the AAA, the minimum doses to 95% of PTV calculated using the PB-MB were overestimated by up to 40% of the prescribed dose. The calculated maximum doses were underestimated by up to 27% using the PB-NC and overestimated by 19% using the PB-MB. The dose distributions near the interface calculated with the AAA agreed with those from Monte Carlo calculations and the measurements.

The above publications demonstrated the impact of dose calculation algorithms on the lung cancer treatment. These comparisons were mainly between type (1) and type (2) methods. The direct comparisons between type (2) algorithms and Monte Carlo simulation have also been done extensively. For instance, in Vanderstraeten *et al*[20]'s study[21], the authors compared the accuracy between Monte Carlo, convolution/superposition, and pencil beam dose calculations for intensity modulated radiation therapy (IMRT) of lung cancer, and they found that the convolution/superposition methods showed an excellent agreement with Monte Carlo method for dose calculation within the target structures, whereas the best agreement in OAR doses was found between collapsed cone convolution model and Monte Carlo simulation. Results from pencil beam algorithm were unsatisfying for both target and OARs. In Li *et al*[28]'s paper, the authors compared superposition algorithm with Monte Carlo method for SBRT non-small-cell lung cancer treatment and they found that the important dosimetric parameter R50 (ratio of 50% prescription isodose volume to PTV) recommended by RTOG 0813 protocol had 12% difference on average between superposition and Monte Carlo calculations.

All these research studies have demonstrated that for dose calculation in lung region the advanced type (2) methods are necessary, and the collapsed cone convolution algorithm and anisotropic analytical algorithm are appropriate options for their relative accurate calculation results compared with the Monte Carlo method.

In the above, we have discussed that the different dose calculation algorithms could give different levels of dose distribution accuracy. Further we will discuss that this different levels of accuracy could be detected clinically, which affect the quality of radiotherapy. The American Association of Physicists in Medicine (AAPM) Report No. 85[2] on tissue inhomogeneity corrections mentioned that a 5% change in dose may result in a significant change in tumor control probability (TCP) and normal tissue complication probabilities (NTCP). In this report, the authors mentioned two examples[29]: A 7% difference in dose delivered to different groups of patients was discovered by a radiation oncologist; and two experiences from the Institut Gustave Roussy, which were related to tumor regression and normal tissue reactions, respectively.

Although it is still a relative new topic, the correlation between dose algorithms and local control, TCP and NTCP, has already been investigated by several groups and more research is expected to be done in the future. In Chetty *et al*[30]'s study, 133 NSCLC patients with stereotactic ablative radiotherapy (SABR)-based treatment were chosen for the correlation study. The correction-based pencil-beam algorithm, model-based convolution/superposition algorithm, and Monte Carlo algorithm were applied for dose calculation. TCP was computed using the Marsden[31,32] model and associations between dose and outcome were inferred. The authors found that model-based mean TCP's were approximately 8%-9%, 6%-8%, and 3%-5% lower than those of correction-based algorithms for volumes < 60, 60-100, and > 100 cm^3, respectively, when the same treatment arrangement were applied. This was because that the advanced type (2) methods simulated the dose deposition physics in a more realistic way than that type (1) methods. Further, the maximum decrement in Monte Carlo-based TCP was about 50% for volumes < 30 cm^3. Variation in TCP rang-

Table 2 Relative differences calculated as (without-with)/with density corrections using each algorithm

	Eclipse AAA	OTP CC	Pinnacle CC	XiO Sup	OTP PB	XiO FFT
Combined lungs						
$NTCP_{Burman}$	-0.29	-0.2	-0.22	-0.25	-0.36	-0.45
$NTCP_{Seppenwoolde}$	-0.19	-0.13	-0.12	-0.15	-0.23	-0.3
Mean dose	-0.08	-0.05	-0.05	-0.06	-0.09	-0.13
V_{20}	-0.06	-0.06	-0.04	-0.03	-0.05	-0.07
Heart						
NTCP	-0.19	-0.15	-0.15	-0.13	-0.17	-0.21
Mean dose	-0.06	-0.05	-0.05	-0.05	-0.06	-0.09
V_{50}	-0.11	-0.1	-0.1	-0.08	-0.08	-0.13
PTV						
Mean dose	-0.06	-0.05	-0.05	-0.05	-0.13	-0.1
D_{01}	-0.05	-0.05	-0.04	-0.04	-0.1	-0.11
D_{99}	-0.07	-0.04	-0.05	-0.05	-0.14	-0.09
GTV						
Mean dose	-0.07	-0.06	-0.06	-0.06	-0.08	-0.1
D_{01}	-0.07	-0.07	-0.06	-0.06	-0.09	-0.11
D_{99}	-0.07	-0.06	-0.06	-0.06	-0.07	-0.1

Negative results indicate lower values when no density corrections are included. Eclipse AAA: Eclipse Anisotropic Analytical Algorithm; OTP CC: Oncentra MasterPlan Collapsed Cone algorithm; Pinnacle CC: Pinnacle Collapsed Cone algorithm; XiO Sup: XiO Multigrid Superposition algorithm; OTP PB: Oncentra MasterPlan Pencil Beam algorithm; XiO FFT: XiO Fast Fourier Transform Convolution algorithm. (Cited from Nielsen *et al*[34] 2011).

Table 3 Clinical impact of dose calculation algorithms

Ref.	Tumor site/technique	Algorithms studied	Results/conclusion
Nielsen *et al*[34], 2011	NSCLC	Eclipse AAA OTP CC Pinnacle CC XiO Sup OTP PB XiO FFT	Differences in dose to target predicted by the different algorithms are of a magnitude. Calculated NTCP values for pneumonitis are more sensitive to the choice of algorithm than mean lung dose and V20
Chandrasekaran *et al*[38], 2011	Lung/3DCRT,SBRT	PBC, Eclipse AAA, Pinnacle CCC, Masterplan PBC and CCC	PBC yielded higher TCP in comparison with other algorithms. For small tumor, TCP was overestimated by 4%-13% by PBC; for large tumor, there was an increase of up to 6%-22%
Liu *et al*[39], 2013	Lung/SABR	EPL, MC	EPL overestimates dose by amounts that substantially decrease TCP in a large proportion. Compared with MC, prescribing based on EPL translated to a median TCP decrement of 4.3% (range, 1.2%-37%) and a > 5% decrement in 46% of tumors
Bufacchi *et al*[33], 2013	Prostate, HN, Lung, Breast /3DCRT	PBC, AAA	NTCP calculated with AAA was lower than the NTCP calculated with PBC, except for the breast treatments
Chetty *et al*[30], 2013	NSCLC/SABR	EPL-1D, EPL-3D, AAA, CCC, Acuros, MC	Average TCP decrements (5%-10%, ranging up to approximately 50%) were observed with model-based algorithms relative to the EPL-based methods

Eclipse AAA: Eclipse Anisotropic Analytical Algorithm; OTP CC: Oncentra MasterPlan Collapsed Cone algorithm; Pinnacle CC: Pinnacle Collapsed Cone algorithm; XiO Sup: XiO Multigrid Superposition algorithm; OTP PB: Oncentra MasterPlan Pencil Beam algorithm; XiO FFT: XiO Fast Fourier Transform Convolution algorithm; EPL: Equivalent path length; MC: Monte Carlo.

es among model-based algorithms is due to the differences in the PTV minimum doses observed in the dose-volume histograms which were the direct products of the calculation algorithms. Though these differences did not have a significant effect on the PTV D95, they had a strong impact on the TCP. The results implied that more advanced algorithms are essential to assess the quality of the treatment clinically in the more realistic way. The detailed results of the percent mean tumor control probability (TCP) values for all algorithms as a function of PTV volume are cited and listed in Table 1.

In Bufacchi *et al*[33]'s study, the focus was shifted to the clinical implication of algorithms on NTCP models for four tumor sites: prostate, head and neck, breast and lung. The pencil beam convolution and anisotropic analytical algorithm were used for 80 treatment plans. The authors found that when the original PBC treatment plans were recalculated using AAA with the same number of monitor units, the NTCP became lower, except for the breast treatments. Further the authors concluded that this difference in NTCP between PBC and AAA treatment plans could be clinically significant. In Nielsen *et al*[34]'s paper, the study was specifically focused on the influence of dose calculation algorithms on NTCP in NSCLC patients. Six dose algorithms from four different treatment planning systems were investigated: Eclipse AAA, Oncentra MasterPlan Collapsed Cone and Pencil Beam, Pinnacle Collapsed Cone, and XiO Multigrid Superposition and Fast Fourier Transform Convolution. NTCP values for heart and lungs were calculated using the relative seriality model[35] and the LKB model[36,37], respectively. The authors found that the influence of density correction on the NTCP values depended on the dose calculation algorithms and the NTCP model parameter set. Compared to mean lung dose (MLD) and V20, the calculated NTCP values for pneumonitis were more sensitive to the calculation algorithms. All these implied that for plan evaluation the algorithms play an extremely important role and the dosimetric parameters such as MLD and V20 might not be sensitive enough for the assessment. The differences of the quantities calculated with and without density correction using each algorithm are cited and listed in Table 2.

To summarize, we list the clinical impact of dose calculation algorithms in Table 3. Five references[30,33,34,38,39] with their results and conclusions are summarized.

CONCLUSION

In this study we reviewed the commonly used dose calculation algorithms: correction-based type (1) methods and model-based type (2) methods. The calculation accuracy of different algorithms illustrated by several studies was summarized. Special focus was given to dose calculation comparison in the lung region. All the research studies demonstrated that for dose calculation in lung region, the advanced type (2) methods are necessary. Further, the accuracy of dose calculation algorithms was correlated to the quantities of TCP/NTCP, and the connection between the algorithms and clinical impact was established. The clinically related TCP/NTCP values are sensitive to the accuracy of dose algorithms. In conclusion, dose calculation algorithms play a vital role in radiation therapy.

REFERENCES

1 **International Commission on Radiation Units and Measurements (ICRU).** Determination of absorbed dose in a patient irradiated by beams of X or gamma rays in radiotherapy procedures. ICRU Report 24. Washington (DC): ICRU, 1976: 67

2 **AAPM.** The American Association of Physicists in Medicine (AAPM) Report 85 Tissue inhomogeneity corrections for MV photon beams. USA: Report of Task Group No. 65 of AAPM, 2004

3 **Metcalfe P**, Kron T, Hoban P. The physics of radiotherapy x-rays and electrons. Madison, WI: Medical Physics Publishing, 2007

4 **Knöös T**, Wieslander E, Cozzi L, Brink C, Fogliata A, Albers D, Nyström H, Lassen S. Comparison of dose calculation algorithms for treatment planning in external photon beam therapy for clinical situations. *Phys Med Biol* 2006; **51**: 5785-5807 [PMID: 17068365 DOI: 10.1088/0031-9155/51/22/005]

5 **Fogliata A**, Vanetti E, Albers D, Brink C, Clivio A, Knöös T, Nicolini G, Cozzi L. On the dosimetric behaviour of photon dose calculation algorithms in the presence of simple geometric heterogeneities: comparison with Monte Carlo calculations. *Phys Med Biol* 2007; **52**: 1363-1385 [PMID: 17301460 DOI: 10.1088/0031-9155/52/5/011]

6 **Milan J**, Bentley RE. The storage and manipulation of radiation dose data in a small digital computer. *Br J Radiol* 1974; **47**: 115-121 [PMID: 4206210 DOI: 10.1259/0007-1285-47-554-115]

7 **Sontag MR**, Cunningham JR. The equivalent tissue-air ratio method for making absorbed dose calculations in a heterogeneous medium. *Radiology* 1978; **129**: 787-794 [PMID: 725060]

8 **Webb S**, Fox RA. Verification by Monte Carlo methods of a power law tissue-air ratio algorithm for inhomogeneity corrections in photon beam dose calculations. *Phys Med Biol* 1980; **25**: 225-240 [PMID: 7384209 DOI: 10.1088/0031-9155/25/2/003]

9 **Boyer A**, Mok E. A photon dose distribution model employing convolution calculations. *Med Phys* 1985; **12**: 169-177 [PMID: 4000072 DOI: 10.1118/1.595772]

10 **Mackie TR**, Scrimger JW, Battista JJ. A convolution method of calculating dose for 15-MV x rays. *Med Phys* 1985; **12**: 188-196 [PMID: 4000075 DOI: 10.1118/1.595774]

11 **Mohan R**, Chui C, Lidofsky L. Differential pencil beam dose computation model for photons. *Med Phys* 1986; **13**: 64-73 [PMID: 3951411 DOI: 10.1118/1.595924]

12 **Ahnesjö A**. Collapsed cone convolution of radiant energy for photon dose calculation in heterogeneous media. *Med Phys* 1989; **16**: 577-592 [PMID: 2770632 DOI: 10.1118/1.596360]

13 **Fogliata A**, Nicolini G, Vanetti E, Clivio A, Cozzi L. Dosimetric validation of the anisotropic analytical algorithm for photon dose calculation: fundamental characterization in water. *Phys Med Biol* 2006; **51**: 1421-1438 [PMID: 16510953 DOI: 10.1088/0031-9155/51/6/004]

14 **Ahnesjo A,** Trepp A. Acquisition of the effective lateral energy fluence distribution for photon beam dose calculations by convolution models. *Phys Med Biol* 1991; 36: 973-985 [DOI: 10.1088/0031-9155/36/7/006]

15 **Ahnesjö A**, Saxner M, Trepp A. A pencil beam model for photon dose calculation. *Med Phys* 1992; **19**: 263-273 [PMID: 1584117 DOI: 10.1118/1.596856]

16 **Ulmer W**, Kaissl W. The inverse problem of a Gaussian convolution and its application to the finite size of the measurement chambers/detectors in photon and proton dosimetry. *Phys Med Biol* 2003; **48**: 707-727 [PMID: 12699190 DOI: 10.1088/0031-9155/48/6/302]

17 **Ulmer W**, Pyyry J, Kaissl W. A 3D photon superposition/convolution algorithm and its foundation on results of Monte Carlo calculations. *Phys Med Biol* 2005; **50**: 1767-1790 [PMID: 15815095 DOI: 10.1088/0031-9155/50/8/010]

18 **Sievinen J,** Ulmer W, Kaissl W. AAA photon dose calculation model in Eclipse. Palo Alto (CA): Varian Medical Systems, 2005

19 **Gagné IM**, Zavgorodni S. Evaluation of the analytical anisotropic algorithm in an extreme water-lung interface phantom using Monte Carlo dose calculations. *J Appl Clin Med Phys* 2007; **8**: 33-46 [PMID: 17592451]

20 **Vanderstraeten B**, Reynaert N, Paelinck L, Madani I, De Wagter C, De Gersem W, De Neve W, Thierens H. Accuracy of patient dose calculation for lung IMRT: A comparison of Monte Carlo, convolution/superposition, and pencil beam computations. *Med Phys* 2006; **33**: 3149-3158 [PMID: 17022207 DOI: 10.1118/1.2241992]

21 **Hasenbalg F**, Neuenschwander H, Mini R, Born EJ. Collapsed cone convolution and analytical anisotropic algorithm dose calculations compared to VMC++ Monte Carlo simulations in clinical cases. *Phys Med Biol* 2007; **52**: 3679-3691 [PMID: 17664570 DOI: 10.1088/0031-9155/52/13/002]

22 **Ding GX**, Duggan DM, Lu B, Hallahan DE, Cmelak A, Malcolm A, Newton J, Deeley M, Coffey CW. Impact of inhomogeneity corrections on dose coverage in the treatment of lung cancer using stereotactic body radiation therapy. *Med Phys* 2007; **34**: 2985-2994 [PMID: 17822007 DOI: 10.1118/1.2745923]

23 **Matsuo Y**, Takayama K, Nagata Y, Kunieda E, Tateoka K, Ishizuka N, Mizowaki T, Norihisa Y, Sakamoto M, Narita Y, Ishikura S, Hiraoka M. Interinstitutional variations in planning for stereotactic body radiation therapy for lung cancer. *Int J Radiat Oncol Biol Phys* 2007; **68**: 416-425 [PMID: 17363190 DOI: 10.1016/j.ijrobp.2006.12.012]

24 **Panettieri V**, Wennberg B, Gagliardi G, Duch MA, Ginjau-

me M, Lax I. SBRT of lung tumours: Monte Carlo simulation with PENELOPE of dose distributions including respiratory motion and comparison with different treatment planning systems. *Phys Med Biol* 2007; **52**: 4265-4281 [PMID: 17664607 DOI: 10.1088/0031-9155/52/14/016]

25 **Lax I**, Panettieri V, Wennberg B, Amor Duch M, Näslund I, Baumann P, Gagliardi G. Dose distributions in SBRT of lung tumors: Comparison between two different treatment planning algorithms and Monte-Carlo simulation including breathing motions. *Acta Oncol* 2006; **45**: 978-988 [PMID: 16982567 DOI: 10.1080/02841860600900050]

26 **Schuring D**, Hurkmans CW. Developing and evaluating stereotactic lung RT trials: what we should know about the influence of inhomogeneity corrections on dose. *Radiat Oncol* 2008; **3**: 21 [PMID: 18662379 DOI: 10.1186/1748-717X-3-21]

27 **Xiao Y**, Papiez L, Paulus R, Timmerman R, Straube WL, Bosch WR, Michalski J, Galvin JM. Dosimetric evaluation of heterogeneity corrections for RTOG 0236: stereotactic body radiotherapy of inoperable stage I-II non-small-cell lung cancer. *Int J Radiat Oncol Biol Phys* 2009; **73**: 1235-1242 [PMID: 19251095 DOI: 10.1016/j.ijrobp.2008.11.019]

28 **Li J**, Galvin J, Harrison A, Timmerman R, Yu Y, Xiao Y. Dosimetric verification using monte carlo calculations for tissue heterogeneity-corrected conformal treatment plans following RTOG 0813 dosimetric criteria for lung cancer stereotactic body radiotherapy. *Int J Radiat Oncol Biol Phys* 2012; **84**: 508-513 [PMID: 22365630 DOI: 10.1016/j.ijrobp.2011.12.005]

29 **Dutreix A**. When and how can we improve precision in radiotherapy? *Radiother Oncol* 1984; **2**: 275-292 [PMID: 6522641 DOI: 10.1016/S0167-8140(84)80070-5]

30 **Chetty IJ**, Devpura S, Liu D, Chen D, Li H, Wen NW, Kumar S, Fraser C, Siddiqui MS, Ajlouni M, Movsas B. Correlation of dose computed using different algorithms with local control following stereotactic ablative radiotherapy (SABR)-based treatment of non-small-cell lung cancer. *Radiother Oncol* 2013; **109**: 498-504 [PMID: 24231237 DOI: 10.1016/j.radonc.2013.10.012]

31 **Nahum AE,** Sanchez-Nieto B. Tumour control probability modelling: basic principles and applications in treatment planning. *Phys Med* 2001; **17:** 13-23

32 **Webb S**, Nahum AE. A model for calculating tumour control probability in radiotherapy including the effects of inhomogeneous distributions of dose and clonogenic cell density. *Phys Med Biol* 1993; **38**: 653-666 [PMID: 8346278 DOI: 10.1088/0031-9155/38/6/001]

33 **Bufacchi A**, Nardiello B, Capparella R, Begnozzi L. Clinical implications in the use of the PBC algorithm versus the AAA by comparison of different NTCP models/parameters. *Radiat Oncol* 2013; **8**: 164 [PMID: 23826854 DOI: 10.1186/1748-717X-8-164]

34 **Nielsen TB**, Wieslander E, Fogliata A, Nielsen M, Hansen O, Brink C. Influence of dose calculation algorithms on the predicted dose distribution and NTCP values for NSCLC patients. *Med Phys* 2011; **38**: 2412-2418 [PMID: 21776775 DOI: 10.1118/1.3575418]

35 **Källman P**, Agren A, Brahme A. Tumour and normal tissue responses to fractionated non-uniform dose delivery. *Int J Radiat Biol* 1992; **62**: 249-262 [PMID: 1355519 DOI: 10.1080/09553009214552071]

36 **Lyman JT**. Complication probability as assessed from dose-volume histograms. *Radiat Res Suppl* 1985; **8**: S13-S19 [PMID: 3867079 DOI: 10.2307/3576626]

37 **Kutcher GJ**, Burman C. Calculation of complication probability factors for non-uniform normal tissue irradiation: the effective volume method. *Int J Radiat Oncol Biol Phys* 1989; **16**: 1623-1630 [PMID: 2722599 DOI: 10.1016/0360-3016(89)90972-3]

38 **Chandrasekaran M,** Panettieri V, Baker C, and Nahum AE. The clinical impact of differences in photon dose algorithms: 3DCRT and SBRT of lung tumors. *Radiother Oncol* 2011; 99: S427-S428 [DOI: 10.1016/S0167-8140(11)71269-5]

39 **Liu MB**, Eclov NC, Trakul N, Murphy J, Diehn M, Le QT, Dieterich S, Maxim PG, Loo BW. Clinical impact of dose overestimation by effective path length calculation in stereotactic ablative radiation therapy of lung tumors. *Pract Radiat Oncol* 2013; **3**: 294-300 [PMID: 24674401 DOI: 10.1016/J.PRRO.2012.09.003]

P- Reviewer: Xiao Y **S- Editor**: Ji FF **L- Editor**: A
E- Editor: Lu YJ

World Journal of Radiology

Submit a Manuscript: http://www.wjgnet.com/esps/
Help Desk: http://www.wjgnet.com/esps/helpdesk.aspx
DOI: 10.4329/wjr.v6.i11.881

World J Radiol 2014 November 28; 6(11): 881-885
ISSN 1949-8470 (online)

OBSERVATIONAL STUDY

Association between facet joint osteoarthritis and the Oswestry Disability Index

Adel Maataoui, Thomas J Vogl, Marcus Middendorp, Konstantinos Kafchitsas, M Fawad Khan

Adel Maataoui, Thomas J Vogl, M Fawad Khan, Institute for Diagnostic and Interventional Radiology, Goethe University, 60590 Frankfurt/ Main, Germany
Marcus Middendorp, Department of Nuclear Medicine, Goethe University, 60590 Frankfurt/Main, Germany
Konstantinos Kafchitsas, Spine Surgery, Asklepios Clinic Lindenlohe, 92421 Schwandorf, Germany
Author contributions: Vogl TJ and Khan MF supervised the project; Maataoui A, Middendorp M, Kafchitsas K, Vogl TJ and Khan MF designed the study and analysed the data; Maataoui A, Middendorp M and Khan MF wrote the main paper; all authors discussed and interpreted the results and implications and commented on the manuscript at all stages.
Correspondence to: Adel Maataoui, MD, Institute for Diagnostic and Interventional Radiology, Goethe University, Frankfurt, Theodor-Stern-Kai 7, 60590 Frankfurt/Main, Germany. adel.maataoui@gmx.de
Telephone: +49-69-63015534 Fax: +49-69-63014222
Received: August 16, 2014 Revised: September 30, 2014
Accepted: October 14, 2014
Published online: November 28, 2014

Abstract

AIM: To investigate the correlation of facet joint osteoarthritis (FJOA) at lumbar levels L4/L5 and L5/S1 and the Oswestry Disability Index (ODI).

METHODS: The study involved lumbar MRIs of 591 patients with a mean age of 47.3 years. The MRIs of the lumbar spine were performed on a 1.5 Tesla scanner (Magnetom® Avanto, Siemens AG, Erlangen, Germany) using a dedicated receive only spine coil. After initial blinding, each dataset was evaluated by 2 board certified radiologist with more than 5 years experience in musculoskeletal imaging. In total 2364 facet joints were graded. Degenerative changes of the facet joints were evaluated according to the 4-point scale as proposed by Weishaupt *et al* Functional status was assessed using the ODI. The index is scored from 0 to 100 and interpreted as follows: 0%-20%, minimal disability; 20%-40%, moderate disability; 40%-60%, severe disability; 60%-80%, crippled; 80%-100%, patients are bedbound. Spearman's coefficient of rank correlation was used for statistical analysis, with significance set at $P < 0.05$.

RESULTS: In total 2364 facet joints at lumbar levels L4/5 and L5/S1 were analysed in 591 individuals. FJOA was present in 97% (L4/L5) and 98% (L5/S1). At level L4/5 (left/right) 17/15 (2.9%/2.5%) were described as grade 0, 146/147 (24.7%/24.9%) as grade 1, 290/302 (49.1%/51.1%) as grade 2 and 138/127 (23.4%/21.5%) as grade 3. At level L5/S1 (left/right) 10/11 (1.7%/1.9%) were described as grade 0, 136/136 (23.0%/23.0%) as grade 1, 318/325 (53.8%/55.0%) as grade 2 and 127/119 (21.5%/20.1%) as grade 3. Regarding the ODI scores, patients' disability had a minimum of 0% and a maximum of 91.11% with an arithmetic mean of 32.77% ± 17.02%. The majority of patients (48.39%) had moderate functional disability (21%-40%). There was no significant correlation between FJOA and ODI on both sides of lumbar level L4/5 and on the left side of lumbar level L5/S1. A weak positive correlation was evaluated between ODI and FJOA on the right side of lumbar level L5/S1.

CONCLUSION: The missing correlation of FJOA and ODI confirms our clinical experience that imaging alone is an insufficient approach explaining low back pain. Clinical correlation is imperative for an adequate diagnostic advance in patients with low back pain.

Key words: Spine; Facet joint osteoarthritis; Magnetic resonance imaging; Low back pain; Oswestry Disability Index

Core tip: Together with secondary disorders facet joint osteoarthritis (FJOA) sets a big burden on health care systems and economics of the western countries. Although FJOA is a common finding on lumbar magnetic resonance imaging (MRI), valid data with regard to correlation with clinical pain scores is missing. The presented study assesses the relationship between increasing grades of FJOA and the Oswestry Disability Score in a large cohort of lumbar MRIs. The results show a weak positive correlation between ODI and FJOA, proving the importance of an adequate clinical approach in patients with low back pain.

Maataoui A, Vogl TJ, Middendorp M, Kafchitsas K, Khan MF. Association between facet joint osteoarthritis and the Oswestry Disability Index. *World J Radiol* 2014; 6(11): 881-885 Available from: URL: http://www.wjgnet.com/1949-8470/full/v6/i11/881.htm DOI: http://dx.doi.org/10.4329/wjr.v6.i11.881

INTRODUCTION

Facet joint osteoarthritis (FJOA) is well known as a cause of low back and lower extremity pain[1-3]. Together with secondary disorders it sets a big burden on health care systems and economics of the western countries[4]. Due to its more precise demonstration of bony details computed tomography (CT) often is the preferred modality in the evaluation of FJOA. Weishaupt *et al*[5] evaluated the significance of magnetic resonance imaging (MRI) in comparison to CT using an established 4-point scale. They found that the interobserver agreement for grading FJOA was moderate for CT and MRI imaging whereas intraobserver agreement was good. Assumed differences of one grade are disregarded, interobserver agreement between both modalities becomes even excellent. In summary, the authors conclude that an additional CT scan is not required in the presence of an MRI examination. The Oswestry Disability Index (ODI) is the most commonly used measure to quantify disability for low back pain[6]. The patient questionnaire contains ten questions concerning the patient's ability to cope with everyday life. The aim of the presented study was the assessment of a relationship between ODI scores and increasing grades of FJOA in a large cohort of lumbar MRIs.

MATERIALS AND METHODS

Study participants

Ethical committee approval was obtained for the study. The indications for MR imaging were suspected disc herniation and facet joint degeneration, respectively. The MRI scans of the lumbar spine were collected over a period of 12 mo in an outpatient setup. Each patient included in the study had a prior history of lower back pain without history of spinal surgery. Patients with proven disc herniation, spinal stenosis, scoliosis and evidence of vertebral fractures were also excluded from the study. Finally, the study involved lumbar MRIs of 591 patients (264 men and 327 women) with a mean age of 47.3 years (range 12-92 years).

Imaging technique

The MRIs of the lumbar spine were performed on a 1.5 Tesla scanner (Magnetom® Avanto, Siemens AG, Erlangen, Germany) using a dedicated receive only spine coil. The imaging protocol included sagittal T2-weighted fast spin-echo images (TR 2850, TE 102) with the following parameters: matrix 512, field of view 300 mm, slice thickness 4 mm, interslice gap 10%, number of excitations 2; axial T2-weighted fast spin-echo images (TR 3550, TE 90) with the following parameters: matrix 448; field of view 210 mm; slice thickness 4 mm; interslice gap 10%, number of excitations 2.

Image evaluation

After initial blinding each dataset was evaluated by two authors (Adel Maataoui and M Fawad Khan), both board certified radiologists with more than 5 years experience in musculoskeletal imaging, in consensus. Since degenerative changes occur most often and earlier in the two lowest motion segments[7], the readers were asked to grade the facet joints at lumbar levels L4/5 and L5/S1, respectively. In total 2364 facet joints were graded.

The facet joints were evaluated according to the 4-point (Grade 0 to Grade Ⅲ) scale as proposed by Weishaupt *et al*[5]: A normal joint space (2-4 mm width) without evidence of osteophytes, hypertrophy of the articular process, subarticular bone erosions or subchondral cysts represented Grade I, while incremental existance of these parameters lead to a higher grade (Figure 1).

ODI

Functional status was assessed using the ODI. Before the examination the supervising physician filled the standardized questionnaire together with the patient. Among questions about the intensity of pain, ability of lifting, ability to care for oneself, ability to walk, ability to sit, ability to stand, social life, sleep quality, and ability to travel are prompted. The index is scored from 0 to 100 and interpreted as follows: 0%-20%, minimal disability; 20%-40 %, moderate disability; 40%-60%, severe disability; 60%-80%, crippled; 80%-100%, patients are bedbound. Due to ethical aspects the question about sexual function was excluded.

Statistical analysis

Statistical analysis was carried out using the BIAS software package (Epsilon publisher, Frankfurt a. M., Germany, http://www.bias-online.de). For statistical analysis Spearman's coefficient of rank correlation and Student's *t*-test were used. In all statistical analysis $P < 0.05$ was considered significant.

RESULTS

Grades of FJOA in the study population

In total 2364 facet joints at lumbar levels L4/5 and L5/

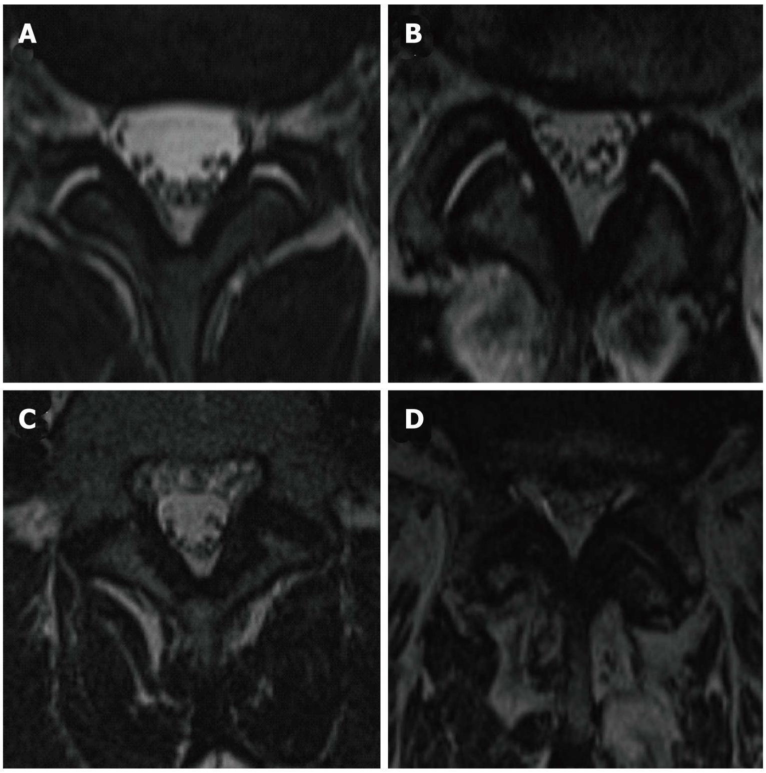

Figure 1 (A-D) Grading system of facet joint osteoarthritis in T2-weighted imaging according to Weishaupt *et al*[5]. Grade 0: Homogenous cartilage and normal (2-4 mm) joint space width; Grade I: Narrowing of the joint space and small osteophytes; Grade II: Narrowing of the joint space, moderate osteophytes and/or subchondral erosions; Grade III: Narrowing of the joint space, large osteophytes and subchondral erosion/ cysts.

Table 1 Grades of facet joint arthritis for lumbar levels L4/5 and L5/S1 *n* (%)

Lumbar level	Grades			
	0	I	II	III
L4/5 left	17 (2.9)	146 (24.7)	290 (49.1)	138 (23.4)
L4/5 right	15 (2.5)	147 (24.9)	302 (51.1)	127 (21.5)
L5/S1 left	10 (1.7)	136 (23.0)	318 (53.8)	127 (21.5)
L5/S1 right	11 (1.9)	136 (23.0)	325 (55.0)	119 (20.1)

S1 were analysed in 591 individuals. FJOA was present in 97% (L4/L5) and 98% (L5/S1). Table 1 summarizes the results.

At level L4/5 (left/right) 17/15 (2.9%/2.5%) were described as grade 0, 146/147 (24.7%/24.9%) as grade 1, 290/302 (49.1%/51.1%) as grade 2 and 138/127 (23.4%/21.5%) as grade 3.

At level L5/S1 (left/right) 10/11 (1.7%/1.9%) were described as grade 0, 136/136 (23.0%/23.0%) as grade 1, 318/325 (53.8%/55.0%) as grade 2 and 127/119 (21.5%/20.1%) as grade 3.

Function score as assessed by ODI

Regarding the ODI scores, patients' disability had a minimum of 0% and a maximum of 91.11% with an arithmetic mean of 32.77% ± 17.02%. There was no statistical difference between the grade of disability in men (31.39% ± 16.72%) and women (33.89% ± 17.21%). The majority of patients (48.39%) had moderate functional disability (21%-40%).

The mean ODI scores for FJOA grade 0, 1, 2 and 3 on the left side of lumbar segment L4/5 were 29.02% ± 21.57%, 31.98% ± 17.16%, 33.24% ± 16.72% and 33.09% ± 17.00%, respectively. The mean ODI scores for FJOA grade 0, 1, 2 and 3 for the right side of lumbar segment L4/5 were 24.44% ± 21.20%, 32.00% ± 16.69%, 33.45% ± 16.93% and 33.04% ± 16.00%, respectively. Table 2 summarizes the results. For grade 0 to 2 of FJOA a discrete but continuous rise of ODI score was detectable. A statistically significant difference between the grade of disability (ODI score) and all grades of FJOA of both sides on lumbar level L5/S1 was not evident.

The mean ODI scores for FJOA grade 0, 1, 2 and 3 on the left side of lumbar segment L5/S1 were 31.56% ± 17.05%, 31.85% ± 18.64%, 32.25% ± 15.75% and 35.17% ± 18.22%, respectively. The mean ODI scores for FJOA grade 0, 1, 2 and 3 for the right side of lumbar segment L5/S1 were 25.86% ± 12.81%, 31.26% ± 17.44%, 32.53% ± 16.38% and 35.80% ± 18.27%, respectively. Table 2 summarizes the results. With increasing grade of FJOA a discrete but continuous rise of ODI score was detectable. A statistically significant difference between the grade of disability (ODI score) and the grade of FJOA of both sides on lumbar level L5/S1 was not evident.

Correlation of ODI and FJOA

There was no significant correlation between FJOA and ODI on both sides of lumbar level L4/5 and on the left side of lumbar level L5/S1: ODI and FJOA left: rho < 0.035, $P < 0.371$; ODI and FJOA right: rho < 0.052, $P < 0.186$; ODI and FJOA left: rho < 0.051, $P < 0.196$.

A weak positive correlation was evaluated between ODI and FJOA on the right side of lumbar level L5/S1:

Table 2 Oswestry Disability Index scores (%) in correlation to facet joint osteoarthritis (grade 0- III)

Lumbar level	Grade FJOA			
	0	I	II	III
L4/5 left	29.02 ± 21.57	31.98 ± 17.16	33.24 ± 16.72	33.09 ± 17.00
L4/5 right	24.44 ± 21.20	32.00 ± 16.69	33.45 ± 16.93	33.04 ± 16.00
L5/S1 left	31.56 ± 17.05	31.85 ± 18.64	32.25 ± 15.75	35.17 ± 18.22
L5/S1 right	25.86 ± 12.81	31.26 ± 17.44	32.53 ± 16.38	35.80 ± 18.27

FJOA: Facet joint arthritis.

Rho < 0.084, $P < 0.035$.

DISCUSSION

Low back pain is a widely spread musculoskeletal disorder in all ages worldwide. The annual prevalence between 25% and 60% makes it a frequent cause of limitation of activity in people younger than 50 years. Furthermore, up to 85% of all people have back pain at some time in life[8]. Despite modern imaging modalities, such as magnetic resonance imaging, for a large proportion of patients with low back pain, it remains difficult to provide a specific diagnosis[9]. The fact that nearly all-lumbar structures are possible sources of low back pain, may serve as a possible explanation[10].

FJOA is a common imaging finding and has been suggested as a major cause of low back and lower extremity pain[1,2]. Since the facet joints are the only synovial joints in the spine with hyaline cartilage overlying subchondral bone, a synovial membrane and a joint capsule, they develop degenerative changes that are equivalent to other peripheral joints. Different studies reported contradicting results about the prevalence of FJOA at lumbar levels. Kalichman *et al*[11] reported that FJOA is more prevalent at L4/5 (45.1%) followed by L5/S1 (38.2%) and L3/4 (30.6%) whereas Abbas *et al*[12] describe a different descending order: L5/S1 (55%), L4/5 (27%) and L3/4 (16%). Additionally, Abbas *et al*[12] describe that FJOA is an age dependant phenomenon, which increases cephalocaudally, whereas they found no correlation of FJOA with sex or the Body mass index[12]. For the assessment of FJOA we applied the 4-point scale as proposed by Weishaupt *et al*[5]. Assuming that grade I changes already represent mild degenerative changes, nearly all patients in our study group showed degenerative alterations of the facet joints. Overall in our study population 97% (L4/5) and 98% (L5/S1) of the examined articulations revealed degenerative changes.

In their cross-sectional study Marchiori *et al*[13] correlated radiographic findings of spinal degeneration of the cervical spine with neck pain and disability in 700 patients[13]. They found that women report higher disability with increasing levels of degeneration while no relation was evident for men. The group of Ashraf *et al*[14] presents similar results. In 150 patients they classified degenerative changes of the lumbar spine on lateral radiographs according to the criteria of Kellgren and Lawrence[14]. Additionally, functional disability was measured using the ODI. They found no significant correlation between the morphological severity of osteoarthritis and ODI scores. A major limitation of the mentioned studies is the fact that degenerative changes of the cervical and lumbar spine were graded on plain film radiographs, which are because of superposition of limited diagnostic value. Additionally, severity of degeneration of intervertebral discs as well as of facet joints was taken into account for scoring. As already mentioned nearly all-lumbar structures are possible sources of low back pain, so that an isolated contemplation of anatomic structures (facet joint, intervertebral disc) and their degenerative changes with regard to clinical importance is necessary. Therefore in the presented study we correlated degenerative changes of the facet joints at lumbar levels L4/5 and L5/S1 with the ODI. The results of this study demonstrate that only for the right-sided facet joints of lumbar level L5/S1 there was a weak correlation between signs of degeneration and clinical disability scores as evaluated by ODI. Taking into account that a huge majority of patients of all ages show degenerative changes of facet joints in the lower motion segments of the lumbar spine, these results should be considered in the future evaluation of lumbar MRIs. In the presence of other degenerative changes like intervertebral disc degeneration, osteochondrosis or Morbus Baastrup the finding of FJOA shouldn't be considered evidentiary as the cause of LBP. In fact, the presented results seem to prove that chronic LBP is a multifactorial disorder, which cannot be explained with a constricted view on one lumbar compartment.

MRI reliably detects age-dependent FJOA of the lumbar spine. Our data revealed no correlation between ODI and FJOA on both sides of lumbar level L4/5 and on the left side of lumbar level L5/S1, while only a weak positive correlation on the right side of lumbar level L5/S1 was evaluated. These findings support the demand, that clinical correlation of apparently explicit imaging findings is not an adjunct only but imperative for an adequate clinical approach in patients suffering from low back pain.

COMMENTS

Background

Facet joint osteoarthritis is well known as a cause of low back and lower extremity pain. Together with secondary disorders it sets a big burden on health care systems and economics of the western countries.

Research frontiers

Despite modern imaging modalities, such as magnetic resonance imaging, it remains difficult to provide a specific diagnosis for a large proportion of patients with low back pain. The fact that nearly all lumbar structures are possible sources of low back pain, may serve as a possible explanation.

Innovations and breakthroughs

The results of the presented study demonstrate that there exists only a weak correlation between signs of degeneration and clinical disability scores as evaluated by the Oswestry Disability Index. Taking into account that a huge majority of patients of all ages show degenerative changes of facet joints in the lower motion segments of the lumbar spine, these results should be considered in the future evaluation of lumbar MRIs.

Applications

With above mentioned innovations in mind, the presence of other degenerative changes like intervertebral disc degeneration, osteochondrosis or Morbus Baastrup the finding of facet joint osteoarthritis shouldn't be considered evidentiary as the cause of low back pain.

Terminology

Since the facet joints are the only synovial joints in the spine with hyaline cartilage overlying subchondral bone, a synovial membrane and a joint capsule, they develop degenerative changes that are equivalent to other peripheral joints. The Oswestry Disability Index is the most commonly used measure to quantify disability for low back pain. The patient questionnaire contains ten questions concerning the patient's ability to cope with everyday life.

Peer review

The manuscript is well written.

REFERENCES

1 **Gellhorn AC**, Katz JN, Suri P. Osteoarthritis of the spine: the facet joints. *Nat Rev Rheumatol* 2013; **9**: 216-224 [PMID: 23147891 DOI: 10.1038/nrrheum]

2 **Goode AP**, Carey TS, Jordan JM. Low back pain and lumbar spine osteoarthritis: how are they related? *Curr Rheumatol Rep* 2013; **15**: 305 [PMID: 23307577 DOI: 10.1007/s11926-012-0305-z]

3 **Suri P**, Dharamsi AS, Gaviola G, Isaac Z. Are facet joint bone marrow lesions and other facet joint features associated with low back pain? A pilot study. *PM R* 2013; **5**: 194-200 [PMID: 23122893 DOI: 10.1016/j.pmrj]

4 **Collaborators USBoD.** The state of US health, 1990-2010: burden of diseases, injuries, and risk factors. *JAMA* 2013; **310**: 591-608 [PMID: 23842577 DOI: 10.1001/jama]

5 **Weishaupt D**, Zanetti M, Boos N, Hodler J. MR imaging and CT in osteoarthritis of the lumbar facet joints. *Skeletal Radiol* 1999; **28**: 215-219 [PMID: 10384992]

6 **Fairbank JC**, Couper J, Davies JB, O'Brien JP. The Oswestry low back pain disability questionnaire. *Physiotherapy* 1980; **66**: 271-273 [PMID: 6450426]

7 **Laplante BL**, DePalma MJ. Spine osteoarthritis. *PM R* 2012; **4**: S28-S36 [PMID: 22632699 DOI: 10.1016/j.pmrj.2012.03.005]

8 **Buchbinder R**, Blyth FM, March LM, Brooks P, Woolf AD, Hoy DG. Placing the global burden of low back pain in context. *Best Pract Res Clin Rheumatol* 2013; **27**: 575-589 [PMID: 24315140 DOI: 10.1016/j.berh.2013.10.007]

9 **Suri P**, Boyko EJ, Goldberg J, Forsberg CW, Jarvik JG. Longitudinal associations between incident lumbar spine MRI findings and chronic low back pain or radicular symptoms: retrospective analysis of data from the longitudinal assessment of imaging and disability of the back (LAIDBACK). *BMC Musculoskelet Disord* 2014; **15**: 152 [PMID: 24886265 DOI: 10.1186/1471-2474-15-152]

10 **Chou D**, Samartzis D, Bellabarba C, Patel A, Luk KD, Kisser JM, Skelly AC. Degenerative magnetic resonance imaging changes in patients with chronic low back pain: a systematic review. *Spine* (Phila Pa 1976) 2011; **36**: S43-S53 [PMID: 21952189 DOI: 10.1097/BRS.0b013e31822ef700]

11 **Kalichman L**, Li L, Kim DH, Guermazi A, Berkin V, O'Donnell CJ, Hoffmann U, Cole R, Hunter DJ. Facet joint osteoarthritis and low back pain in the community-based population. *Spine* (Phila Pa 1976) 2008; **33**: 2560-2565 [PMID: 18923337 DOI: 10.1097/BRS.0b013e318184ef95]

12 **Abbas J**, Hamoud K, Peleg S, May H, Masharawi Y, Cohen H, Peled N, Hershkovitz I. Facet joints arthrosis in normal and stenotic lumbar spines. *Spine* (Phila Pa 1976) 2011; **36**: E1541-E1546 [PMID: 21270684 DOI: 10.1097/BRS.0b013e318210c889]

13 **Marchiori DM**, Henderson CN. A cross-sectional study correlating cervical radiographic degenerative findings to pain and disability. *Spine* (Phila Pa 1976) 1996; **21**: 2747-2751 [PMID: 8979320]

14 **Ashraf A**, Farahangiz S, Pakniat Jahromi B, Setayeshpour N, Naseri M. Correlation between Degree of Radiologic Signs of Osteoarthritis and Functional Status in Patients with Chronic Mechanical Low Back Pain. *Malays J Med Sci* 2014; **21**: 28-33 [PMID: 24876804]

P- Reviewer: Razek AAKA, Teli MGA **S- Editor**: Ji FF
L- Editor: A **E- Editor**: Lu YJ

World Journal of Radiology

Submit a Manuscript: http://www.wjgnet.com/esps/
Help Desk: http://www.wjgnet.com/esps/helpdesk.aspx
DOI: 10.4329/wjr.v6.i11.886

World J Radiol 2014 November 28; 6(11): 886-889
ISSN 1949-8470 (online)

CASE REPORT

Truncus arteriosus: Diagnosis with dual-source computed tomography angiography and low radiation dose

Mustafa Koplay, Derya Cimen, Mesut Sivri, Osman Güvenc, Derya Arslan, Alaaddin Nayman, Bulent Oran

Mustafa Koplay, Mesut Sivri, Alaaddin Nayman, Department of Radiology, Medical Faculty of Selcuk University, 42031 Konya, Turkey
Derya Cimen, Osman Güvenc, Derya Arslan, Bulent Oran, Department of Pediatric Cardiology, Medical Faculty of Selcuk University, 42031 Konya, Turkey
Author contributions: All authors contributed to this paper.
Correspondence to: Mustafa Koplay, MD, Department of Radiology, Medical Faculty of Selcuk University, The Central Campus, Ardicli Street, 42031 Konya, Turkey. koplaymustafa@hotmail.com
Telephone: +90-332-2243800 Fax: +90-332-2654728
Received: June 29, 2014 Revised: September 20, 2014
Accepted: October 1, 2014
Published online: November 28, 2014

Abstract

Truncus arteriosus is an uncommon congenital cardiac abnormality which is characterized by a single arterial trunk origin from the heart that supplies both the systemic, pulmonary and coronary circulation. We present a preterm newborn female patient with type 2 truncusarteriosus, left superior vena cava and aberrant subclavian artery diagnosed with low dose dual-source cardiac computed tomography (CT). We discuss that low dose dual-source cardiac CT has more advantages than other imaging methods and it is an important modality for assessment of patients with conotruncal anomalies such as truncusarteriosus.

Key words: Truncusarteriosus; Type 2; Dual-source computed tomography; Angiography; Radiation dose

Core tip: Truncus arteriosus is an uncommon congenital cardiac abnormality which is characterized by a single arterial trunk origin from the heart that supplies both the systemic, pulmonary and coronary circulation. We discuss that low dose dual-source cardiac computed tomography has more advantages than other imaging methods and it is an important modality for assessment of patients with conotruncal anomalies such as truncusarteriosus.

Koplay M, Cimen D, Sivri M, Güvenc O, Arslan D, Nayman A, Oran B. Truncus arteriosus: Diagnosis with dual-source computed tomography angiography and low radiation dose. *World J Radiol* 2014; 6(11): 886-889 Available from: URL: http://www.wjgnet.com/1949-8470/full/v6/i11/886.htm DOI: http://dx.doi.org/10.4329/wjr.v6.i11.886

INTRODUCTION

Truncus arteriosus is an uncommon congenital cardiac *abnormality* which is characterized by a single arterial trunk origin from the ventricle which occurs due to the failure of conotruncalseptation during development of the fetus. It occurs in approximately 2% of all congenital cardiac anomalies and it is seen higher in males than females[1]. This arterial trunk enables systemic, pulmonary, and coronary circulation. In general, the common trunk is combined with a large, sub arterial ventricular septal defect (VSD) of infundibular type to providethe completion of circulatory flow circuit[2]. Less often, it may originate completely right or left ventricle[3]. Several different abnormalities are described with truncusarteriosus that lead to differences in diagnosis and treatment such as the interruption of aortic arch, structural abnormalities of the truncal valve, coronary artery abnormalities, and much more rarely, right aortic arch, double aortic arch, left superior vena cava, secundum atrial septal defect (ASD), aberrant subclavian artery and complete atrioventricular septal defect. Prenatal ultrasound, echocardiography, catheter cardiac angiography, computerized tomography (CT) and magnetic resonance imaging (MRI) can be used for diagnosis of congenital cardiovascular diseases[4]. The purpose of this study was to present a case of TA arising from completely right ventricle with left superior vena cava and aberrant subclavian artery and to describe the advantages of low dose dual-source CT angiography in diagnosis.

CASE REPORT

A three-day preterm female infant was referred to our clinic with cleft lip-palate and on suspicion of cardiac abnormality. She was born at 36th week of gestation by caesarian delivery with the birth-weight of 2600 g from a 33-year-old woman. Physical examination showed central cyanosis and grade 2/6 systolic murmur at the apex. Respiratory rate was 48 breaths/min, and heart rate was 160 beats/min. The lungs found clear by auscultation and the liver was palpable 4 cm under the right costal margin. Arterial blood gas results revealed that PaO_2 was 40.6 mmHg, $PaCO_2$ as 16.9 mmHg, and O2SAT as 84%. Transthoracic echocardiography showed the secundum type ASD, peri-membraneous VSD, and single arterial trunk.

In order to demonstrate such congenital anomalies and vascular structures in detail, multi-detector computerized tomography (MDCT) was used on a dual-source 128-MDCT scanner (Somatom Definition Flash, Siemens Healthcare, Germany). No medication was administered for sedation. Scans were acquired by 128 mm × 0.625 mm collimation, 3 mm slice thickness, 0.6 mm reconstruction slice thickness, and 0.3 mm reconstruction interval, 80 kVp, 25 mA and a helical pitch of 3.4. Non-ionic contrast medium (1.5 mL/kg) was applied by an automatic injector at a rate of 1 mL/s. CT scan was obtained from the arcus aorta level towards the diaphragmatic face of the heart in prospectively electrocardiography (ECG)-triggered high-pitch spiral mode (flash spiral technique). After the traditional images of the patient were acquired on axial plane and were evaluated in detail. In addition, multiplanar reconstructions (MPR) maximum intensity projection (MIP) and Three dimensional (3D) volume rendering (3D VR) images were used for evaluating of the anomalies by using special computerized software (Syngovia, 2011). MDCT showed secundum type ASD and peri-membraneous VSD as echocardiography. Additionally, there was a single arterial trunk origin from the right ventricle. Left and right branched pulmonary arteriesweredivided into the posterior aspect of trunk. Furthermore, persistent left superior vena cava and right aberrant subclavian artery were diagnosed during the CT study. 3D VR images clearly demonstrated the correlation between these abnormal vessels and origins (Figures 1 and 2). The patient died due to bronchopneumonia.

The radiation dose was determined in terms of protocol dose-length product (DLP) in CT scanning. Effective dose (ED) was obtained on the value of DLP multiplying it by 0.039 conversion factor for infant. The DLP value for CT angiography was 10 mGy cm and estimated ED was calculated as 0.39 mSv.

DISCUSSION

Truncus arteriosus is a major conotruncal anomaly such as the Fallot tetralogy, double-outlet right ventricle, transposition of the great vessels and interrupted arcus aorta. It is related with chromosome 22q11 deletion and DiGeorge syndrome. Two classifications have been identified: one by Collett and Edwards in 1949 and the other one by Van Praagh[4] in 1965. There are four types of truncus arteriosus based on the branching pattern of pulmonary artery in each classification system. In Collets and Edwards classification, there is a single pulmonary trunk which origins from the left lateral aspect of the common trunk and pulmonary trunk was divided into right and left pulmonary arteries in type 1. In type 2, pulmonary trunk is absent and right and left pulmonary arterial branches origin from the posterolateral aspect of the common arterial trunk as in our case. Type 3, left and right pulmonary arteries origin from the left and right lateral aspects of the trunk. Type 4, major aorta-pulmonary collateral arteries enables pulmonary blood flow. Van Praagh classification is nearly the same the classification of Collett and Edwards. There are some similar differences.

In diagnosis, chest radiography may be the first simplest technique to show cardiomegaly and increased pulmonary vascular markings. However, it usually does not provide detailed diagnosis.

Echocardiography is a basic, rapid, non-radiating and non-invasive method for the diagnosis of TA. It may lead to determine hemodynamics. However, there are some limitations of echocardiography such as a small field of view (FOV) and an acoustic window. Also it is operator-dependent and the image quality is less in geriatric patients. It is also inadequate for visualization of anomalous vessel anatomy, origin and branching of arterial trunk, other associated anomalies with TA, and extra cardiac-structures[5].

Cardiac catheterization and angiography can be used for interventional procedures. It is now used less frequently for the diagnosis because it is an invasive method and it requiressedation or general anesthesia. Furthermore, it has catheter-related complications and causes the patient expose to high radiation doses and iodine-containing contrast agent.

Cardiovascular MRI is one of the best modalities for the diagnosis of TA. Being non-invasive and non-radiating, cardiovascular MRI provides structural and functional information such as ventricular volumes and function, flow in chambers and vessels, and tissue characteristics[5]. Disadvantages of MRI are that, it is less accessible and is expensive. It can be difficult for the patients to stay still for a long scanning time. Sedation or general anesthesia is required in young patients. Vascular stents, coils, and pacemakers can cause metallic artefacts.

CT provides excellent morphological evaluation of TA. 3D CT angiography provides greater informa-

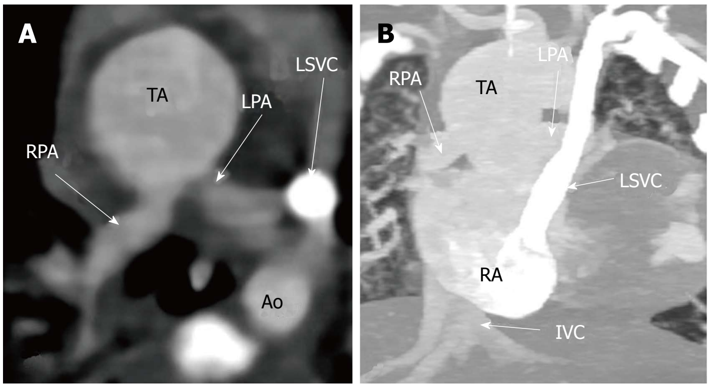

Figure 1 Axial (A) and maximum intensity projection coronal (B) images show a single arterial trunk origin from the right ventricule and left and right branched pulmonary vessels origin from the posterior aspect of trunk. In addition, persistent left superior vena cava is observed. TA: Truncus arteriosus; LPA: Left pulmonary artery; RPA: Right pulmonary artery; Ao: Descending aorta; LSVC: Left superior vena cava; IVC: Inferior vena cava; RA: Right atrium.

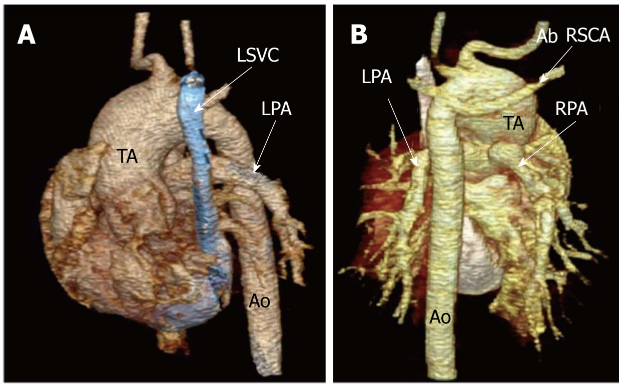

Figure 2 Volume rendered 3D images (A and B) clearly demonstrates correlation between these abnormal vessels and origins. TA: Truncus arteriosus; RPA: Right pulmonary artery; LPA: Left pulmonary artery; Ao: Descending aorta; LSVC: Left superior vena cava; IVC: Inferior vena cava; Ab RSCA: Right aberrant subclavian artery.

tion about anomalous anatomic detail, abnormal origin, branching of arterial trunk, cardiac and extra cardiac abnormalities such asaortic arch, coronary arteries abnormalities, left superior vena cava, and aberrant subclavian artery[5,6]. 3D images provide our understanding of complex anatomy and connection problems. Additionally, it is useful for surgical planning and post-operative assessment. It is easy to use especially in younger patients due to the fast acquisition time and necessity of minimal sedation[5,7]. It is more practical compared to MRI. Furthermore, CT can be safely used in patients with vascular stents, coils, and pacemakers. Airways and lung parenchyma can be evaluated simultaneously[7].

The significant disadvantages of CT when compared to MRI are ionizing radiation and iodinated contrast media, to which infants and children are especially sensitive. Moreover pediatric patients normally have higher heart rates and may have an incompatibility against beta-blockers. Breath-holding is an important problem in pediatric patients, as well. Flash spiral mode of dual-source CT can be used to overcome these disadvantages. Dual Source CT (DSCT) technology is the latest innovation in MDCT. In DSCT, ionizing radiation and the necessity of contrast media can be minimized with the usage of a weight-based low-dose protocol. Moreover, it allows high temporal resolution in patients with high heart rates or arrhythmia and does not require the use of beta-blockers. Providing high image quality in a shortest breah-holding period, as well, this technology is a fast scanning method due to the application of dual X-ray and detector system simultaneously[8]. They are very important features for pediatric cardiac CT examinations of congenital heart diseases. In our case, DSCT have clearly showed findings indicative of type 2 TA, the left and right branched pulmonary arteries that arose from posterior aspect of trunk. The ionizing radiation dose and contrast volume were calculated as 0.39 mSv and 4 mL, respectively.

In conclusion, DSCT is a useful imaging method for diagnosis, surgical planning, and postoperative evaluation of congenital heart abnormality such as TA, especially in infants and in children. It has significant roles to get the better limitations of other imaging modalities and should be preferred because of its fast imaging quality, low radiation dose, short breath-hold, and the other advantages.

COMMENTS

Case characteristics
A three day preterm female infant was referred to our clinic with cleft lip -palate and suspicion of cardiac anomaly.

Clinical diagnosis
Physical examination showed central cyanosis and grade 2/6 systolic murmur at the apex.

Differential diagnosis
Cardiovascular anomalies.

Laboratory diagnosis
Arterial blood gas results revealed that PaO_2 was 40.6 mmHg, $PaCO_2$ of 16.9 mmHg, O2SAT of 84%.

Imaging diagnosis
Multidedector computer tomography (MDCT) showed secundum type atrial septal defect and perimembraneous ventricular septal defect as echocardiography; in additionally, there was a single arterial trunk arising from the right ventricule, persistent left superior vena cava and right aberrant subclavian artery was diagnosed on CT study.

Pathological diagnosis
Truncus arteriosus.

Treatment
The patient was died due to bronchopneumonia.

Related reports
CT is a useful imaging method for diagnosis, surgical planning and postoperative evaluation of congenital heart diseases like truncus arteriosus especially in infants and children.

Term explanation
Dual source CT systems have design of a CT scanner with two X-ray tubes and two detectors that has the potential to overcome limitations of conventional

MDCT systems, such as temporal resolution for cardiac imaging.

Experiences and lessons

Dual-source CT has significant roles to get the better limitations of other imaging modalities and should be preferred because of its fast imaging quality, low radiation dose, short breath-hold and the other advantages.

Peer review

The manuscript is well written.

REFERENCES

1 **Pilu G,** Nicolaides KH. Diagnosis of Fetal Abnormalities: The 18-23-Week Scan. New York, NY: Taylor and Francis, 1999

2 **Barboza JM**, Dajani NK, Glenn LG, Angtuaco TL. Prenatal diagnosis of congenital cardiac anomalies: a practical approach using two basic views. *Radiographics* 2002; **22**: 1125-1137; discussion 1125-1137 [PMID: 12235342 DOI: 10.1148/radiographics.22.5.g02se171125]

3 **Murdison KA**, McLean DA, Carpenter B, Duncan WJ.Truncusarteriosuscommunis associated with mitral valve and left ventricular hypoplasia without ventricular septal defect: unique combination. *Pediatr Cardiol* 1996; **17**: 322-326 [PMID: 8660449 DOI: 10.1007/s002469900071]

4 **Yildirim A**, Karabulut N, Doğan S, Herek D. Congenital thoracic arterial anomalies in adults: a CT overview. *DiagnInterv Radiol* 2011; **17**: 352-362 [PMID: 21975665]

5 **Johnson TR**. Conotruncal cardiac defects: a clinical imaging perspective. *Pediatr Cardiol* 2010; **31**: 430-437 [PMID: 20165841 DOI: 10.1007/s00246-010-9668-y]

6 **Kawano T**, Ishii M, Takagi J, Maeno Y, Eto G, Sugahara Y, Toshima T, Yasunaga H, Kawara T, Todo K, Kato H. Three-dimensional helical computed tomographic angiography in neonates and infants with complex congenital heart disease. *Am Heart J* 2000; **139**: 6546-6560 [DOI: 10.1016/S0002-8703(00)90044-9]

7 **Goo HW**, Park IS, Ko JK, Kim YH, Seo DM, Yun TJ, Park JJ, Yoon CH. CT of congenital heart disease: normal anatomy and typical pathologic conditions. *Radiographics* 2003; **23** Spec No: S147-S165 [PMID: 14557509 DOI: 10.1148/rg.23si035501]

8 **Matt D**, Scheffel H, Leschka S, Flohr TG, Marincek B, Kaufmann PA, Alkadhi H. Dual-source CT coronary angiography: image quality, mean heart rate, and heart rate variability. *AJR Am J Roentgenol* 2007; **189**: 567-573 [PMID: 17715102 DOI: 10.2214/AJR.07.2078]

P- Reviewer: Battal B, Cademartiri F, Hiwatashi A
S- Editor: Ji FF **L- Editor**: A **E- Editor**: Lu YJ

World Journal of Radiology

Submit a Manuscript: http://www.wjgnet.com/esps/
Help Desk: http://www.wjgnet.com/esps/helpdesk.aspx
www.wjgnet.com

World J Radiol 2014 November 28; 6(11): I-V
ISSN 1949-8470 (online)

INSTRUCTIONS TO AUTHORS

GENERAL INFORMATION

World Journal of Radiology (*World J Radiol*, *WJR*, online ISSN 1949-8470, DOI: 10.4329) is a peer-reviewed open access (OA) academic journal that aims to guide clinical practice and improve diagnostic and therapeutic skills of clinicians.

Aim and scope

WJR covers topics concerning diagnostic radiology, radiation oncology, radiologic physics, neuroradiology, nuclear radiology, pediatric radiology, vascular/interventional radiology, medical imaging achieved by various modalities and related methods analysis. The current columns of *WJR* include editorial, frontier, diagnostic advances, therapeutics advances, field of vision, mini-reviews, review, topic highlight, medical ethics, original articles, case report, clinical case conference (clinicopathological conference), and autobiography.

We encourage authors to submit their manuscripts to *WJR*. We will give priority to manuscripts that are supported by major national and international foundations and those that are of great basic and clinical significance.

WJR is edited and published by Baishideng Publishing Group (BPG). BPG has a strong professional editorial team composed of science editors, language editors and electronic editors. BPG currently publishes 43 OA clinical medical journals, including 42 in English, has a total of 15471 editorial board members or peer reviewers, and is a world first-class publisher.

Columns

The columns in the issues of *WJR* will include: (1) Editorial: The editorial board members are invited to make comments on an important topic in their field in terms of its current research status and future directions to lead the development of this discipline; (2) Frontier: The editorial board members are invited to select a highly cited cutting-edge original paper of his/her own to summarize major findings, the problems that have been resolved and remain to be resolved, and future research directions to help readers understand his/her important academic point of view and future research directions in the field; (3) Diagnostic Advances: The editorial board members are invited to write high-quality diagnostic advances in their field to improve the diagnostic skills of readers. The topic covers general clinical diagnosis, differential diagnosis, pathological diagnosis, laboratory diagnosis, imaging diagnosis, endoscopic diagnosis, biotechnological diagnosis, functional diagnosis, and physical diagnosis; (4) Therapeutics Advances: The editorial board members are invited to write high-quality therapeutic advances in their field to help improve the therapeutic skills of readers. The topic covers medication therapy, psychotherapy, physical therapy, replacement therapy, interventional therapy, minimally invasive therapy, endoscopic therapy, transplantation therapy, and surgical therapy; (5) Field of Vision: The editorial board members are invited to write commentaries on classic articles, hot topic articles, or latest articles to keep readers at the forefront of research and increase their levels of clinical research. Classic articles refer to papers that are included in Web of Knowledge and have received a large number of citations (ranking in the top 1%) after being published for more than years, reflecting the quality and impact of papers. Hot topic articles refer to papers that are included in Web of Knowledge and have received a large number of citations after being published for no more than 2 years, reflecting cutting-edge trends in scientific research. Latest articles refer to the latest published high-quality papers that are included in PubMed, reflecting the latest research trends. These commentary articles should focus on the status quo of research, the most important research topics, the problems that have now been resolved and remain to be resolved, and future research directions. Basic information about the article to be commented (including authors, article title, journal name, year, volume, and inclusive page numbers); (6) Minireviews: The editorial board members are invited to write short reviews on recent advances and trends in research of molecular biology, genomics, and related cutting-edge technologies to provide readers with the latest knowledge and help improve their diagnostic and therapeutic skills; (7) Review: To make a systematic review to focus on the status quo of research, the most important research topics, the problems that have now been resolved and remain to be resolved, and future research directions; (8) Topic Highlight: The editorial board members are invited to write a series of articles (7-10 articles) to comment and discuss a hot topic to help improve the diagnostic and therapeutic skills of readers; (9) Medical Ethics: The editorial board members are invited to write articles about medical ethics to increase readers' knowledge of medical ethics. The topic covers international ethics guidelines, animal studies, clinical trials, organ transplantation, *etc*.; (10) Clinical Case Conference or Clinicopathological Conference: The editorial board members are invited to contribute high-quality clinical case conference; (11) Original Articles: To report innovative and original findings in radiology; (12) Research Report: To briefly report the novel and innovative findings in radiology; (13) Meta-Analysis: Covers the systematic review, mixedtreatment comparison, meta-regression, and overview of reviews, in order to summarize a given quantitative effect, *e.g.*, the clinical effectiveness and safety of clinical treatments by combining data from two or more randomized controlled trials, thereby providing more precise and externally valid estimates than those which would stem from each individual dataset if analyzed separately from the others; (15) Letters to the Editor: To discuss and make reply to the contributions published in *WJR*, or to introduce and comment on a controversial issue of general interest; (16) Book Reviews: To introduce and comment on quality monographs of radiology; and (17) Autobiography: The editorial board members are invited to write their autobiography to provide readers with stories of success or failure in their scientific research career. The topic covers their basic personal information and information about when they started doing research work, where and how they did research work, what they have achieved, and their lessons from success or failure.

Name of journal

World Journal of Radiology

ISSN

ISSN 1949-8470 (online)

Launch date

December 31, 2009

Frequency

Monthly

Editor-in-Chief

Kai U Juergens, MD, Associate Professor, MRT und PET/CT, Nuklearmedizin Bremen Mitte, ZEMODI - Zentrum für morpholo-

Editorial office

Jin-Lei Wang, Director
Xiu-Xia Song, Vice Director
World Journal of Radiology
Room 903, Building D, Ocean International Center,
No. 62 Dongsihuan Zhonglu, Chaoyang District,
Beijing 100025, China
Telephone: +86-10-85381891
Fax: +86-10-85381893
E-mail: editorialoffice@wjgnet.com
Help Desk: http://www.wjgnet.com/esps/helpdesk.aspx
http://www.wjgnet.com

Publisher

Baishideng Publishing Group Inc
8226 Regency Drive,
Pleasanton, CA 94588, USA
Telephone: +1-925-223-8242
Fax: +1-925-223-8243
E-mail: bpgoffice@wjgnet.com
Help Desk: http://www.wjgnet.com/esps/helpdesk.aspx
http://www.wjgnet.com

Instructions to authors

Full instructions are available online at http://www.wjgnet.com/1948-5204/g_info_20100312180518.htm.

Indexed and Abstracted in

PubMed Central, PubMed, Digital Object Identifier, and Directory of Open Access Journals.

SPECIAL STATEMENT

All articles published in journals owned by the BPG represent the views and opinions of their authors, and not the views, opinions or policies of the BPG, except where otherwise explicitly indicated.

Biostatistical editing

Statisital review is performed after peer review. We invite an expert in Biomedical Statistics to evaluate the statistical method used in the paper, including *t*-test (group or paired comparisons), chi-squared test, Ridit, probit, logit, regression (linear, curvilinear, or stepwise), correlation, analysis of variance, analysis of covariance, *etc*. The reviewing points include: (1) Statistical methods should be described when they are used to verify the results; (2) Whether the statistical techniques are suitable or correct; (3) Only homogeneous data can be averaged. Standard deviations are preferred to standard errors. Give the number of observations and subjects (*n*). Losses in observations, such as drop-outs from the study should be reported; (4) Values such as ED50, LD50, IC50 should have their 95% confidence limits calculated and compared by weighted probit analysis (Bliss and Finney); and (5) The word 'significantly' should be replaced by its synonyms (if it indicates extent) or the *P* value (if it indicates statistical significance).

Conflict-of-interest statement

In the interests of transparency and to help reviewers assess any potential bias, *WJR* requires authors of all papers to declare any competing commercial, personal, political, intellectual, or religious interests in relation to the submitted work. Referees are also asked to indicate any potential conflict they might have reviewing a particular paper. Before submitting, authors are suggested to read "Uniform Requirements for Manuscripts Submitted to Biomedical Journals: Ethical Considerations in the Conduct and Reporting of Research: Conflicts of Interest" from International Committee of Medical Journal Editors (ICMJE), which is available at: http://www.icmje.org/ethical_4conflicts.html.

Sample wording: [Name of individual] has received fees for serving as a speaker, a consultant and an advisory board member for [names of organizations], and has received research funding from [names of organization]. [Name of individual] is an employee of [name of organization]. [Name of individual] owns stocks and shares in [name of organization]. [Name of individual] owns patent [patent identification and brief description].

Statement of informed consent

Manuscripts should contain a statement to the effect that all human studies have been reviewed by the appropriate ethics committee or it should be stated clearly in the text that all persons gave their informed consent prior to their inclusion in the study. Details that might disclose the identity of the subjects under study should be omitted. Authors should also draw attention to the Code of Ethics of the World Medical Association (Declaration of Helsinki, 1964, as revised in 2004).

Statement of human and animal rights

When reporting the results from experiments, authors should follow the highest standards and the trial should conform to Good Clinical Practice (for example, US Food and Drug Administration Good Clinical Practice in FDA-Regulated Clinical Trials; UK Medicines Research Council Guidelines for Good Clinical Practice in Clinical Trials) and/or the World Medical Association Declaration of Helsinki. Generally, we suggest authors follow the lead investigator's national standard. If doubt exists whether the research was conducted in accordance with the above standards, the authors must explain the rationale for their approach and demonstrate that the institutional review body explicitly approved the doubtful aspects of the study.

Before submitting, authors should make their study approved by the relevant research ethics committee or institutional review board. If human participants were involved, manuscripts must be accompanied by a statement that the experiments were undertaken with the understanding and appropriate informed consent of each. Any personal item or information will not be published without explicit consents from the involved patients. If experimental animals were used, the materials and methods (experimental procedures) section must clearly indicate that appropriate measures were taken to minimize pain or discomfort, and details of animal care should be provided.

SUBMISSION OF MANUSCRIPTS

Manuscripts should be typed in 1.5 line spacing and 12 pt. Book Antiqua with ample margins. Number all pages consecutively, and start each of the following sections on a new page: Title Page, Abstract, Introduction, Materials and Methods, Results, Discussion, Acknowledgements, References, Tables, Figures, and Figure Legends. Neither the editors nor the publisher are responsible for the opinions expressed by contributors. Manuscripts formally accepted for publication become the permanent property of BPG, and may not be reproduced by any means, in whole or in part, without the written permission of both the authors and the publisher. We reserve the right to copy-edit and put onto our website accepted manuscripts. Authors should follow the relevant guidelines for the care and use of laboratory animals of their institution or national animal welfare committee. For the sake of transparency in regard to the performance and reporting of clinical trials, we endorse the policy of the ICMJE to refuse to publish papers on clinical trial results if the trial was not recorded in a publicly-accessible registry at its outset. The only register now available, to our knowledge, is http://www.clinicaltrials.gov sponsored by the United States National Library of Medicine and we encourage all potential contributors to register with it. However, in the case that other registers become available you will be duly notified. A letter of recommendation from each author's organization should be provided with the contributed article to ensure the privacy and secrecy of research is protected.

Authors should retain one copy of the text, tables, photographs and illustrations because rejected manuscripts will not be returned to the author(s) and the editors will not be responsible for loss or damage to photographs and illustrations sustained during mailing.

Online submissions

Manuscripts should be submitted through the Online Submission System at: http://www.wjgnet.com/esps/. Authors are highly recommended to consult the ONLINE INSTRUCTIONS TO AUTHORS (http://www.wjgnet.com/1948-5204/g_info_20100312180518.htm) before attempting to submit online. For assistance, authors encountering problems with the Online Submission System may send an email describing the problem to bpgoffice@wjgnet.com, or by telephone: +86-10-85381891. If you submit your manuscript online, do not make a postal contribution. Repeated online submission for the same manuscript is strictly prohibited.

MANUSCRIPT PREPARATION

All contributions should be written in English. All articles must be submitted using word-processing software. All submissions must be typed in 1.5 line spacing and 12 pt. Book Antiqua with ample margins. Style should conform to our house format. Required information for each of the manuscript sections is as follows:

Title page

Title: Title should be less than 12 words.

Running title: A short running title of less than 6 words should be provided.

Authorship: Authorship credit should be in accordance with the standard proposed by International Committee of Medical Journal Editors, based on (1) substantial contributions to conception and design, acquisition of data, or analysis and interpretation of data; (2) drafting the article or revising it critically for important intellectual content; and (3) final approval of the version to be published. Authors should meet conditions 1, 2, and 3.

Institution: Author names should be given first, then the complete name of institution, city, province and postcode. For example, Xu-Chen Zhang, Li-Xin Mei, Department of Pathology, Chengde Medical College, Chengde 067000, Hebei Province, China. One author may be represented from two institutions, for example, George Sgourakis, Department of General, Visceral, and Transplantation Surgery, Essen 45122, Germany; George Sgourakis, 2nd Surgical Department, Korgialenio-Benakio Red Cross Hospital, Athens 15451, Greece

Author contributions: The format of this section should be: Author contributions: Wang CL and Liang L contributed equally to this work; Wang CL, Liang L, Fu JF, Zou CC, Hong F and Wu XM designed the research; Wang CL, Zou CC, Hong F and Wu XM performed the research; Xue JZ and Lu JR contributed new reagents/analytic tools; Wang CL, Liang L and Fu JF analyzed the data; and Wang CL, Liang L and Fu JF wrote the paper.

Supportive foundations: The complete name and number of supportive foundations should be provided, e.g. Supported by National Natural Science Foundation of China, No. 30224801

Correspondence to: Only one corresponding address should be provided. Author names should be given first, then author title, affiliation, the complete name of institution, city, postcode, province, country, and email. All the letters in the email should be in lower case. A space interval should be inserted between country name and email address. For example, Montgomery Bissell, MD, Professor of Medicine, Chief, Liver Center, Gastroenterology Division, University of California, Box 0538, San Francisco, CA 94143, United States. montgomery.bissell@ucsf.edu

Telephone and fax: Telephone and fax should consist of +, country number, district number and telephone or fax number, e.g. Telephone: +86-10-85381891 Fax: +86-10-85381893

Peer reviewers: All articles received are subject to peer review. Normally, three experts are invited for each article. Decision on acceptance is made only when at least two experts recommend publication of an article. All peer-reviewers are acknowledged on Express Submission and Peer-review System website.

Abstract

There are unstructured abstracts (no less than 200 words) and structured abstracts. The specific requirements for structured abstracts are as follows:

An informative, structured abstract should accompany each manuscript. Abstracts of original contributions should be structured into the following sections: AIM (no more than 20 words; Only the purpose of the study should be included. Please write the Aim in the form of "To investigate/study/…"), METHODS (no less than 140 words for Original Articles; and no less than 80 words for Brief Articles), RESULTS (no less than 150 words for Original Articles and no less than 120 words for Brief Articles; You should present *P* values where appropriate and must provide relevant data to illustrate how they were obtained, e.g. 6.92 ± 3.86 *vs* 3.61 ± 1.67, $P < 0.001$), and CONCLUSION (no more than 26 words).

Key words

Please list 5-10 key words, selected mainly from *Index Medicus*, which reflect the content of the study.

Core tip

Please write a summary of less than 100 words to outline the most innovative and important arguments and core contents in your paper to attract readers.

Text

For articles of these sections, original articles and brief articles, the main text should be structured into the following sections: INTRODUCTION, MATERIALS AND METHODS, RESULTS and DISCUSSION, and should include appropriate Figures and Tables. Data should be presented in the main text or in Figures and Tables, but not in both. The main text format of these sections, editorial, topic highlight, case report, letters to the editors, can be found at: http://www.wjgnet.com/1948-5204/g_info_list.htm.

Illustrations

Figures should be numbered as 1, 2, 3, *etc*., and mentioned clearly in the main text. Provide a brief title for each figure on a separate page. Detailed legends should not be provided under the figures. This part should be added into the text where the figures are applicable. Keeping all elements compiled is necessary in line-art image. Scale bars should be used rather than magnification factors, with the length of the bar defined in the legend rather than on the bar itself. File names should identify the figure and panel. Avoid layering type directly over shaded or textured areas. Please use uniform legends for the same subjects. For example: Figure 1 Pathological changes in atrophic gastritis after treatment. A: ...; B: ...; C: ...; D: ...; E: ...; F: ...; G: …*etc*. It is our principle to publish high resolution-figures for the E-versions.

Tables

Three-line tables should be numbered 1, 2, 3, *etc*., and mentioned clearly in the main text. Provide a brief title for each table. Detailed legends should not be included under tables, but rather added into the text where applicable. The information should complement, but not duplicate the text. Use one horizontal line under the title, a second under column heads, and a third below the Table, above any footnotes. Vertical and italic lines should be omitted.

Notes in tables and illustrations

Data that are not statistically significant should not be noted. $^aP < 0.05$, $^bP < 0.01$ should be noted ($P > 0.05$ should not be noted). If there are other series of P values, $^cP < 0.05$ and $^dP < 0.01$ are used. A third series of P values can be expressed as $^eP < 0.05$ and $^fP < 0.01$. Other notes in tables or under illustrations should be expressed as ^1F, ^2F, ^3F; or sometimes as other symbols with a superscript (Arabic numerals) in the upper left corner. In a multi-curve illustration, each curve should be labeled with ●, ○, ■, □, ▲, △, *etc*., in a certain sequence.

Acknowledgments

Brief acknowledgments of persons who have made genuine contributions to the manuscript and who endorse the data and conclusions should be included. Authors are responsible for obtaining written permission to use any copyrighted text and/or illustrations.

REFERENCES

Coding system

The author should number the references in Arabic numerals according to the citation order in the text. Put reference numbers in square brackets in superscript at the end of citation content or after the cited author's name. For citation content which is part of the narration, the coding number and square brackets should be typeset normally. For example, "Crohn's disease (CD) is associated with increased intestinal permeability[1,2]". If references are cited directly in the text, they should be put together within the text, for example, "From references[19,22-24], we know that..."

When the authors write the references, please ensure that the order in text is the same as in the references section, and also ensure the spelling accuracy of the first author's name. Do not list the same citation twice.

PMID and DOI

Pleased provide PubMed citation numbers to the reference list, e.g. PMID and DOI, which can be found at http://www.ncbi.nlm.nih.gov/sites/entrez?db=pubmed and http://www.crossref.org/SimpleTextQuery/, respectively. The numbers will be used in E-version of this journal.

Style for journal references

Authors: the name of the first author should be typed in bold-faced letters. The family name of all authors should be typed with the initial letter capitalized, followed by their abbreviated first and middle initials. (For example, Lian-Sheng Ma is abbreviated as Ma LS, Bo-Rong Pan as Pan BR). The title of the cited article and italicized journal title (journal title should be in its abbreviated form as shown in PubMed), publication date, volume number (in black), start page, and end page [PMID: 11819634 DOI: 10.3748/wjg.13.5396].

Style for book references

Authors: the name of the first author should be typed in bold-faced letters. The surname of all authors should be typed with the initial letter capitalized, followed by their abbreviated middle and first initials. (For example, Lian-Sheng Ma is abbreviated as Ma LS, Bo-Rong Pan as Pan BR) Book title. Publication number. Publication place: Publication press, Year: start page and end page.

Format

Journals

English journal article (list all authors and include the PMID where applicable)

1 **Jung EM**, Clevert DA, Schreyer AG, Schmitt S, Rennert J, Kubale R, Feuerbach S, Jung F. Evaluation of quantitative contrast harmonic imaging to assess malignancy of liver tumors: A prospective controlled two-center study. *World J Gastroenterol* 2007; **13**: 6356-6364 [PMID: 18081224 DOI: 10.3748/wjg.13.6356]

Chinese journal article (list all authors and include the PMID where applicable)

2 **Lin GZ**, Wang XZ, Wang P, Lin J, Yang FD. Immunologic effect of Jianpi Yishen decoction in treatment of Pixu-diarrhoea. *Shijie Huaren Xiaohua Zazhi* 1999; **7**: 285-287

In press

3 **Tian D**, Araki H, Stahl E, Bergelson J, Kreitman M. Signature of balancing selection in Arabidopsis. *Proc Natl Acad Sci USA* 2006; In press

Organization as author

4 **Diabetes Prevention Program Research Group**. Hypertension, insulin, and proinsulin in participants with impaired glucose tolerance. *Hypertension* 2002; **40**: 679-686 [PMID: 12411462 DOI:10.1161/01.HYP.0000035706.28494.09]

Both personal authors and an organization as author

5 **Vallancien G**, Emberton M, Harving N, van Moorselaar RJ; Alf-One Study Group. Sexual dysfunction in 1, 274 European men suffering from lower urinary tract symptoms. *J Urol* 2003; **169**: 2257-2261 [PMID: 12771764 DOI:10.1097/01.ju.0000067940.76090.73]

No author given

6 21st century heart solution may have a sting in the tail. *BMJ* 2002; **325**: 184 [PMID: 12142303 DOI:10.1136/bmj.325.7357.184]

Volume with supplement

7 **Geraud G**, Spierings EL, Keywood C. Tolerability and safety of frovatriptan with short- and long-term use for treatment of migraine and in comparison with sumatriptan. *Headache* 2002; **42** Suppl 2: S93-99 [PMID: 12028325 DOI:10.1046/j.1526-4610.42.s2.7.x]

Issue with no volume

8 **Banit DM**, Kaufer H, Hartford JM. Intraoperative frozen section analysis in revision total joint arthroplasty. *Clin Orthop Relat Res* 2002; (**401**): 230-238 [PMID: 12151900 DOI:10.1097/00003086-200208000-00026]

No volume or issue

9 Outreach: Bringing HIV-positive individuals into care. *HRSA Careaction* 2002; 1-6 [PMID: 12154804]

Books

Personal author(s)

10 **Sherlock S**, Dooley J. Diseases of the liver and billiary system. 9th ed. Oxford: Blackwell Sci Pub, 1993: 258-296

Chapter in a book (list all authors)

11 **Lam SK**. Academic investigator's perspectives of medical treatment for peptic ulcer. In: Swabb EA, Azabo S. Ulcer disease: investigation and basis for therapy. New York: Marcel Dekker, 1991: 431-450

Author(s) and editor(s)

12 **Breedlove GK**, Schorfheide AM. Adolescent pregnancy. 2nd ed. Wieczorek RR, editor. White Plains (NY): March of Dimes Education Services, 2001: 20-34

Conference proceedings

13 **Harnden P**, Joffe JK, Jones WG, editors. Germ cell tumours V. Proceedings of the 5th Germ cell tumours Conference; 2001 Sep 13-15; Leeds, UK. New York: Springer, 2002: 30-56

Conference paper

14 **Christensen S**, Oppacher F. An analysis of Koza's computational effort statistic for genetic programming. In: Foster JA, Lutton E, Miller J, Ryan C, Tettamanzi AG, editors. Genetic programming. EuroGP 2002: Proceedings of the 5th European Conference on Genetic Programming; 2002 Apr 3-5; Kinsdale, Ireland. Berlin: Springer, 2002: 182-191

Electronic journal (list all authors)

15 Morse SS. Factors in the emergence of infectious diseases. Emerg Infect Dis serial online, 1995-01-03, cited 1996-06-05; 1(1): 24 screens. Available from: URL: http://www.cdc.gov/ncidod/eid/index.htm

Patent (list all authors)

16 **Pagedas AC**, inventor; Ancel Surgical R&D Inc., assignee. Flexible endoscopic grasping and cutting device and positioning tool assembly. United States patent US 20020103498. 2002 Aug 1

Statistical data
Write as mean ± SD or mean ± SE.

Statistical expression
Express *t* test as *t* (in italics), *F* test as *F* (in italics), chi square test as χ^2 (in Greek), related coefficient as *r* (in italics), degree of freedom as υ (in Greek), sample number as *n* (in italics), and probability as *P* (in italics).

Units
Use SI units. For example: body mass, m (B) = 78 kg; blood pressure, p (B) = 16.2/12.3 kPa; incubation time, t (incubation) = 96 h, blood glucose concentration, c (glucose) 6.4 ± 2.1 mmol/L; blood CEA mass concentration, p (CEA) = 8.6 24.5 μg/L; CO_2 volume fraction, 50 mL/L CO_2, not 5% CO_2; likewise for 40 g/L formaldehyde, not 10% formalin; and mass fraction, 8 ng/g, *etc*. Arabic numerals such as 23, 243, 641 should be read 23 243 641.

The format for how to accurately write common units and quantums can be found at: http://www.wjgnet.com/1948-5204/g_info_20100312183048.htm.

Abbreviations
Standard abbreviations should be defined in the abstract and on first mention in the text. In general, terms should not be abbreviated unless they are used repeatedly and the abbreviation is helpful to the reader. Permissible abbreviations are listed in Units, Symbols and Abbreviations: A Guide for Biological and Medical Editors and Authors (Ed. Baron DN, 1988) published by The Royal Society of Medicine, London. Certain commonly used abbreviations, such as DNA, RNA, HIV, LD50, PCR, HBV, ECG, WBC, RBC, CT, ESR, CSF, IgG, ELISA, PBS, ATP, EDTA, mAb, can be used directly without further explanation.

Italics
Quantities: *t* time or temperature, *c* concentration, *A* area, *l* length, *m* mass, *V* volume.
Genotypes: *gyrA*, *arg* 1, *c myc*, *c fos*, *etc*.
Restriction enzymes: *Eco*RI, *Hin*dI, *Bam*HI, *Kbo* I, *Kpn* I, *etc*.
Biology: *H. pylori*, *E coli*, *etc*.

Examples for paper writing
All types of articles' writing style and requirement will be found in the link: http://www.wjgnet.com/esps/NavigationInfo.aspx?id=15

SUBMISSION OF THE REVISED MANUSCRIPTS AFTER ACCEPTED
Authors must revise their manuscript carefully according to the revision policies of BPG. The revised version, along with the signed copyright transfer agreement, responses to the reviewers, and English language Grade B certificate (for non-native speakers of English), should be submitted to the online system via the link contained in the e-mail sent by the editor. If you have any questions about the revision, please send e-mail to esps@wjgnet.com.

Language evaluation
The language of a manuscript will be graded before it is sent for revision. (1) Grade A: priority publishing; (2) Grade B: minor language polishing; (3) Grade C: a great deal of language polishing needed; and (4) Grade D: rejected. Revised articles should reach Grade A or B.

Copyright assignment form
Please download a Copyright assignment form from http://www.wjgnet.com/1948-5204/g_info_20100312182928.htm.

Responses to reviewers
Please revise your article according to the comments/suggestions provided by the reviewers. The format for responses to the reviewers' comments can be found at: http://www.wjgnet.com/1948-5204/g_info_20100312182841.htm.

Proof of financial support
For papers supported by a foundation, authors should provide a copy of the approval document and serial number of the foundation.

STATEMENT ABOUT ANONYMOUS PUBLICATION OF THE PEER REVIEWERS' COMMENTS
In order to increase the quality of peer review, push authors to carefully revise their manuscripts based on the peer reviewers' comments, and promote academic interactions among peer reviewers, authors and readers, we decide to anonymously publish the reviewers' comments and author's responses at the same time the manuscript is published online.

PUBLICATION FEE
WJR is an international, peer-reviewed, OA online journal. Articles published by this journal are distributed under the terms of the Creative Commons Attribution Non-commercial License, which permits use, distribution, and reproduction in any medium and format, provided the original work is properly cited. The use is non-commercial and is otherwise in compliance with the license. Authors of accepted articles must pay a publication fee. Publication fee: 698 USD per article. All invited articles are published free of charge.

Baishideng®

Published by **Baishideng Publishing Group Inc**
8226 Regency Drive, Pleasanton, CA 94588, USA
Telephone: +1-925-223-8242
Fax: +1-925-223-8243
E-mail: bpgoffice@wjgnet.com
Help Desk: http://www.wjgnet.com/esps/helpdesk.aspx
http://www.wjgnet.com